Light manipulation by plasmonic nanostructures

A thesis submitted for the degree
of Doctor of Philosophy of
the Australian National University

Wei Liu

July, 2013

Australian
National
University

Declaration

This thesis is an account of research undertaken in the Nonlinear Physics Centre within the Research School of Physics and Engineering at the Australian National University between September 2009 and March 2013 while I was enrolled for the Doctor of Philosophy degree.

The research has been conducted under the supervision of A/Prof. Dragomir N. Neshev, Dr. Andrey E. Miroshnichenko, Dr. Ilya V. Shadrivov, A/Prof. Andrey A. Sukhorukov, and Prof. Yuri S. Kivshar. However, unless specifically stated otherwise, the material presented within this thesis is my own.

None of the work presented here has ever been submitted for any degree at this or any other institution of learning.

Wei Liu
July, 2013

Publications and selected presentations

Refereed journal articles

The published results that are included in this thesis are typed in bold.

1. **W. Liu, A. A. Sukhorukov, A. E. Miroshnichenko, C. G. Poulton, Z. Y. Xu, D. N. Neshev, and Yu. S. Kivshar, "Complete spectral gap in coupled dielectric waveguides embedded into metal," Appl. Phys. Lett. 97, 021106 (2010).**

2. **W. Liu, D. N. Neshev, A. E. Miroshnichenko, I. V. Shadrivov, and Yu. S. Kivshar, "Polychromatic nanofocusing of surface plasmon polaritons," Phys. Rev. B. 83, 073404 (2011).**

3. **W. Liu, D. N. Neshev, I. V. Shadrivov, A. E. Miroshnichenko, and Yu. S. Kivshar, "Plasmonic Airy beam manipulation in linear optical potentials," Opt. Lett. 36, 1164 (2011).**

4. A. R. Davoyan, W. Liu, A. E. Miroshnichenko, I. V. Shadrivov, S. I. Bozhevolnyi, and Yu. S. Kivshar, "Mode transformation in waveguiding plasmonic structures," Photon. Nano.: Fundam. Appl., **9**, 207(2011).

5. **W. Liu, D. N. Neshev, A. E. Miroshnichenko, I. V. Shadrivov, and Yu. S. Kivshar, "Bouncing plasmonic waves in half-parabolic potentials," Phys. Rev. A 84, 063805 (2011).**

6. **W. Liu, A. E. Miroshnichenko, D. N. Neshev, and Yu. S. Kivshar, "Broadband unidirectional scattering by core-shell nanoparticles," ACS Nano 6, 5489 (2012).**

7. **W. Liu, A. E. Miroshnichenko, D. N. Neshev, and Yu. S. Kivshar, "Polarization-independent Fano resonances arrays of core-shell nanoparticles," Phys. Rev. B 86 (R), 081407 (2012).**

8. **W. Liu, A. E. Miroshnichenko, R. F. Oulton, D. N. Neshev, O. Hess, and Yu. S. Kivshar, "Scattering of core-shell nanowires by the interference of electric and magnetic resonances," Opt. Lett. 38, 2621 (2013).**

9. B. Hopkins, W. Liu, A. E. Miroshnichenko, and Yu. S. Kivshar, "Optically-isotropic responses induced by discrete rotational symmetry of nanoparticle clusters," Nanoscale **5**, 6395 (2013).

Articles in the special issue of Optics & Photonics News

The December issues of Optics and Photonics News—the monthly magazine of The Optical Society of America—highlight the most exciting optics research that have emerged in the preceding 12 ***months all over the world.***

1. A. Minovich, A. E. Klein, W. Liu, A. Salandrino, N. Janunts, I.V. Shadrivov, A. E. Miroshnichenko, T. Pertsch, D. N. Neshev, D. N. Christodoulides, and Yu. S. Kivshar, "Airy plasmons: Bending light on a chip," Opt. Photon. News 12, 35 (2011).

2. A. E. Miroshnichenko, W. Liu, D. N. Neshev, Yu. S. Kivshar, A. I. Kuznetsov, Y. H. Fu, and B. Lukyanchuk, "Magnetic Light: Optical Magnetism of Dielectric Nanoparticles," Opt. Photon. News 12, 35 (2012).

Selected presentations

1. W. Liu, A. A. Sukhorukov, A. E. Miroshnichenko, C. G. Poulton, Z. Y. Xu, D. N. Neshev, and Yu. S. Kivshar, "Complete spectral gap in coupled hollow metallic waveguides," The 19th Australian Institute of Physics Congress incorporating the 35th Australian Conference on Optical Fibre Technology 2010 (Melbourne Australia, December 2010).

2. W. Liu, D. N. Neshev, A. E. Miroshnichenko, I. V. Shadrivov, and Yu. S. Kivshar, "Polychromatic nanofocusing of surface plasmons," CLEO/Europe and EQEC 2011 Conference (Munich Germany, May 2011).

3. W. Liu, D. N. Neshev, A. E. Miroshnichenko, I. V. Shadrivov, and Yu. S. Kivshar, "Polychromatic nanofocusing of surface plasmons," Quantum Electronics and Laser Science Conference (Baltimore USA., May 2011).

4. W. Liu, D. N. Neshev, A. E. Miroshnichenko, I. V. Shadrivov, and Yu. S. Kivshar, "Polychromatic nanofocusing of surface plasmons," The Fifth International Conference on Nanophotonics 2011 (Shanghai China, May 2011).

5. W. Liu, D. N. Neshev, A. E. Miroshnichenko, I. V. Shadrivov, and Yu. S. Kivshar, "Plasmonic analogue of quantum paddle balls," 2011 IQEC/CLEO Pacific Rim Conference (Sydney, August 2011).

6. W. Liu, "Arching light on a chip", John Carver Seminar Series 2011 (Canberra Australia, October 2011, the most popular talk).

7. W. Liu, A. M. Miroshnichenko, D. N. Neshev, and Yu. S. Kivshar, "Polarization-independent Fano resonances in one dimensional arrays of core-shell nanospheres," Quantum Electronics and Laser Science Conference (San Jose USA., May 2012).

8. W. Liu, A. E. Miroshnichenko, D. N. Neshev, and Yu. S. Kivshar, "Polarization independent Fano resonances in one dimensional arrays of core-shell nanoparticles," The Sixth International Conference on Nanophotonics 2012 (Beijing China, May 2012).

9. W. Liu, "Nanoscale light manipulations through plasmonic potentials and magneto-electric resonances", ITI seminar, University of Southern Denmark (Odense Denmark, December 2012, invited by Prof. Sergey I. Bozhevolnyi).

Acknowledgements

Since I started to write this thesis, I have been haunted, from time to time, by the strong feeling of being constrained by the rigid format requirement of the thesis, and thus of being deprived of my own right to express myself freely. As a student from mainland China, I am familiar with various theories of *Karl Marx* and naturally this feeling reminds me of his *Alienation Theory*. The major point of this theory is that the socially stratified society is like a big machine and as a mechanistic part of that machine, each person is alienated from his or her humanity, directed by the goals set by the big machine and deprived of the right to think him or herself. To some extent, as *Karl Marx* described, I feel I am alienated from my own thesis, and what is even worse, I am alienated from myself, working like a machine.

It is understandable that for scientific research there should be some rigid format requirement. Within the thesis however, I believe there should be a piece of land where we can express ourselves freely and write down whatever we like. The only such place I can find, throughout the whole thesis, is the section of acknowledgements. However when I have a look at the well accepted theses on the bookshelf of our department, and quite a few other ones approved by other universities all around the world, it is noticed that even this section is highly formatted, almost always starting with "Firstly I would like to thank ...". There is nothing to blame in writing this section like this and actually in the first version I did so. But immediately after everything had been written down I realized that throughout the thesis which I should be able to claim my thesis, ironically I would not be able to find anything with an obvious stamp of my name. The even worse consequence of this kind of fixed format, I believe, is that it makes my sincere thanks extremely dry, and overshadows rather than illuminates the gratitude held at the bottom of my heart.

I would like to identify myself as an outgoing person and besides the supervisory panel, I have a lot of interactions with almost anyone else in our group and many researchers in other institutes. To abandon the well accepted format makes it much more difficult rather than simpler to write this section, as it is always easier to put the name of everyone after the expression "many thanks to". Now the real challenge is how is it possible to enable all those people, to whom I am grateful, feel through the somehow cold sentences a warm and vibrating heart full of thanks?

The ancient Chinese philosopher *Laozi* told us from the first sentence of his book *Dao Te Ching* that "*The Way that can be described is not an everlasting*

Way; the Name that can be named is not a perpetual name". The Austrian-British philosopher *Ludwig Wittgenstein* expressed some similar belief by writing down "*My work consists of two parts: the one I have presented here plus all that I have not written. And it is precisely the second part that is the important one*". The core of what mentioned above, as far as I understand, is that the power of language is quite limited. I believe that there exists another version of Heisenberg's uncertainty principle: the more you want to reveal the bottom of your heart, the less words you should use. Maybe the best way to give my thanks to all the people who have been of great help, is not to write down long sentences full of their names, but to keep silent.

To make this section appear to be not too bizarre, I would like to write it down here a specific short story between me and *Dragomir Neshev*, who is the chair of the supervisory panel:

At the beginning of July 2012 I went to Imperial College London for a half year visit and approximately two months later I had to make a very urgent trip back to Canberra Australia due to some private personal crisis. After I explained briefly to *Dragomir* what the situation for me was, he said "*Wei, there are some things I can help you with while for others I can do nothing, but you can always count on me for full support!*"

At the same time *Andrey Miroshnichenko*, another member of the supervisory panel, also gave me a lot of consolation and encouragement. I am deeply pleased that throughout my PhD period I have been treated by the supervisory panel not as an employee or cheap labor, as is the case in many groups, but as a close friend. I will cherish all the time spent together with not only the people mentioned here, but also all of you, who have been of great help in terms of everything and to whom I am deeply grateful.

Abstract

This thesis studies various effects based on the excitation of surfaces plasmons in various plasmonic nanostructures. We start the thesis with a general introduction of the field of plasmonics in Chapter 1. In this chapter we discuss both propagating surface plasmon polaritons (SPPs) and localized surface plasmons (LSPs), how to geometrize LSPs to make it related to SPPs through the Bohr condition, the features of subwavelength confinement and near-field enhancement, and wave guidance through coupled LSPs. Then after the discussion of the achievements and challenges in this field (Section 1.3), we will outline the basic structure of the thesis at the end of this chapter (Section 1.4).

In Chapter 2 we demonstrate a new mechanism to achieve complete spectral gap without periodicity along propagation direction based on the coupling of backward and forward modes supported by plasmonic nanostructures. We study the backward modes in single cylindrical plasmonic structures (Section 2.2) and focus on the two simplest cases: nanowires and nanocavities. Afterwards, we demonstrate how to achieve spectral gaps in coupled plasmonic nanocavities (Section 2.3). A polarization-dependent spectral gap is achieved firstly in two coupled nanocavities which support forward and backward modes respectively (Section 2.3.1). At the end we demonstrate a complete spectral gap, which is induced by the symmetry of a four-coupled-nanocavity system (Section 2.3.2).

In Chapter 3 we study beam shaping in plasmonic potentials. Based on the similarity between Schrödinger equation for matter waves and paraxial wave equation for photons, we introduce the concept of *plasmonic potentials* and demonstrate how to obtain different kinds of potentials for SPPs in various modulated metal-dielectric-metal (MDM) structures. We investigate firstly the parabolic potentials in quadratically modulated MDM and the beam manipulations in such potentials, including polychromatic nanofocusing in full parabolic potentials (Section 3.2.1), plasmonic analogue of quantum paddle balls in half parabolic potentials (Section 3.2.2), and adiabatic nanofocusing in tapered parabolic potentials (Section 3.2.3). In the following section (Section 3.3) we show the existence of linear plasmonic potentials in wedged MDM and efficient steering of the Airy beams in such potentials (Section 3.3.2) after a brief introduction on Airy beams in free space (Section 3.3.1).

In Chapter 4 we study scattering engineering by magneto-electric core-shell nanostructures with induced electric and magnetic resonances. The introduction part (Section 4.1) gives a brief overview on the scattering of solely electric dipole

(ED) or magnetic dipole (MD), and how the coexistence and interference of the ED and the MD can bring extra flexibility for scattering shaping. Afterwards, we discuss the scattering shaping by core-shell nanostructures through the interferences of electric and magnetic dipoles (Section 4.2), including two examples of broadband unidirectional scattering by core-shell nanospheres (Section 4.2.1) and efficient shaping of the scattering pattern for core-shell nanowires (Section 4.2.2). At the end of this chapter we demonstrate polarization-independent Fano resonances in arrays of core-shell nanospheres (Section 4.3.2).

At the end of this thesis in Chapter 5 we summarize the results and draw the conclusions. We also discuss the challenges and possible future developments of the field of plasmonics.

Contents

CHAPTER 1

Introduction

All the research work presented in this thesis falls into the field of plasmonics, of which the major attractive capability is to confine light down to the nanoscale. This rapidly expanding and promising field of plasmonics is not an isolated field but comes from a broader background of nano-optics, which is built on the developments of classical optics. The core of nano-optics, similar to that of the field of plasmonics, is go gain access to the length scale beyond the diffraction limit. To put the contents of this thesis in a clearer and wider context, before the specific introduction to plasmonics, we start with a short introduction to diffraction limit and the field of nano-optics.

1.1 Diffraction limit and nano-optics

The earliest record of principles of classical geometric optics dates back to the Chinese philosopher Mozi (approximately 470 to 390 BC), who put forward unprecedented innovative new ideas in the field of optics, including ideas like using pinholes and camera obscura that had not been even considered until the Arab physicists of the early 11th century AD [1]. After Mozi, although there had been a lot of studies about geometric optics, especially those conducted systematically by the Greek philosophers (Empredocles and Euclid), optical devices (telescopes and microscopes) had not been built for scientific probe until Galileo Galilei in the early 17th century [2, 3]. There had been steady development afterwards especially for the improvement of the resolution of microscopes. As more of the nature of light was revealed, it was realized that any further improvement could not be achieved as there was always a insurmountable limit [2, 3]. It was after the work of Abbe and Rayleigh that such limit was accepted as the diffraction limit [2, 3].

Diffraction limit

The formulas of Abbe diffraction limit can be easily reproduced using Fourier Optics [4], while a more intuitive and easier way to obtain them is employing the Heisenberg's uncertainty principle [5–7]. In optics, the principle can be expressed as:

$$\Delta k \cdot \Delta x \geq 1/2, \tag{1.1}$$

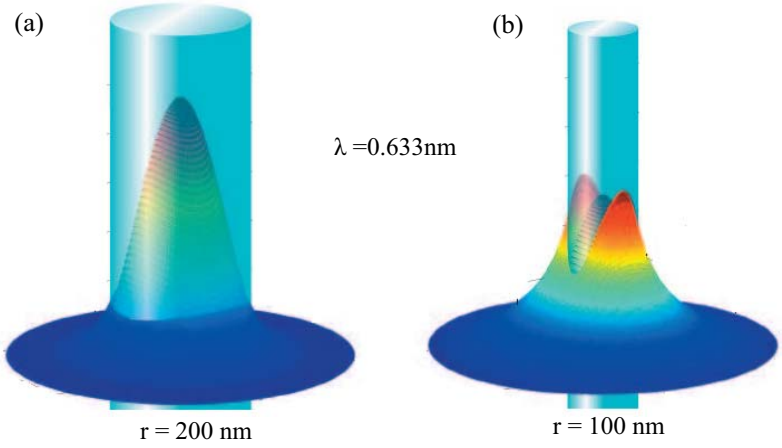

Figure 1.1: The Poynting vector distribution for the fundamental mode of silica nanowires of radii of (a) $r = 200$ nm and (b) $r = 100$ nm. The free space wavelength is $\lambda = 633$ nm. After Ref. [8].

which indicates that to reduce the uncertainty of spatial position, usually the increase of the uncertainty for spatial frequency is required. In homogenous and isotropic media with refractive index n, the uncertainty in the domain of spatial frequency is restricted by $\Delta k \leq 2\pi n/\lambda_0$ where λ_0 is the wavelength in vacuum. Then according to Eq. (1.1), the uncertainty in the domain of spatial frequency satisfies:

$$\Delta x \geq \frac{\lambda_0}{4\pi n} = \frac{\lambda_{\text{eff}}}{4\pi}, \tag{1.2}$$

which is very similar to what was derived by Abbe and Rayleigh [2, 3].

The usual way to visualize the diffraction limit is to show the focal spot of a lens, as was done in Refs. [5, 6]. Here we visualize it in an alternative way through the basic properties of conventional waveguides. In Fig. 1.1 we show the energy confinement of the fundamental modes of silica nanowires of two different radii. When the wire diameter is comparable to the effective wavelength of the light in silica ($\approx$ 420 nm), most of the energy can be still confined within the nanowire [Fig. 1.1(a)]. However, when we reduce the diameter of the silica wire to be significantly smaller than the effective wavelength, most of the energy will spread out of the nanowire, as this simple waveguide will not be able to confine the light beyond the diffraction limit [Fig. 1.1(b)].

Nano-optics

Since the establishment of the theory of diffraction limit many techniques and approaches have been demonstrated to be able to go beyond the diffraction limit, which fueled the rapid development of the field of nano-optics. The central goal of nano-optics is to gain access to the regime which is in the nanoscale and beyond the diffraction limit, with the well known techniques as multi-photon microscopy, near-field microscopy, and so on [3]. Nowadays, this field is developing rapidly and attracting more interest than ever before. The prosperity in this field is firstly

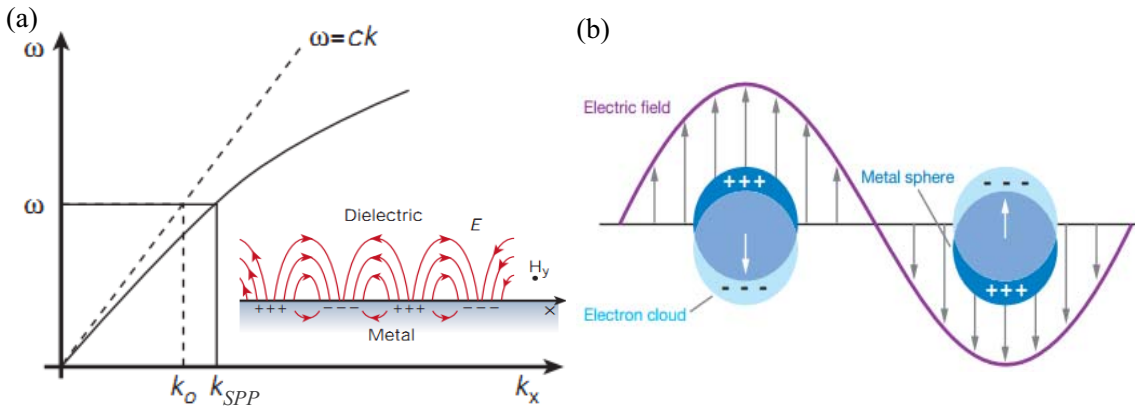

Figure 1.2: Schematic illustration of (a) SPPs on the metal-dielectric interface with well defined dispersion curves. The propagation constant of the SPPs is larger (than that of the photons of the same frequency in free space (indicated by the dashed line). (b) Dipolar LSPs supported by spherical metal particles. After Refs. [9, 16].

driven by what we have achieved, such as the capability of better nanofabrication and larger simulation capacity enabled by the development of supercomputers. At the same time it is driven by what we hope to achieve in the future: optical computer based on the miniaturization of optical circuits and its integration with electronic devices, microscopy with unprecedented super-resolution, data storage device with ultra-high data density, and so on. It is also expected that some new physics can be found in the nanoscale, as mentioned by Richard Feynman "There is plenty of room at the bottom". There are so many branches of nano-optics that it is impossible to list them all, but most of them will fall into the following categories [3]: theoretical concepts in the nanoscale, interaction of light with nanosystems, interactions between nanosystems, diffraction limit and strongly focused light, resonance phenomena in nanosystems and so on. As an outstanding and promising sub-branch of nano-optics, the field of plasmonics is what the thesis is mainly about.

The field of plasmonics originates from the study of electromagnetic responses of metals and nowadays any science and technology that are related to the coupling of photons into the collective oscillations of electrons at the metal-dielectric interface might be categorized into this field [3, 9–16]. The recent usual boom and expansion has been boosted by mainly two important discoveries: extraordinary transmission through thin metal films [17] and metamaterials [18–22], where the excitation of plasmonic states plays a significant role.

1.2 Plasmonics: go beyond the diffraction limit

Two branches of plasmonics: propagating surface plasmon polaritons and localized surface plasmons

The field of plasmonics can be roughly divided into two branches: propagating surface plasmon polaritons (SPPs) and localized surface plasmons (LSPs) [10,

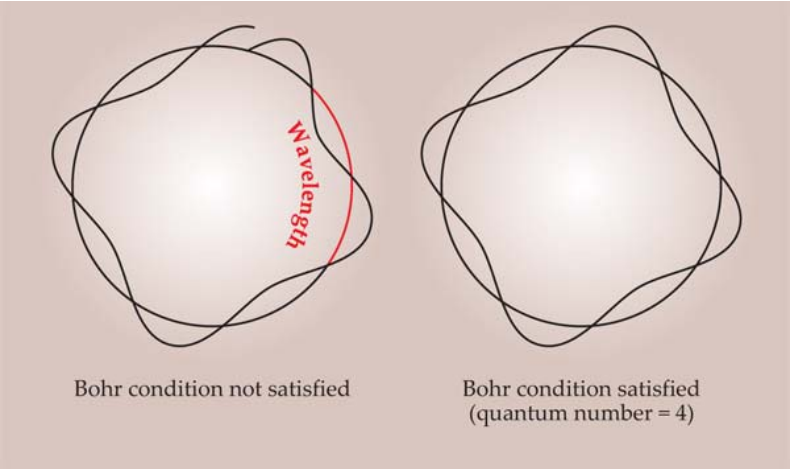

Figure 1.3: Schematic illustration of the Bohr condition: on the right the condition is satisfied where the circumference of an electron contains an integral number of the de Broglie wavelengths while on the left the condition is not satisfied. After Ref. [23].

13, 14]. SPPs is a propagating coupled state of electrons and photons and have a well defined wave vector along the propagation direction while LSPs are localized resonances accompanied by the collective oscillations of electrons and the radiation into the surrounding media. At the same time, SPPs usually have broadband response and thus are characterized by continuous dispersion curves, while LSPs are localized resonances and are characterized by a set of discrete resonant frequencies. In Fig. 1.2 we give schematic representations of the two states in the two simplest structures: (a) SPPs confined at the interface of a semi-infinite metal and dielectric layer and (b) dipolar LSPs resonance supported by spherical metal particles.

Geometrize localized surface plasmons through Bohr condition

We note here that the two branches of LSPs and SPPs are highly related to each other. LSPs is a kind of localized resonance and is similar to most localized resonances for which the Bohr condition is satisfied [23, 24]. According to the Bohr condition, to support a well defined resonance, the length of enclosed orbit of matter waves should contain an integral number of the de Broglie wavelengths. Figure 1.3 shows schematically the Bohr condition and when the condition is satisfied, the phase accumulated along the enclosed orbit is an integral number of 2π. It was through Bohr condition that the quantum states of Hydrogen atom were geometrized.

In optics the Bohr condition can be expressed as:

$$\oint n(\mathbf{r}) k_0 d\mathbf{r} = 2m\pi, \tag{1.3}$$

where $n(\mathbf{r})$ is position dependent refractive index and k_0 is the wavenumber in free space and m is an integer, which usually is used to indicate the order of the mode.

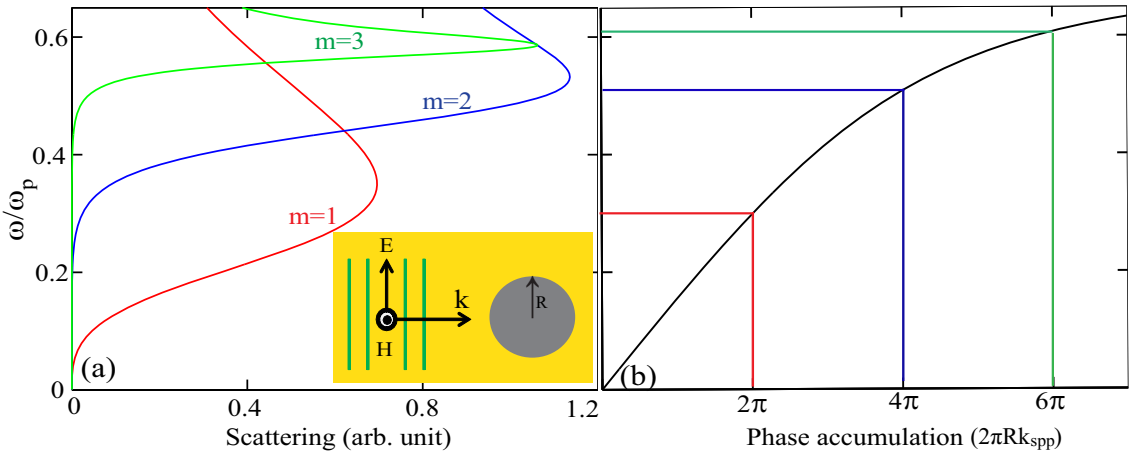

Figure 1.4: (a) Scattering spectra of modes of different orders of an infinite metallic nanowire of radius R scattering a normally incident TM plane wave (inset). (b) The dispersion curve of the corresponding waveguide of the infinite metallic nanowire: a semi-infinite metal dielectric structure shown in the inset of Fig. 1.2(a). The dispersion curve is the same as that in Fig. 1.2(a) with the wavenumber replaced by the phase accumulation ($2\pi R k_{\text{spp}}$) along the circum of the nanowire.

This condition basically means that to support a well defined resonance the phase accumulation along a loop of optical path should be an integral number of 2π.

To support LSPs resonance within plasmonic structures, as the phase is accumulated through the propagation of SPPs modes, the corresponding Bohr condition is:

$$\oint k_{\text{spp}} d\mathbf{r} = 2m\pi, \tag{1.4}$$

where k_{spp} is the wavenumber for the SPPs in a corresponding extended plasmonic waveguide. To clearly explain the links between SPPs and LSPs and the above equation, we show the simplest case in Fig. 1.4. Figure 1.4(a) shows the scattering spectra of a normally incident TM plane wave scattered by an infinite metallic nanowire, where the first three modes are shown. To clarify the physics, the metal is simply characterized by the lossless Drude model with plasmon frequency ω_p and the radius of the nanowire R is $R = c\pi/\omega_p$, where c is the speed of light. The corresponding extended plasmonic waveguide of such a infinite metallic nanowire is the semi-infinite metal dielectric structure shown in the inset of Fig. 1.2(a). The dispersion relation of SPPs supported by this structure is:

$$k_{\text{spp}} = \frac{2\pi}{\lambda}\sqrt{\frac{\varepsilon_m \varepsilon_d}{\varepsilon_m + \varepsilon_d}}, \tag{1.5}$$

where ε_m and ε_d are the permittivities of the metal and dielectric respectively and k_{spp} is the effective wavenumber of the SPPs supported. The dispersion is shown in Fig. 1.2(a) and in Fig. 1.4(b) we show this dispersion curve again but changed the horizontal axis from k_{spp} to phase accumulation along the circum of the cross section of the nanowire, which equals to $2\pi R k_{\text{spp}}$. Figure 1.2 shows that the resonant

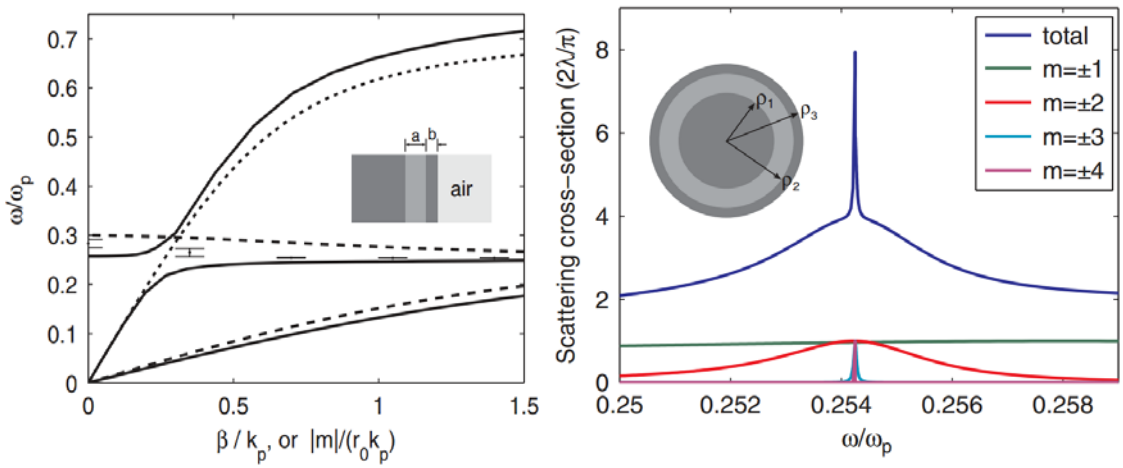

Figure 1.5: (a) The dispersion curves of a three-layered metal-dielectric structure (dark layers and light layer indicate metal and dielectric respectively as shown in the inset). (b) The scattering cross sections of the corresponding three-layered core-shell nanoparticle (inset) with the contributions from modes of different orders. After Ref. [25].

frequencies of modes of different orders correspond to the frequencies where the phase accumulation is an integral number of 2π and this tells us convincingly that the Bohr condition can be directly applied to the analysis of LSPs.

Another noticeable demonstration of this principle is the effect of superscattering by nanoparticles [25]. Figure 1.5(a) shows the dispersion curves of a three-layered metal-dielectric waveguide (dark layers indicate metal and light area indicates dielectric as shown in the inset), where a flat band exists. If we wrap the three-layered planar waveguide, then we can get a 2D three-layered core-shell nanoparticles shown in the inset of Fig. 1.5(b), where the scattering cross sections of such particle is also shown. According to Eq. (1.4) and the flat band shown in Fig. 1.5(a), the resonant frequencies of the modes of different orders (characterized by m) should be almost the same. Figure 1.5(b)shows the scattering spectra of the three-layered core-shell nanoparticle and the contributions from modes of different orders are also shown. It is clear that modes of different orders are overlapped at the same frequency, which agrees well with the analysis above.

After LSPs are geometrized, now a lot of existing scattering features can be understood and some new scattering features are expected. Usually it is widely accepted that within resonant structures higher order modes are supported at higher frequencies as shown in Fig. 1.4(a). Also the resonance frequency will blueshift with shrinking structure sizes. Now we understand that this is due to the normal dispersion of the corresponding waveguide as shown in Fig. 1.4(b). Given that the dispersion curves can be engineered, relative resonant frequencies of the higher order modes can be manipulated, and the resonant frequency does not have to blueshift for smaller particle sizes. Fan *et al.* demonstrated [25] that if a flat band can be obtained, then modes of different orders can be overlapped at the same frequency (Fig. 1.5). We can make a step further and expect that if we get

a dispersion curve with negative group velocity (the corresponding mode is called backward mode and more details will be given in Chapter 1 about the backward modes in plasmonic structures), then higher order modes can be supported at lower frequencies. At the same time we note that, if the corresponding waveguide shows multi-band dispersions in contrast to the single band dispersion shown in Fig. 1.4(b), we can achieve: (1) modes of different orders at the same frequencies without a flat band and (2) several modes of the same order at different frequencies and the number of the modes is decided by how many bands are involved in the corresponding waveguides. For example, for the structure shown in Fig. 1.5(a) investigated by Fan *et al.*, there is another band below the flat band. Due to the existence of this band, another set of modes with mode orders $m = 1 : 3$ are supported at the frequencies of $\omega/\omega_p = 0.0496,\ 0.0929,\ 0.1285$, respectively.

In Chapter 4 we will show the overlapping of the ED and the MD in core-shell nanoparticles, including both nanospheres and nanowires. This is due to the coexistence of two bands, which will accumulate phase independently to support the ED and the MD respectively. The two modes overlap at the same frequency, where the two bands simultaneously accumulate a phase of 2π, leading to the coexistence of two dipoles at the same frequency. The mechanism to support modes of different orders at the same frequency shown in Ref. [25] relies on a flat band, where the effect of loss is devastating and the high order modes almost cannot be observed when loss is considered [25]. However the mechanism we mention here to support several modes of the same frequency comes from the multi-band dispersion of the corresponding plasmonic waveguides, which can avoid the huge loss of metal at the frequency of a flat band and thus be more promising for related applications.

Generally speaking, the Bohr condition discussed above can be applied to geometrize the LSPs. But still this model has some limitations, as is the case for the original Bohr model in the beginning period of quantum mechanics [26]. For example, for metal particles of the size much smaller than the free space wavelength (when the quasi-static approximation of Maxwell equations can be applied), according to Eqs. (1.3)-(1.5), all plasmon resonances will locate approximately at the surface plasmon frequency when $\varepsilon_m + \varepsilon_d = 0$ [13, 14, 27]. This is still the case for metallic nanowires for p-polarized normal incidence [as shown in the inset Fig. 1.4(a)] under quasi-static approximation, when all the plasmon modes overlap at the surface plasmon frequency. But for metallic spheres this is not the case any more. Under quasi-static approximation, it is well known that the LSP modes of metal spheres resonate when $\varepsilon_m + (1 + \frac{1}{m})\varepsilon_d = 0$, where m is the mode order and should be a positive integer [13, 14, 27]. The resonance frequencies of modes of sufficiently higher order($m \gg 1$) will converge to the surface plasmon frequency ($1 + \frac{1}{m} \to 1$), but for modes of low order, the resonance frequency will be significantly different. For example, the resonance frequency of the fundamental mode ($m = 1$, dipole mode) is the Fröhlich frequency, when $\varepsilon_m + 2\varepsilon_d = 0$ [27]. Other limitations include that it is hard to apply the Bohr condition to metallic particles of arbitrary shapes, for which it is hard to decide the length of the phase accumulation path, and hard to explain the polarization dependence and the edge effects. Still a lot of work needs to be done to clarify those limitations and to introduce more accurate models to

geometrize the localized plasmonic resonances.

Subwavelength confinement and near-field enhancement within plasmonic structures

After geometrize LSPs and thus bridge the two branches of LSPs and SPPs through the Bohr condition, now we come to the problems how photons can be confined down to subwavelength regime within resonant plasmonic structures. According to Eq. (1.1) and Eq. (1.2), to improve the confinement in spatial domain, one has to increase the uncertainty in spatial frequency domain and/or shrinking the effective wavelength of the state. As is shown by the dispersion curve in Fig. 1.2(a), the effective wavelength of SPPs can be much smaller (with larger wavenumber) than that of the photons of the same frequency in free space, leading to much better confinement down to the subwavelength regime. While at the same time, this also indicates that SPPs modes cannot be excited directly by photons in free space, but rely on special techniques [9–14]. SPPs can be excited through Kretschmann geometry, Otto geometry, SNOM tip, grating diffraction, scattering of surface roughness and so on [9–14]. For better visualization of this effect, in Fig. 1.6 we show schematically the energy confinement of the *fundamental* SPPs modes supported by plasmonic waveguides with shrinking cross sections. In sharp contrast to the dielectric waveguides shown in Fig. 1.1, plasmonic waveguides are able to confine the fundamental guided SPPs modes to neighboring area of the waveguide, irrespective of the size of the waveguide. We note here that this principle holds only for the fundamental plasmonic modes. Other modes will be cut-off at some point with shrinking waveguide sizes and will not be able be further confined. The basic mechanism is that as the size of the plasmonic waveguide is reduced, the effective wavelength of the fundamental SPPs mode is also shrunk, resulting in a better confinement than its all-dielectric counterpart [28]. For example, the widely used MDM structure supports two modes of even and odd parity (with respect to the transverse magnetic field) respectively [9–14]. The even mode is the fundamental mode and Fig. 1.6 shows correctly the corresponding energy flows with shrinking cross sections. For the odd (long range SPP) mode however, with shrinking cross sections of the MDM structure, the energy flow shows an opposite trend in contrast to what is shown in Fig. 1.6: the energy spread rather than become more confined. Furthermore, beyond some critical size of the cross section, the odd mode will be cut-off and cannot be excited anymore.

It is known that to support a localized mode, usually it is required that the minimum size of the particle has to be comparable to the effective wavelength. This is because according to the Bohr condition there should be an optical path that is long enough for sufficient phase accumulation [29]. While this is not the case for metal particles, as metal particle even in the deep subwavelength regime can still support LSP modes [10, 13, 14]. This is due to the fact that at the metal-dielectric interface k_{spp} could be much larger than its counterpart in free space. Consequently according to Eq. (1.4) the phase accumulation within plasmonic particles can be much faster and then a much shorter optical length is required to accumulate sufficient phase to

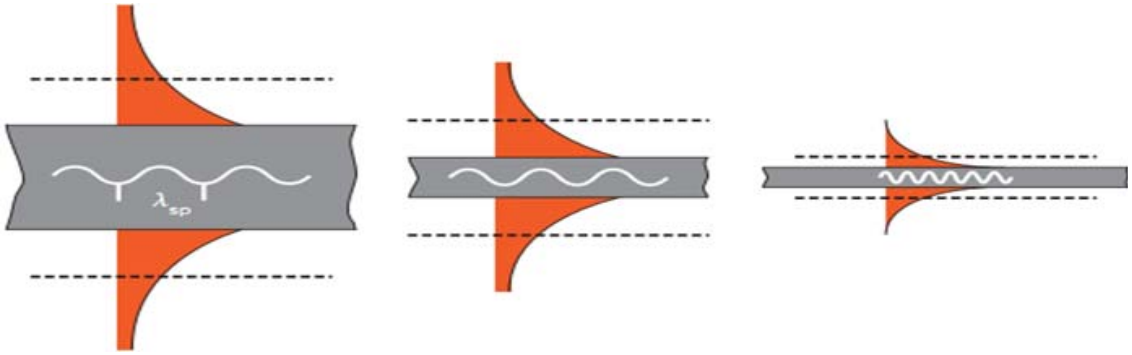

Figure 1.6: Schematic illustration of the energy confinement of the **fundamental** SPPs modes supported by plasmonic waveguides of shrinking sizes. After Ref. [28].

support a resonance. It is also well shown that for shrinking metal particles sizes, the resonant frequency would blue-shift [10]. This could be easily explained through Eq. (1.4): shrinking particle sizes also means shorter optical paths and thus larger wavenumber (usually smaller wavelength) is required to accumulate sufficient phase to support a resonance. Based on the same reason, for the same optical length, it is easier to support higher order LSPs resonances than conventional photonic resonances. In Fig. 1.7(a) we show a silver-coated micro-disk which support a lot of whispering-gallery modes as shown in Fig. 1.7(b). The whispering-gallery modes supported can be roughly categorized into two branches: LSPs modes with subwavelength confinement [SPP branches in Fig. 1.7(b) with mode profile shown in the inset. We note here that those plasmonic modes demonstrated in Ref. [30] are actually localized standing waves and thus it is better to term them LSPs modes, rather than SPP modes as was termed in this paper.] and conventional photonic modes without subwavelength confinement [DE branches in Fig. 1.7(b) with mode profile shown in the inset]. It is clear that higher order LSPs modes are supported than the conventional photonic modes at the same frequency. Also we note that the LSPs resonance is confined at the metal-dielectric interface while the conventional photonic modes are mainly confined within silica.

Despite the subwavelength confinement described above, there is also the generic feature of near-field enhancement within plasmonic structures, both for SPPs modes and LSPs resonances [3, 9–16]. As a coupled state of coherent electron oscillations and photons, plasmonic states (for both SPPs and LSPs) are mainly confined at the metal-dielectric interface, where the field is significantly enhanced [3, 9–14]. Such field enhancement can be further improved by nanofocusing of SPPs modes within in tapered waveguides [Fig. 1.8(a)] or by nanofocusing of LSPs resonances within a chain a coupled metal particles of decreasing sizes [Fig. 1.8(b)].

Waveguiding through coupled localized surface plasmon resonances

We can categorize the field of plasmonics into to two branches by whether the states excited are localized or propagating, with SPPs characterized by dispersion curves and LSPs characterized discrete resonant frequencies. However the demarca-

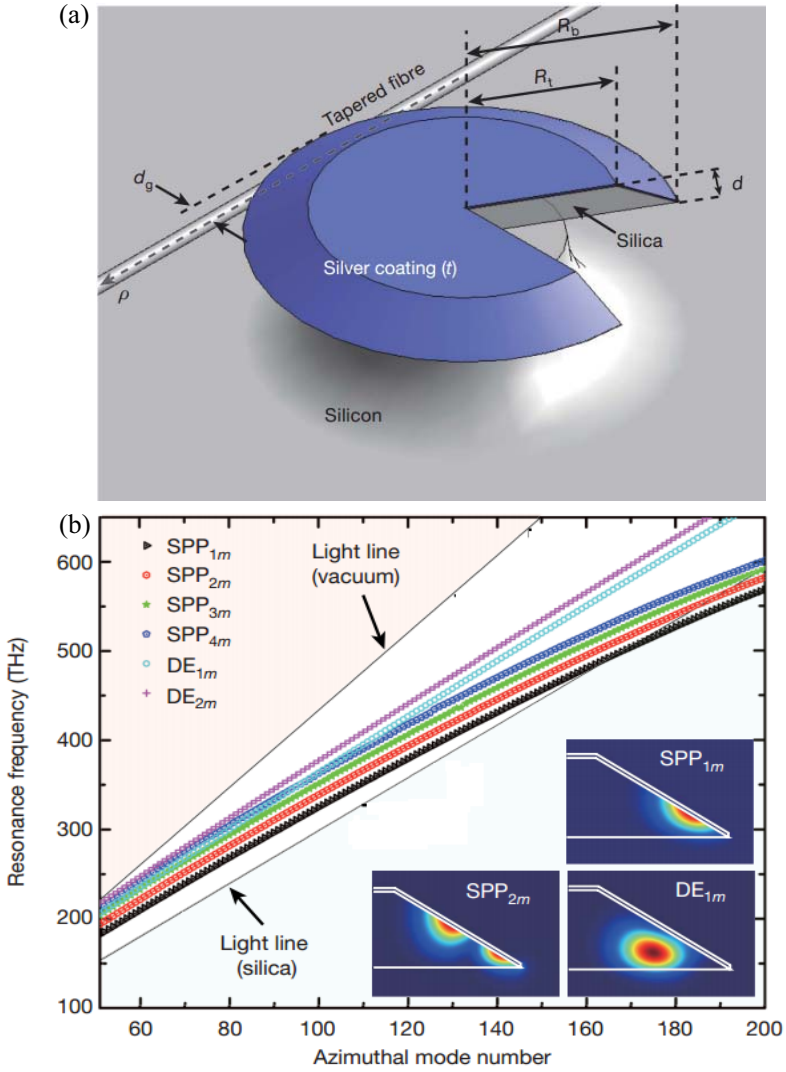

Figure 1.7: (a) A metal-coated whispering-gallery micro-disk and (b) the whispering-gallery modes supported by the disk. Both LSPs (SPP branches) and conventional photonic (DE branches) modes are supported with the corresponding mode profile shown in the inset. After Ref. [30].

tion between SPPs and LSPs is not absolute. For example as we mentioned earlier, when continuous plasmonic waveguides are truncated or wrapped, LSPs can be supported. At the same time, a chain of coupled LSPs resonances can be characterized by well defined dispersion curves and thus be used for subwavelength energy guidance [33–35]. In Fig. 1.9(a) we show the dispersion curves of a chain of coupled dipolar LSPs resonances. Both the results for longitudinal and transverse dipole orientations are shown. Figure 1.9(b) shows the experimental observation of energy transportation through a chain of metal nanoparticles. Compared to the result of a single metal particle, the effect of wave guidance by the chain is obvious.

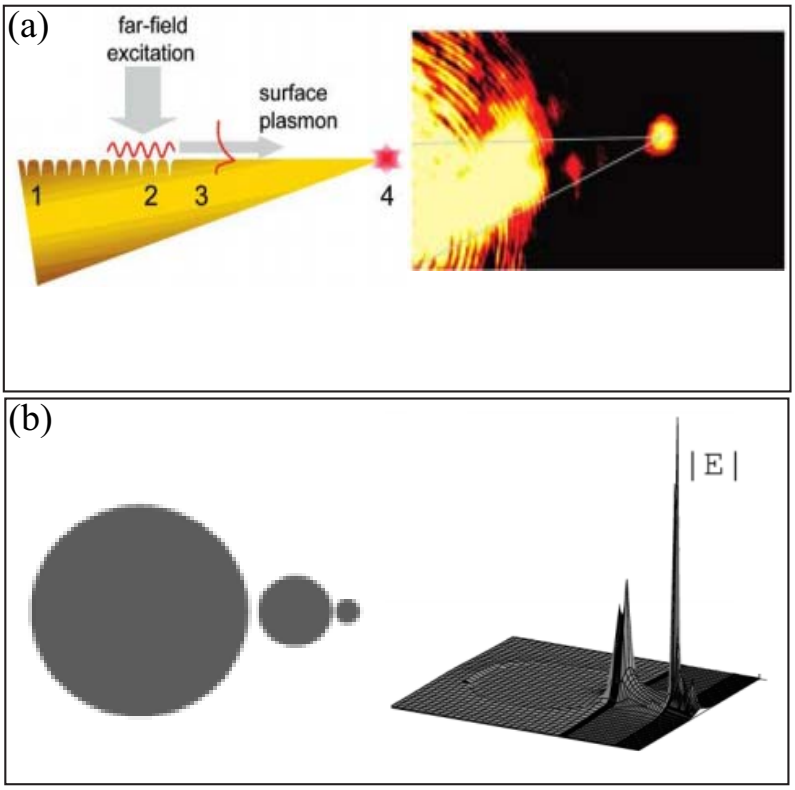

Figure 1.8: (a) Nanofocusing of SPPs modes in a tapered metallic tip through grating coupling with experimental result shown on the right. (b) Nanofocusing of LSPs resonances through a chain of metal nanospheres with decreasing sizes. The effect of field enhancement is shown on the right. After Refs. [31, 32].

1.3 Achievements and major challenges in plasmonics

Nowadays the field of plasmonics (both the branch of SPPs and LSPs) is developing and expanding faster than ever before. One of the driving forces behind this trend is the benefits of miniaturization and integration of optical circuits with electronic ones [12, 36, 37]. To highlight the importance of plasmonic structures, Figure 1.10 shows the typical physical limitations of different technologies based on different materials for computing and communication. Semiconductor electronics can operate in the nanometer regime, but the working speed is constrained by heat generation. Conventional photonic circuits based on insulators can work with a high operating speed, while cannot be miniaturized beyond the diffraction limit (see also Fig. 1.1). Plasmonic structures can avoid the disadvantages mentioned above and combine the advantages. In other words plasmonic structures can confine states excited down to the nanometer scale and can operate with a high speed, thus are expected to effectively bridge the field of nano-electronics and photonics. Another driving force for the rapid development of plasmonics is the new emerging field of metamaterials [20–22], where plasmonic items play a vitally important role to support both electric and artificial magnetic responses.

Due to the special features of plasmonic structures mentioned above, the demon-

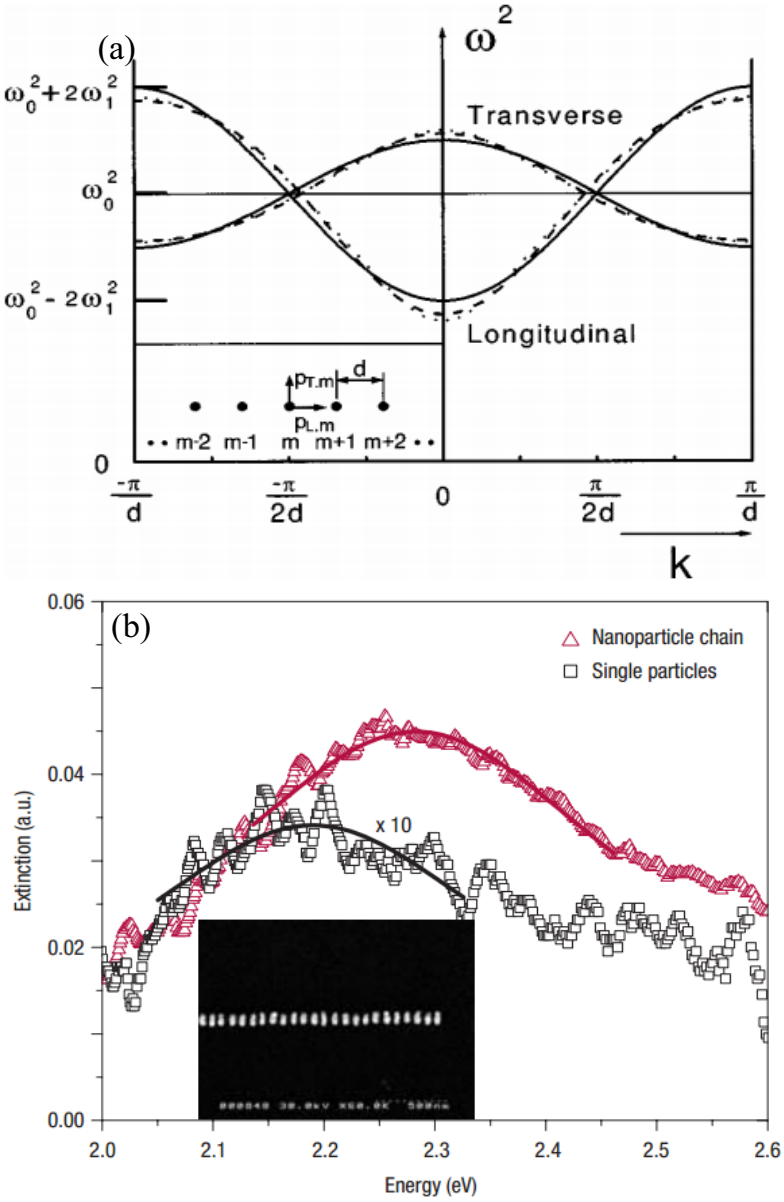

Figure 1.9: (a) Dispersion curves for coupled dipolar LSPs resonances for both longitudinal and transverse dipole orientations. (b) Experimental observation of energy guidance through a chain of metal particles. For comparison the result of a single metal particle is also presented. After Refs. [34, 35].

stration of plasmonic circuits based on various metallic waveguides [12, 28, 37, 38] is quite noticeable and deserves specific mention here. Figure 1.11 shows three kinds of plasmonic circuits based on channel SPPs [12, 37] which are confined within V-shaped grooves cut into planar metallic plates including plasmonic Y-splitter [Fig. 1.11(a)], plasmonic Mach-Zehnder interferometer [Fig. 1.11(b)] and plasmonic ring resonator [Fig. 1.11(c)]. More functionalities can be achieved through combining those three circuits or fabricate other plasmonic structures. Based on those

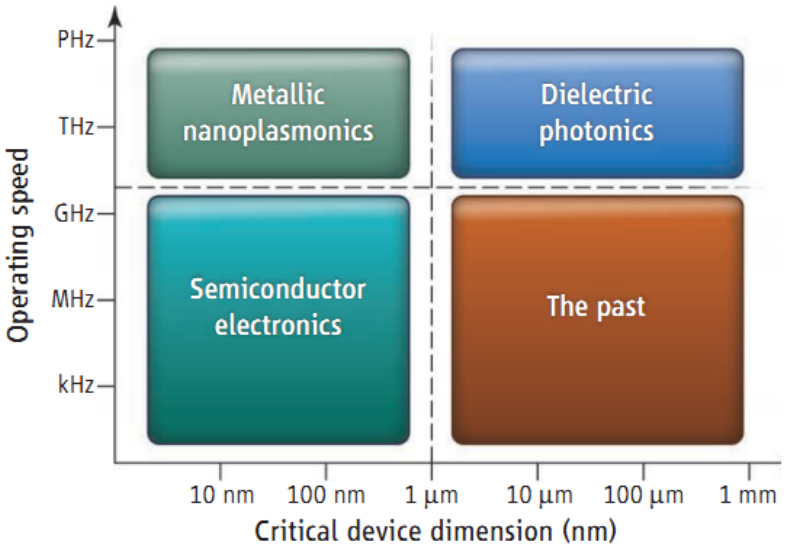

Figure 1.10: The typical size and operating speed of four different research domains, which have different physical limitations in terms both size and operating speed and those limitations are indicated by dashed lines. After Ref. [36].

circuits we can split and bend radiation sharply, and possibly realize ultra-compact plasmonic components which can be integrated with nano-electronic devices, and thus paving the way for a new class of integrated optical circuits.

The plasmonic waveguides demonstrated in Fig. 1.11 are effectively passive, which however can be made active through incorporating gain or nonlinear materials for various applications, including high-harmonic and ultra-short pulse generation, switching, loss compensation and so on [39–48]. The recent demonstration of nanoscale plasmonic lasers is a quite significant step [49, 50]. As mentioned above, a localized plasmonic state can be supported when the Bohr condition is satisfied and such a state can be confined down to a region in the subwavelength regime. In this confining region, if materials with gain are incorporated and when the threshold is reached, lasing effect will be present. Figure 1.12 shows two platforms where lasing effect is observed. In the first platform [Fig. 1.12(a)] the plasmonic states are confined within a Fabry-Pérot cavity between the semiconductor nanowire (CdS) and the Ag plate, where the CdS nanowire is doped, serving also as the gain material. In the second platform [Fig. 1.12(b)] the plasmonic states are confined at the surface of the gold core and the outmost layer is doped silica working as the gain material. The lasing effect within the deep subwavelength cavities renders the opportunity to study the light-matter interaction in the extreme dimension and sheds light on many laser related applications.

Plasmonic structures are also widely used for sensing [16, 51–55], imaging [56, 57], nanoantennas [58, 59], photovoltaic devices [60], and flexible phase front engineering [61, 62]. As an example, in Fig. 1.13 we show two plasmonic sensing devices based on SPPs modes and LSPs resonances respectively. It is known that plasmonic states are confined at the metal-dielectric interface and those states are

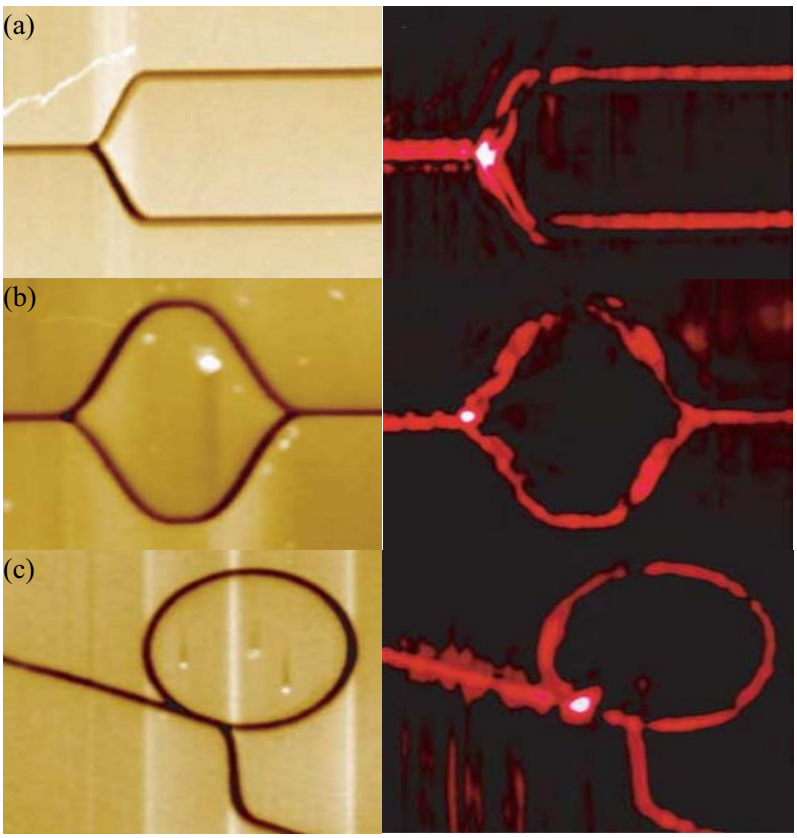

Figure 1.11: Experimental demonstration of three kinds of plasmonic circuits based on channel SPPs. (a) Plasmonic Y-splitter. (b) plasmonic Mach-Zehnder interferometer. (c) plasmonic ring resonator. After Ref. [37].

very sensitive to the surrounding environment close to the interface. Figure 1.13(a) shows a protein density sensing device based on the Kretschmann geometry for SPPs modes excitation. Different protein density in the upmost channel will lead to different SPPs propagation constants [see Eq. (1.5)] and thus different incident angle of the incident beam is required to excite effectively the SPPs modes. Thus different incident angles will be used to sense the change of the protein densities. Figure 1.13(b) shows another sensor based on the LSPs resonance supported by the Au triangle. For different pressures, different proportions of Hydrogen will be absorbed by the Pd disk. As the disk is close to the edge of the Au triangle where there is a significant field enhancement and high density of states, this will lead to scattering spectral peak shift of the sensing system. Consequently, the scattering spectra can be used to effectively sense the change of the pressure.

It is worth mentioning that plasmonics based applications can be found not only in different branches of physics, but also in frontier researches in chemistry, biology and medicine [15, 60, 63, 64]. Figure 1.14 shows a proposal for breast cancer therapy [15]: plasmonic core-shell nanoparticles resonant at the near-infrared spectral regime (inset of Fig. 1.14) are injected into the bloodstream and then those particles will flow mainly to the new-grown tumor. Under the illumination of a laser

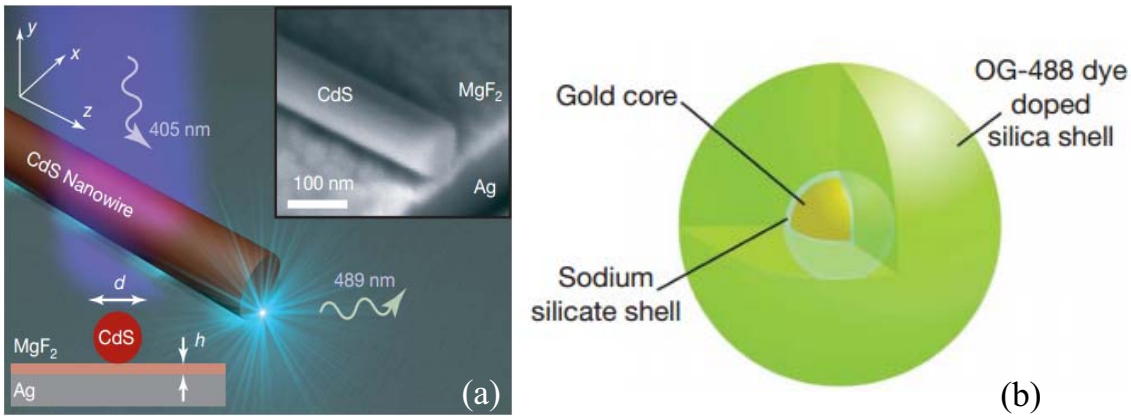

Figure 1.12: Experimental demonstration of plasmonic nano-lasers in (a) the plasmonic states are confined within the Fabry-Pérot cavity made of MgF_2 between the doped CdS nanowire and the Ag plate and in (b) the plasmonic states are confined at the surface of the gold core and the outmost layer is doped silica working as the gain material. After Refs. [49, 50].

of central wavelength close to the resonant wavelength of the injected particles, due to the excitations of LSPs resonances, the particles will generate heat to kill the tumor cells. As the particles are mainly embedded into the tumor issue, the healthy tissue will not be harmed by this heating effect.

The research of plasmonics during the past several years has become more comprehensive and has rapidly spread into the quantum regime [65–73]. It is worth noticing that in this field despite all the significant achievements, there are still many challenges laying ahead, with the major and tough ones described below:

Although the field of plasmonics provides an effective way for us to gain access to the regime in the nanoscale with its special feature of subwavelength confinement, and many flexible functionalities based on the feature of significant near-field enhancement, there is an inevitable trade-off between subwavelength confinement and the intrinsic loss of metals. A well known approach proposed to compensate for the loss is to incorporate gain materials [44, 74], while the side effects of the gain materials on the signal processed are not clear. An example of the side effects is the effect of gain materials on the quantum noise of the system investigated [44]. At the same time, the narrow operating spectral regime of the gain media and the requirement of an external pump will probably further restrict the applications of gain-assisted plasmonic devices.

Related to plasmonic structures with gain materials, the topic of lasing effect, especially the concept and demonstration of lasing spaser currently has become quite hot but at the same time also quite controversial [44, 49, 50, 77–83]. The controversy is not only about the basic concepts of the lasing effect [44, 77, 79–83] but also about the recent experimental demonstrations of such effect [49, 50]. In Ref. [49] Noginov *et al.* claimed that for the first time they have demonstrated the lasing spaser [Fig. 1.12(b)], while it is not clear what is really the lasing mechanism in that paper. The feedback can come from a single particle as it supports well defined

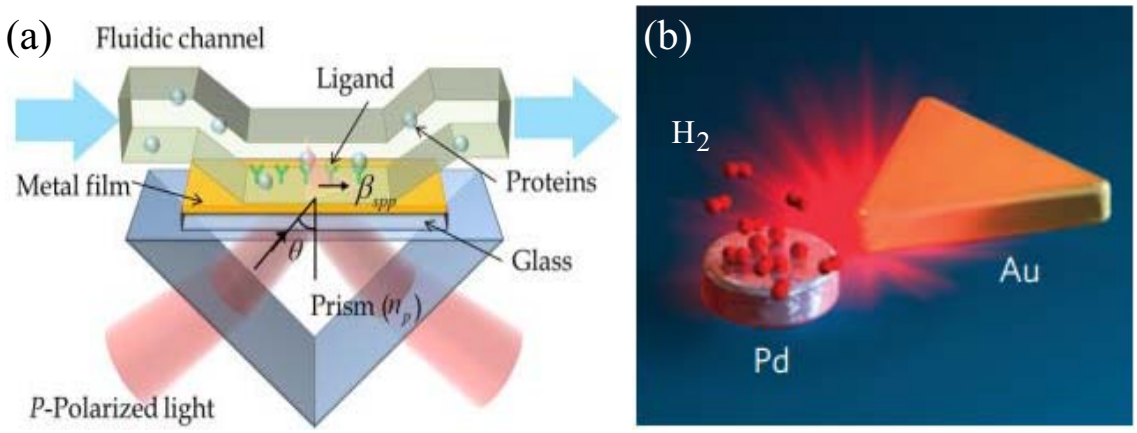

Figure 1.13: (a) A protein density sensor based on the Kretschmann geometry for SPPs modes excitation. Different protein densities will lead to different SPPs propagation constants and thus different incident angles are required to excite efficiently the SPPs modes. (b) A pressure sensor based on the resonant scattering of Au triangle. Different pressures will lead to different amounts of Hydrogen to be absorbed and thus lead to the shift of the scattering spectra. After Refs. [75, 76].

resonances, or from the random arrangement of all the particles (a random laser), or both feedback effects can be present. To rule out the mechanism of random lasing, a single particle lasing structure can be investigated but it is challenging to prepare a satisfactory experimental platform for such a test. The demonstration in Ref. [50] is quite decisive and clear [Fig. 1.12(a)], but it is argued that this demonstration is based on propagating SPPs rather than localized surface plasmons, and thus can only be called a plasmonic laser rather than a lasing spaser. There have been no clear conclusions yet about the debates mentioned above, while for the demonstrations in Ref. [49] and Ref. [50] we cannot see the fundamental differences between them. As we mentioned earlier of the Bohr condition, the resonances of both structures come from the integral number of 2π phase accumulation of SPPs. The only difference is that in the former structure phase is accumulated at the spherical metal-dielectric interface of the core-shell particle while in the latter one the phase is accumulated in a loop in the planar Fabry-Pérot cavity. But this difference is not sufficient for the justification of the claim that one of them is lasing spacer and the other is not.

The challenges of the field of plasmonics come not only from the intrinsic loss, but also from other special features of metals, such as nonlocality, quantum effect, nonlinearity and so on. To simplify the calculations of plasmonic structures, usually we assign to the metals effective permittivities and then all the properties can be obtained directly through solving Maxwell equations. For the effective permittivities of metals, in most classical investigations we take the experimental data of bulk metal or simply use the Drude model, the assumption behind which is that the free electrons show a δ-function type distribution and thus the electron pressure due to inhomogeneous electron distribution is neglected [27]. This approach works well under most circumstances when the scale of metallic items used is above the nanometer regime. However for structures with metallic items of scales in the sub-nanometer

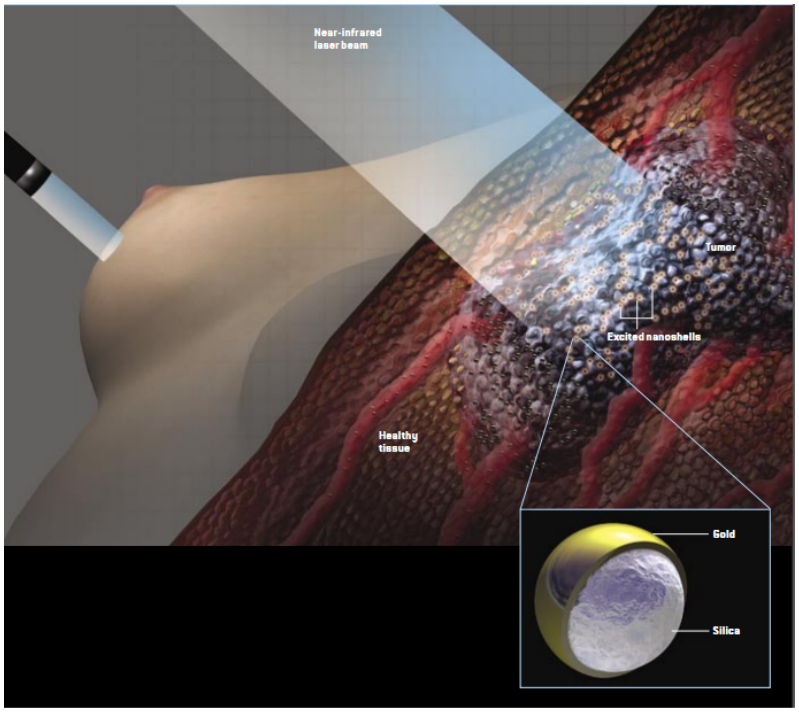

Figure 1.14: Plasmonics based cancer therapy: plasmonic silica core-gold shell nanoparticles (inset, those particles are made to be resonant in the near-infrared spectral regime) are injected into the bloodstream and then those particles will mainly be embedded into new-grown tumor tissue. Afterwards, a laser of central wavelength close to the resonant wavelength of the injected particles is shined to the region of tumor tissue. As the LSPs resonances of the particles injected are excited, the particles will generate sufficient heat to kill the tumor cells. After Ref. [15].

regime, the nonlocal effects of metals have to be taken into consideration [27, 84–87]. The Bloch hydrodynamic model has been widely used to address the nonlocal effects of metals, in which an extra term is introduced to include the pressure of the electron gas coming from inhomogeneous distribution [27]. The problem of this model is that there is some uncertainty in regard to what should be the proper pressure coefficient and after the application of this model, what should be the proper continuity condition: continuity of the field or continuity of the current [27]. There are still a lot of things to be done to improve this model, given that this model will be even more complicated when the quantum tunneling effect joins to be mixed with the nonlocal effect [70–73].

Despite the nonlocal and quantum effects of metal, another challenge comes from the nonlinearities of metal. There is significant near-field enhancement within plasmonic structures, which can thus be made highly active and functional when nonlinear effects are employed [21, 22]. For this kind of applications the nonlinearity of metal can play a significant role. However, similar to the nonlocal effect, it is quite challenging to characterize accurately the nonlinear effects of the metals [88–92]. This will become even more challenging in the sub-nanometer regime where nonlocal and quantum effects are present at the same time.

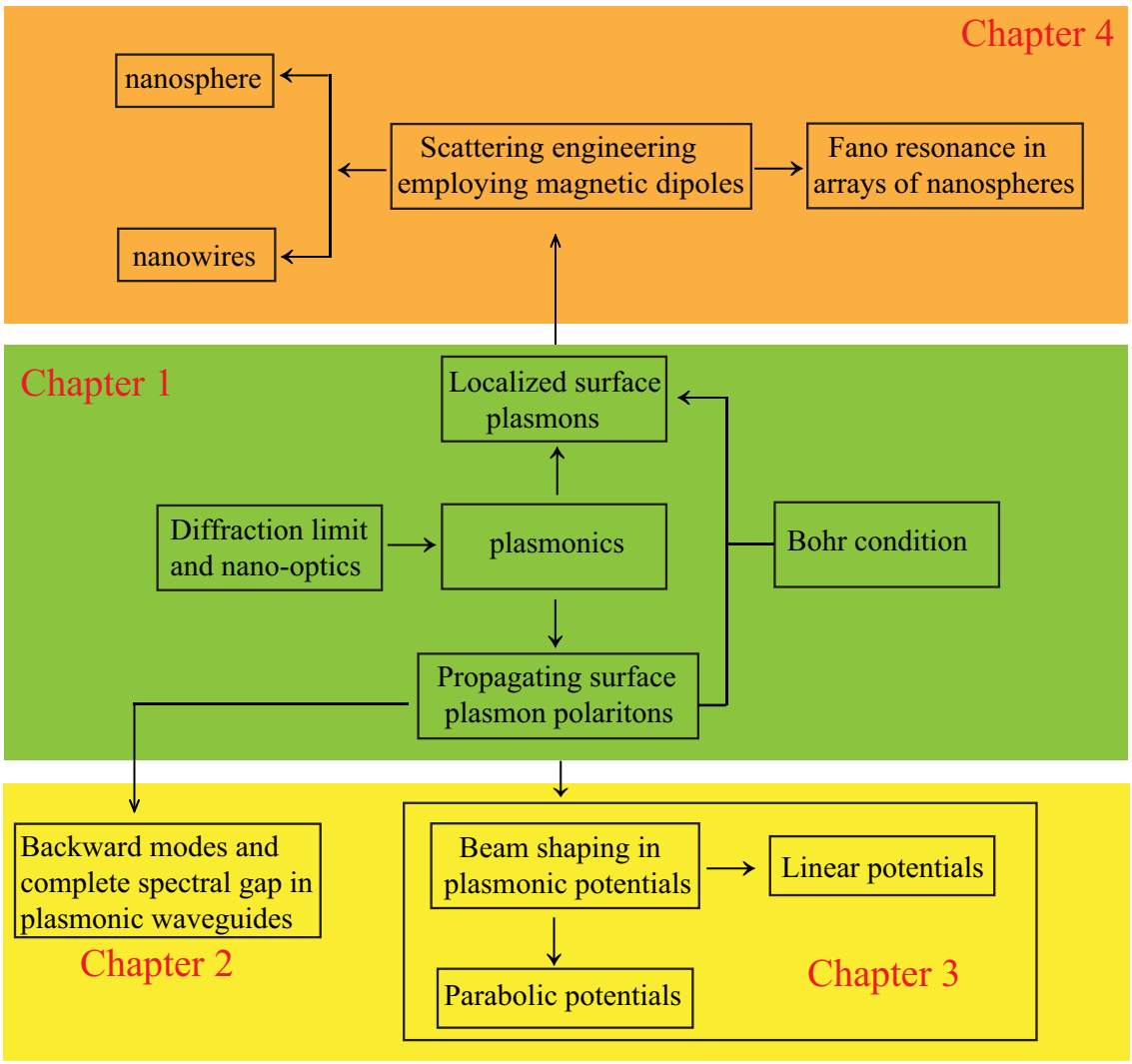

Figure 1.15: Schematic illustration of the structure of this thesis. We start the thesis with introduction to diffraction limit and nano-optics, of which the field of plasmonics is a promising and fast developing field. The field of plasmonics can be roughly divided into two branches of SPPs and LSPs, depending on whether the states excited are localized or propagating. The two sub-branches are highly related to each other through the Bohr condition. The SPPs related work is presented in Chapter 2 on backward modes and complete spectral gap, and in Chapter 3 on beam shaping in plasmonic potentials. LSPs related work is presented in Chapter 4 on scattering engineering through employing magnetic dipoles.

1.4 Scope and outline of this thesis

The research work presented in this thesis attempts to attack several specific challenges for both branches of SPPs and LSPs in the field of plasmonics as listed below:

(1) Spectral gap is an important concept in photonics, which in general indicates a spectral regime within which the electromagnetic waves cannot propagate

through. A special and most popular kind of spectral gap is bandgap in photonic crystals, which is playing a vitally important role for various applications, including the suppression of the spontaneous emission, photonic crystal laser, waveguiding in photonic crystal fibers and so on [93–95]. The realization of spectral gaps, similar to bandgaps, usually requires complex configurations like periodicity and thus complicated fabrication techniques. In Chapter 2 we demonstrate a new way to achieve spectral gaps without periodicity in the propagation direction. The basic mechanism is the coupling of backward and forward modes in plasmonic waveguides, for which there is automatic phase matching without any extra periodicity. We demonstrate both polarization-dependent and polarization independent complete spectral gaps in coupled plasmonic nanocavities.

(2) To realize the effective integration of plasmonic circuits with electronic device, an important step is to achieve flexible plasmonic beam shaping and steering [12, 28, 37]. There are a number of approaches for beam manipulations, such as employing nonlinear media [45] and bending the plasmonic waveguides [12, 28, 37]. However the drawbacks of those approaches are very clear: the nonlinear effects are usually very weak and highly dependent on the intensity of the signal, and bending the waveguides will induce huge extra scattering losses. In Chapter 3 we achieve various plasmonic potentials (graded index distribution) in modulated metal-dielectric-metal structures and based on such potentials we demonstrate efficient beam shaping and steering, including polychromatic nanofocusing in full parabolic potentials, plasmonic analogue of quantum paddle balls in half parabolic potentials, adiabatic nanofocusing in tapering parabolic potentials and plasmonic Airy beam manipulations in linear potentials.

(3) For many LSPs based applications, such as plasmonic nanoantennas [58, 59], sensing with plasmonic nanoparticles [52], and photovoltaic devices [60], clocking [96], control of the direction of the scattered light [61, 62] and so on, efficient shaping of the scattering pattern is one of the most crucial issues. Nevertheless, most approaches on scattering shaping are based on engineering of the electric responses of the nanostructures. This is because most structures have only electric responses as there are very limited kinds of magnetic materials, which at the same time can usually only operate in narrow spectral regimes, and are accompanied by high losses. In Chapter 4 we introduce the artificial magnetic dipoles into plasmonic nanostructures and manage to effectively shape the scattering pattern, through the interferences of electric and the artificial magnetic dipoles, for magneto-electric core-shell nanospheres and core-shell nanowires. We also demonstrate polarization independent Fano resonances in arrays of core-shell nanospheres.

For a clear overview of the thesis, in Fig. 1.15 we give a schematic illustration of the basic structure of the thesis: firstly we put the overall introduction of plasmonics in the broader background of diffraction limit and nano-optics; The field of plasmonics could be roughly divided into two branches of SPPs and LSPs, which can be unified through the Bohr condition of quantization; Chapter 2 about backward modes and complete spectral gap in plasmonic structures and Chapter 3 about beam shaping in plasmonic potentials fall into the category of SPPs; Chapter 4 about scattering engineering through employing magnetic dipoles falls into

the other category of LSPs. The thesis is concluded in the last chapter, where we summarize the results and give a brief outlook of the field of plasmonics.

CHAPTER 2

Backward modes and complete spectral gaps in cylindrical plasmonic nanostructures

The spectral gap in general means a spectral regime within which the electromagnetic waves cannot propagate through. One of the most well known examples of spectral gaps is the bandgap in photonic crystals. The spectral gap can basically block the flow of photons, and such functionality plays a central role in various photonic structures, based on which many applications can be realized, such as photonic crystal laser, wave guidance in photonic crystal fibers, suppression of spontaneous emission, color changing paints and so on [93–95]. However, the realization of spectral gaps, similar to bandgaps, usually requires configurations like periodicity and thus relatively complicated fabrication techniques. Moreover, such structures that support spectral gaps are hard to be further miniaturized in the optical regimes and thus challenging to be integrated with electronic devices. In this chapter we demonstrate a new mechanism to achieve spectral gaps based on the coupling of backward and forward modes. As there is automatic phase matching, no periodicity in the propagation direction is required. We demonstrate both polarization-dependent and polarization independent complete spectral gaps in coupled plasmonic nanocavities. The simpler mechanism is anticipated to be widely used to simplify the structure design for spectral gap based devices and play an important role in many possible related applications.

2.1 Introduction

In this part of introduction, we will start from the basic mechanism of bandgaps in photonic crystals and based on this we point out why backward modes are required to construct spectral gaps without periodicity in the propagation direction. Then we discuss the features of backward modes and their existence in planar layered plasmonic structures.

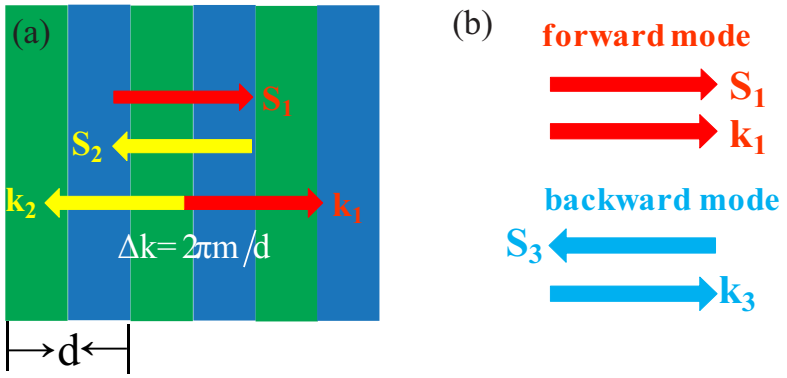

Figure 2.1: Schematic illustration of (a) the principle of the bandgaps in 1D photonic crystals and (b) forward and backward modes. $S_{1,2,3}$ indicates the direction of energy flows and $k_{1,2,3}$ indicates the direction of phase velocity.

Basic mechanism of bandgaps

To block the forward energy flow in one channel, there should be an extra channel coupled to the first one to transport energy backwards. To visualize this, in Fig. 2.1(a) we show schematically the mechanism of bandgaps in one dimensional (1D) dielectric photonic crystals. The existence of the bandgap depends on the coupling of two modes with contra-directional energy flows indicated by $S_{1,2}$ and wave vectors indicated by $K_{1,2}$. As both of the two modes are forward modes [the direction of the energy flow and wave vector is the same, as shown in Fig. 2.1(a)], energy flows into opposite directions also means that the two modes are not phased matched. To make the two modes effectively coupled to each other to produce the bandgaps, the periodicity of the photonic crystals (d) is required to provide extra momentum ($\Delta k = 2\pi m/d$, where m is an integer) to satisfy the phase matching condition ($k_1 - k_2 = \Delta k$). This explains intuitively and briefly why usually periodicity is required to make bandgaps. After the clarification of this point, it is easy to figure out that, if there is a mode (backward mode) which can transport the energy backwards while at the same time the wave vector is forward [as shown in Fig. 2.1(b)], then this mode will couple automatically to the forward mode directly without the need of periodicity to provide extra momentum. This means that spectral gaps can be achieved directly within systems where forward and backward modes are supported simultaneously.

Backward modes in planar layered plasmonic structures

With contra-directional energy flow and phase velocity, the backward modes sound quite unusual but actually they exist in our everyday life [97]. Recently boosted by the field of metamaterials [19–22], backward modes have attracted surging interest as they play a fundamental role for many novel phenomena observed in metamaterials, such as negative refraction, lens with super resolution, cloaking and so on [18–22, 57, 98–104]. The backward modes are supported in various plasmonic structures, where the negative permittivity of metals plays a central role. At the

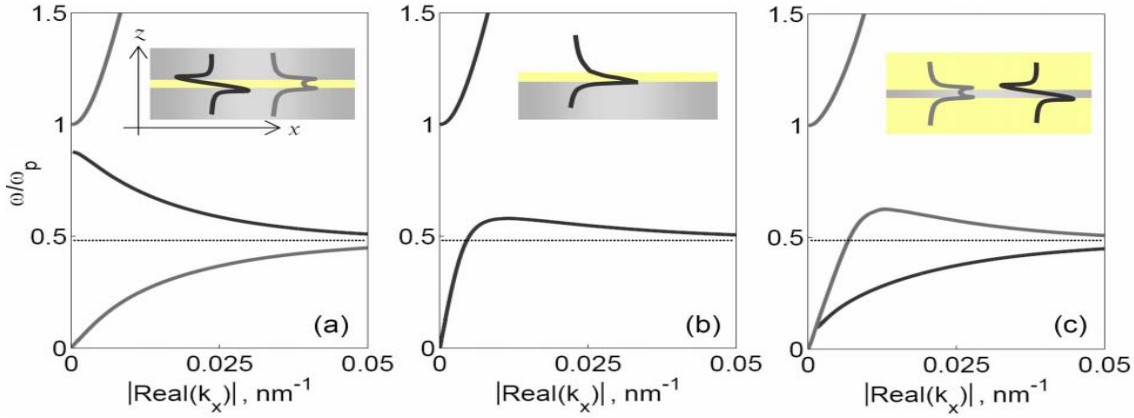

Figure 2.2: Backward modes (curves with a negative slope) in various planar plasmonic structures (grey regions indicate silver and yellow regions indicate GaP with other areas being vacuum): (a) a MDM waveguide with the GaP layer thickness of 50 nm, (b) a metal-dielectric-vacuum waveguide with the GaP layer thickness of 50 nm and (c) a DMD waveguide with silver layer thickness of 50 nm. The curves are plotted in lossless regime and dotted lines indicate the surface plasmon frequency. After Ref. [105]

metal dielectric interface, due to the negative permittivity of metals, the continuity condition requires the electric field component perpendicular to the interface in the dielectric should be opposite to that in the metal and this usually leads to contra-directional energy flows in the neighboring media. For a supported mode, when the overall backward energy flows in the metal is more than those forward ones in the dielectric, then the mode would be a backward mode.

In Fig. 2.2 we show the existence of backward modes (characterized by a dispersion curve with a negative group velocity) in three well studied planar structures: metal-dielectric-metal (MDM), metal-dielectric-vacuum, and dielectric-metal-dielectric (DMD) structures. As mentioned before, the backward modes are supported only when the overall forward energy flows is more than those backward ones and thus for the above three kinds of structures, to support backward modes specific structure parameters are required. We note that backward modes can also be found in other more complicated planar structures [106].

2.2 Backward modes in single cylindrical plasmonic nanostructures

In this section, we will study the simplest two cases of cylindrical plasmonic structures: nanowires and nanocavities, which actually are just 3D DMD and MDM structures respectively. Similar to their 2D counterparts [see Fig. 2.2(a) and (c)], we will show that both of them can support backward modes for specific structure parameters. In this section, to simplify the analysis and not lose the generality, we use the Drude model to simulate the optical properties of a metal: $\varepsilon_m(\omega) = 1 -$

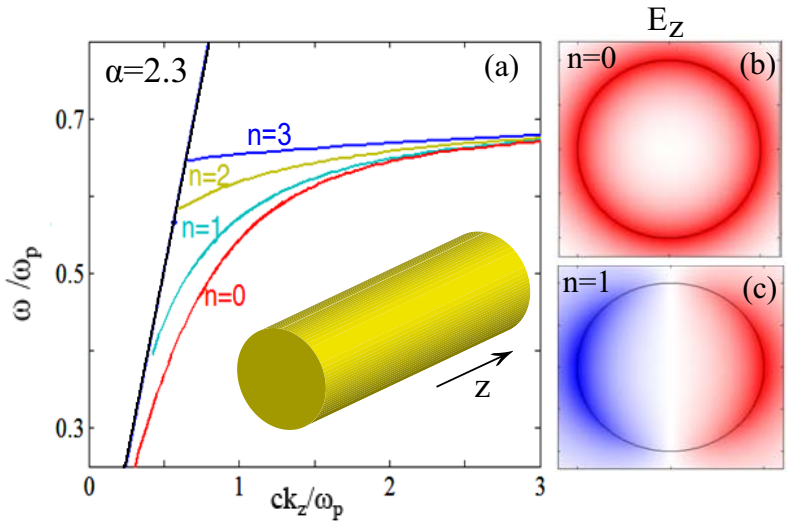

Figure 2.3: Modes of different orders supported by a metal nanowire [inset of (a)]. (a) The lossless dispersion curves of modes of different orders with fixed nanowire size $\alpha = 2.3$. The light line is indicted by the black curve. (b) and (c) show the electric field distribution (E_z component) for the fundamental and the dipole modes, respectively.

$\omega_p^2/\omega(\omega+i\omega_\tau)$, where ω_p is the plasma frequency and ω_τ is the collision frequency. At the same time, we define two normalized quantities: loss parameter $\gamma = \omega_\tau/\omega_p$, and size parameter $\alpha = R\omega_p/c$, where R is the radius of the the nanowire or nanocavity, and c is speed of light.

2.2.1 Plasmonic nanowires

Compared to 2D DMD structures in which one transverse direction is uniform, the cross section of a metal nanowire [inset of Fig. 2.3(a)] functions like a confining potential. Similar to confining potentials in quantum mechanics which lead to discrete states [24], plasmonic nanowires support SPPs modes of different orders (characterized by mode order n), with $2n$ nodes in the field distribution at the cross section [107–112]. Actually we can apply the Bohr condition at the cross section [111]. In Fig. 2.3(a) we show dispersion curves of modes of different orders with fixed nanowire size $\alpha = 2.3$ (which correspond to $R \approx 50$ nm for silver or gold, with plasma frequency $\omega_p = 1.37 \times 10^{16}$ rad/s) when the loss of metal is neglected ($\gamma = 0$). We are interested in only SPPs modes and thus the radiative modes on the left-hand side of the light line (indicted by black curve) are not shown (more details about the features of the radiative modes can be found in Ref. [107]). In Fig. 2.3(b) and Fig. 2.3(c) we show the electric field distribution (E_z component) for the fundamental and the dipole modes respectively. For this relatively large nanowire, none of the first four SPPs modes are backward modes. This means that for all the modes shown in Fig. 2.3(a), more energy flows forward in the dielectric background than that flows backward in the metal.

Next we change the parameters to search for backward modes supported by

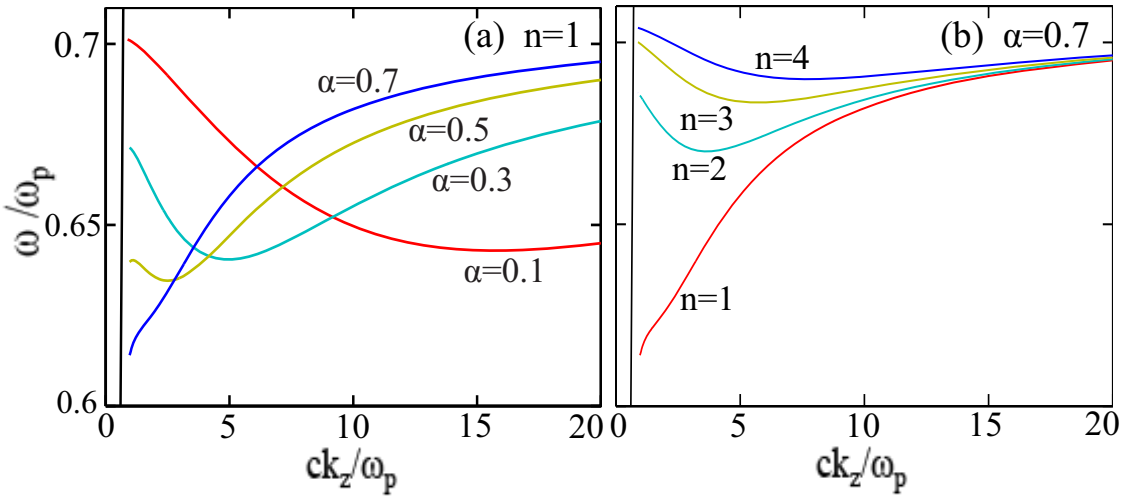

Figure 2.4: Lossless dispersion curves for (a) dipole modes supported by plasmonic nanowires with different sizes from $\alpha = 0.1$ to $\alpha = 0.7$ and (b) modes of different orders of the nanowire with fixed size $\alpha = 0.7$. The black line indicates the light line in vacuum.

plasmonic nanowires. It is known that the fundamental mode is always a forward mode [107–110] and thus firstly we focus on the dipole mode ($n = 1$) and change the size of the nanowires. We show the results in Fig. 2.4(a) and it is clearly shown that as we shrink the size of the nanowire, part of the dipole mode will become backward. Then we fix the size of the nanowire ($\alpha = 0.7$) and change the mode orders. As shown in Fig. 2.4(b), high order modes will become partly backward although the dipole mode is a fully forward mode.

Up to now, we have shown only the lossless dispersion curves when the loss of metal is ignored ($\gamma = 0$). There has been a lot of work about the effect of the loss of metal on the dispersion curves of the modes supported [113–116] and the general conclusion is that: when the group velocity is high, the dispersion curves will stay more or less the same as the lossless case while at the low group velocity region, the loss of metal will change significantly the dispersion curves. This is understandable as the slower energy flows, the more time it will has to interact with metal and thus more of the energy will be absorbed. In Fig. 2.5(a) we show the dispersion curves of the dipole mode supported by a metal nanowire of size parameter $\alpha = 0.1$ and the results of both lossy and lossless metal are shown. It is clear that when the group velocity is relatively large, the curves for the two cases are almost the same, but in the region close to the zero group velocity point, the curve will bifurcate into two branches.

To understand the nature of the two new formed branches, then we investigate the overall energy flows of the two branches. In lossless cases, the direction of overall energy flows is the same as that of group velocity [117, 118] and then it is easy to judge whether a mode is forward or backward through checking the slope of the dispersion curve. However, when loss is introduced in the system, the two directions of overall energy flow and of group velocity will be different [119] and

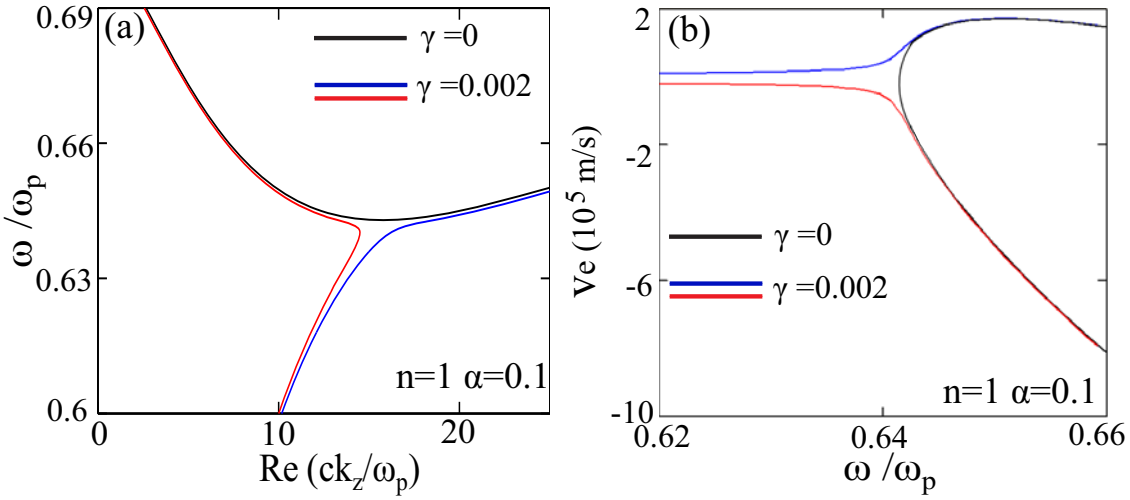

Figure 2.5: (a) Dispersion curves for dipole mode supported by nanowire with $\alpha = 0.1$ for both lossy ($\gamma = 0.002$) and lossless cases. When loss is present, the curve will bifurcate into two branches with forward energy flow (blue curve) and backward energy flow (red curve). (b) The energy velocity for lossless branch (black curve) and two lossy branches.

thus in lossy systems, to judge the direction of overall energy flow, we calculate the energy velocity of the modes supported by nanowires, which is defined as follows:

$$v_e = \frac{\int_0^R \int_0^{2\pi} rS_{zm}drd\theta + \int_R^{+\infty} \int_0^{2\pi} rS_{zd}drd\theta}{\int_0^R \int_0^{2\pi} rW_m drd\theta + \int_R^{+\infty} \int_0^{2\pi} rW_d drd\theta}, \tag{2.1}$$

where S_z denotes Poynting vector component along propagation direction, W denotes the energy density, and subscripts d and m denote the corresponding quantity in background dielectric and metal respectively. Energy velocity simply is the integrated energy flow divided by the integrated energy density, which is identical to group velocity $v_g = d\omega/dk$ [117, 118] in lossless case, while in lossy case v_g represents the velocity of the peak of a pulse which is not directly related to v_e [119]. In Fig. 2.5(b) we show the energy velocity for both new formed branches. It is clearly shown that one branch (blue curve) corresponds to a forward wave while the other branch (red) corresponds to a backward mode, which is independent of the group velocities of two branches. Also it is show that in the lossy case, the zero energy velocity is not accessible any more. We note here that there is another way based on the principle of causality together with the sign of the imaginary part of wavenumber, which makes it rather simple to tell the overall energy flow direction and thus the nature of the modes in lossy cases [120].

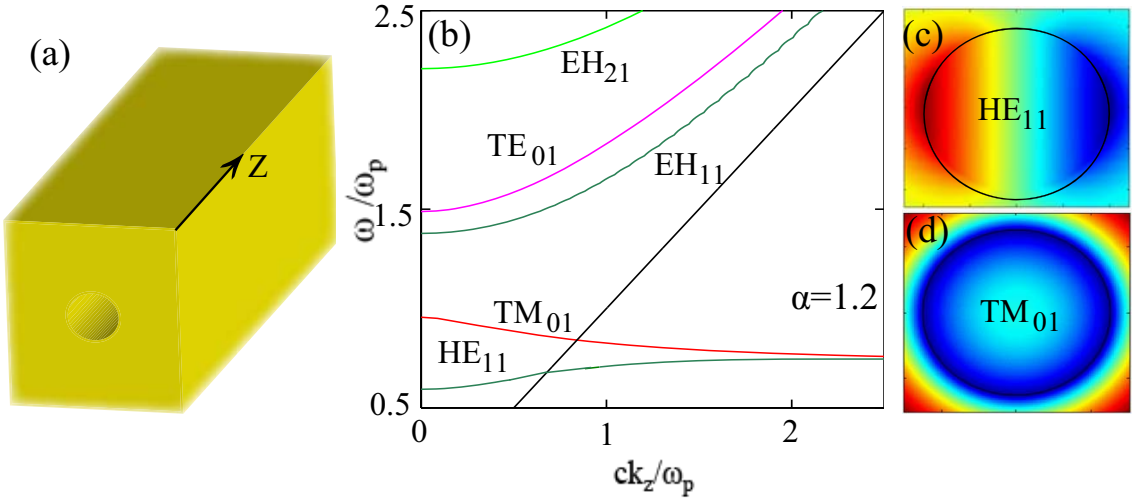

Figure 2.6: Dispersion curves in (b) indicate different modes supported by the plasmonic nanocavity [shown in (a)] with $\alpha = 1.2$ when loss of metal is neglected ($\gamma = 0$). (c) and (d) show the electric field distribution (E_z component) for the HE_{11} and TM_{01} modes, respectively.

2.2.2 Plasmonic nanocavities

Similar to the plasmonic nanowires, plasmonic nanocavities [schematically shown in Fig. 2.6(a)] support modes of different orders and many types of modes exist [108, 109]. The difference is that for modes supported by nanocavities, even the dispersion curves located on the left-hand side of the light line indicate nonradiative modes which are well confined within the cavity. This is because light cannot escape through the infinite metallic background. In Fig. 2.6(b) we show the lossless dispersion curves of different modes confined within the plasmonic nanocavity with size parameter $\alpha = 1.2$. More details about how those modes are named could be found in Refs. [108, 121]. In Fig. 2.6(c) we show the electric field distribution (E_z component) for the HE_{11} and TM_{11} modes, respectively, and we will give more details below about the two modes. The HE_{11} mode shows a typical dipole distribution while the TM_{01} mode shows an angular-invariant uniform distribution, which is a backward mode for the parameters chosen.

The nature of the modes (forward or backward) supported by the nanocavities is dependent on the sizes of the nanocavities, similar to the modes of nanowires as shown in Fig. 2.4. Next we study the evolution of the HE_{11} and TM_{01} modes with changing size parameters. Firstly we neglect the loss of metal and show in Fig. 2.7(a) and Fig. 2.7(b) the lossless dispersion curves for HE_{11} and TM_{01} modes respectively supported by plasmonic nanocavities of different size parameters. As it is clearly demonstrated, it is easier to support backward modes for shrunk size parameters, as is the case for nanowires, as shown in Fig. 2.4. Then we study the effect of loss on the dispersion curves for HE_{11} and TM_{01} modes and the results are shown in Fig. 2.7(c) and Fig. 2.7(d), respectively. As we claimed before, at relatively large group velocities, the effect of loss is not significant, while in the region close

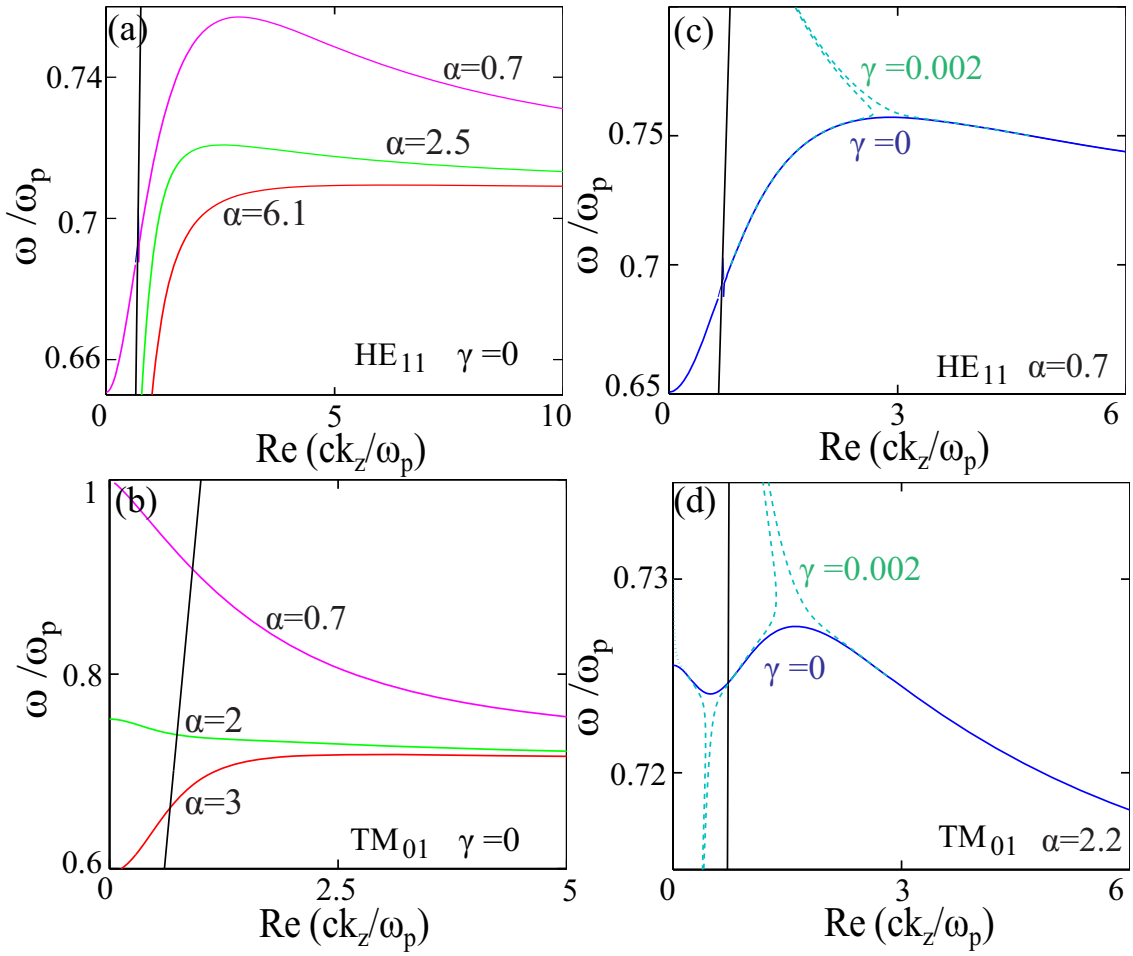

Figure 2.7: Lossless dispersion curves for (a) HE_{11} and (b) TM_{01} modes supported by plasmonic nanocavities of different size parameters. (c) and (d) show both the lossless and lossy dispersion curves for the two modes for a chosen size parameter.

to the zero group velocity point, the effect is not negligible any more. The mode bifurcation at the zero group velocity point shown in Fig. 2.7(c) and Fig. 2.7(d) when loss is present is a quite generic feature and has already been demonstrated for nanowires, as shown in Fig. 2.5.

Here we note that we use the Drude model to simulate the optical responses of metals, which does not work well when the size of the nanowire or nanocavity is in the sub-nanometer regime when nonlocal effect of metal has to be taken into consideration [27, 84]. Due to the nonlocal effect of metal the longitudinal modes can arise and SPPs modes can exist above the surface plasmon frequency [27, 84]. Though the results about nonlocal effects in cylindrical plasmonic structures will not be included in this thesis but published in a upcoming paper, we claim that even when nonlocal effect is taken into consideration, backward modes can still exist and the effect of loss on the dispersion curves, especially the zero group velocity point, is quite similar to what we have demonstrated earlier in Fig. 2.5 and Fig. 2.7.

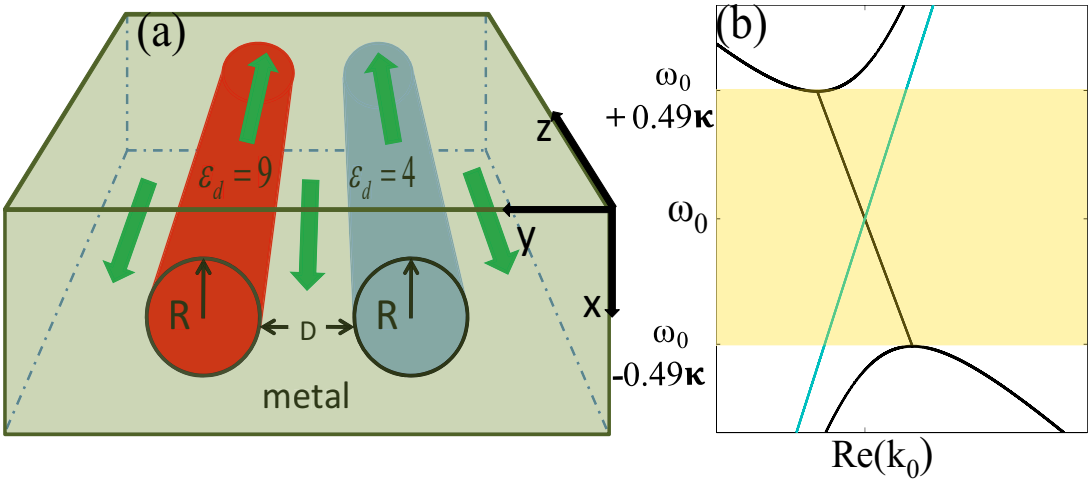

Figure 2.8: (a) Two dielectric waveguides with $\varepsilon_1 = 9$ and $\varepsilon_2 = 4$, separated by D embedded into infinite metal. Green arrows indicate the energy flow at different channels for the wave vector along z; (b) dispersion of two coupled waveguides. Yellow region indicates the incomplete polarization dependent spectral gap obtained using temporal coupled mode theory with $v_g = 0.13c$, $v_{g3} = -0.039c$, and $\delta = 0$, where c is the speed of light.

2.3 Spectral gap in coupled plasmonic nanocavities

In this section we study a plasmonic coupler involving backward (TM_{01}) and forward (HE_{11}) modes of dielectric waveguides embedded into an infinite metallic background (plasmonic nanocavities). The simultaneously achievable contra-directional energy flows and co-directional phase velocities in different channels lead to a spectral gap, despite the absence of periodic structures along the waveguide. We demonstrate that a polarization independent complete spectral gap can be achieved in a symmetric structure composed of four coupled nanocavities. This new mechanism demonstrated may play an important role in nanophotonics, as it could significantly simplify complex geometries that are required for subwavelength optical manipulation and concentration.

2.3.1 Polarization-dependent spectral gap in two coupled plasmonic nanocavities

Figure 2.8(a) shows the two-waveguide structure we study: two dielectric rods of the same radius $\alpha = 1.21$ (corresponding R is about 25 nm for silver) with $\varepsilon_1 = 9$ and $\varepsilon_2 = 4$ are embedded into infinite metal. Firstly, by analyzing the dispersion of a single waveguide, we find that the backward TM_{01} mode for $\varepsilon = 9$ intersects with the forward HE_{11} mode for $\varepsilon = 4$ at $\omega/\omega_p = 0.3856$ [see Fig.2.9(a)]. The HE_{11} mode has linear polarization inside the dielectric [see Fig. 2.9(c)], which could be excited directly with a normal incident wave [122], whereas the TM_{01} mode has

radial polarization [see Fig. 2.9(d)] with much higher losses in the coupling region [see Fig. 2.9(b)].

Prior to preforming a fully numerical study, we use temporal coupled mode theory [123, 124] (TCMT) to get a qualitative understanding of dispersion relation in the lossless case. The eigenmodes of a coupled system are expressed as a superposition of individual waveguide modes: $\mathbf{E} = \sum_m A_m(z,t)\mathbf{E}_m(x,y)e^{i(\omega_{m0}+\kappa_{mm})t}$, where $\omega_{m0} = \omega_m$ at $k = k_0$ and κ_{mm} is the self-coupling coefficient. For the two coupled waveguides, three modes can couple to one another: two forward HE_{11} modes of preferred x and y polarizations, which could be approximately reconstructed by two orthogonal eigenmodes of circular polarizations $A_{1,2}(z,t)$, and one backward TM_{01} mode $A_3(z,t)$. The coupled mode equations in time domain are:

$$i\frac{\partial A_{1,2}(z,t)}{\partial t} + iv_g\frac{\partial A_{1,2}(z,t)}{\partial z} + \kappa A_3(z,t)e^{i2\delta t} = 0, \tag{2.2}$$

$$i\frac{\partial A_3(z,t)}{\partial t} + iv_{g3}\frac{\partial A_3(z,t)}{\partial z} + \kappa\sum_{m=1}^{2} A_m(z,t)e^{-i2\delta t} = 0, \tag{2.3}$$

where $\delta = \frac{1}{2}(\kappa_{33} + \omega_{30} - \kappa_{11} - \omega_{10}) = \frac{1}{2}(\kappa_{33} + \omega_{30} - \kappa_{22} - \omega_{20})$ is the antisymmetry parameter of two waveguides; $A_{1,2,3}$ are normalized envelopes of the wavefunction; $v_{gi}(v_g = v_{g1,g2} > 0, v_{g3} < 0)$ are the group velocities at $\omega_0 = \omega(k_0)$; $\kappa_{12} = \kappa_{21} = 0$ (mode 1 and 2 are orthogonal), and the other mutual coupling coefficients are identical: $\kappa_{ij} = \kappa_{ji} = \kappa$ $(i = 1, 2;\ j = 3)$. In the coupling region we ignore the dispersion of group velocities and assume that $v_{g,g3}$ and κ are constants. By introducing the following variables: $a_1(z,t) = A_1(z,t)e^{-i\delta t}$, $a_2(z,t) = A_2(z,t)e^{-i\delta t}$, $a_3(z,t) = A_3(z,t)e^{i\delta t}$, Eq.(2.2) and Eq.(2.3) can be simplified as:

$$i(\frac{\partial}{\partial t} + \omega_1\frac{\partial}{\partial z})a_{1,2}(z,t) - \delta a_{1,2}(z,t) + \kappa a_3(z,t) = 0, \tag{2.4}$$

$$i(\frac{\partial}{\partial t} + \omega_{13}\frac{\partial}{\partial z})a_3(z,t) + \delta a_3(z,t) + \kappa\left[a_1(z,t) + a_2(z,t)\right] = 0. \tag{2.5}$$

Then we apply the Fourier Transform:

$$a_{1,2}(z,t) = (\frac{1}{2\pi})^2 \iint \hat{a}_{1,2}(k,\omega)e^{i\omega t - ikz} \tag{2.6}$$

and then Eq.(2.4) and Eq.(2.5) are transformed into the frequency domain:

$$\left[i(i\omega - i\omega_1 k) - \delta\right]\hat{a}_{1,2}(k,\omega) + \kappa\hat{a}_3(k,\omega) = 0, \tag{2.7}$$

$$\left[i(i\omega - i\omega_{13}k) + \delta\right]\hat{a}_3(k,\omega) + \kappa\left[\hat{a}_1(k,\omega) + \hat{a}_2(k,\omega)\right] = 0. \tag{2.8}$$

The eigenvalues of Eq.(2.7) and Eq.(2.8) can be easily found, which actually correspond to the propagation constants of the three eigenmodes supported by the coupled system:

$$k_{1,2} = \left(\alpha_1 \pm i\sqrt{-8v_{g3}v_g\kappa^2 - \alpha_2^2}\right)/2v_g v_{g3}, \qquad k_3 = (\omega + \delta)/v_g, \tag{2.9}$$

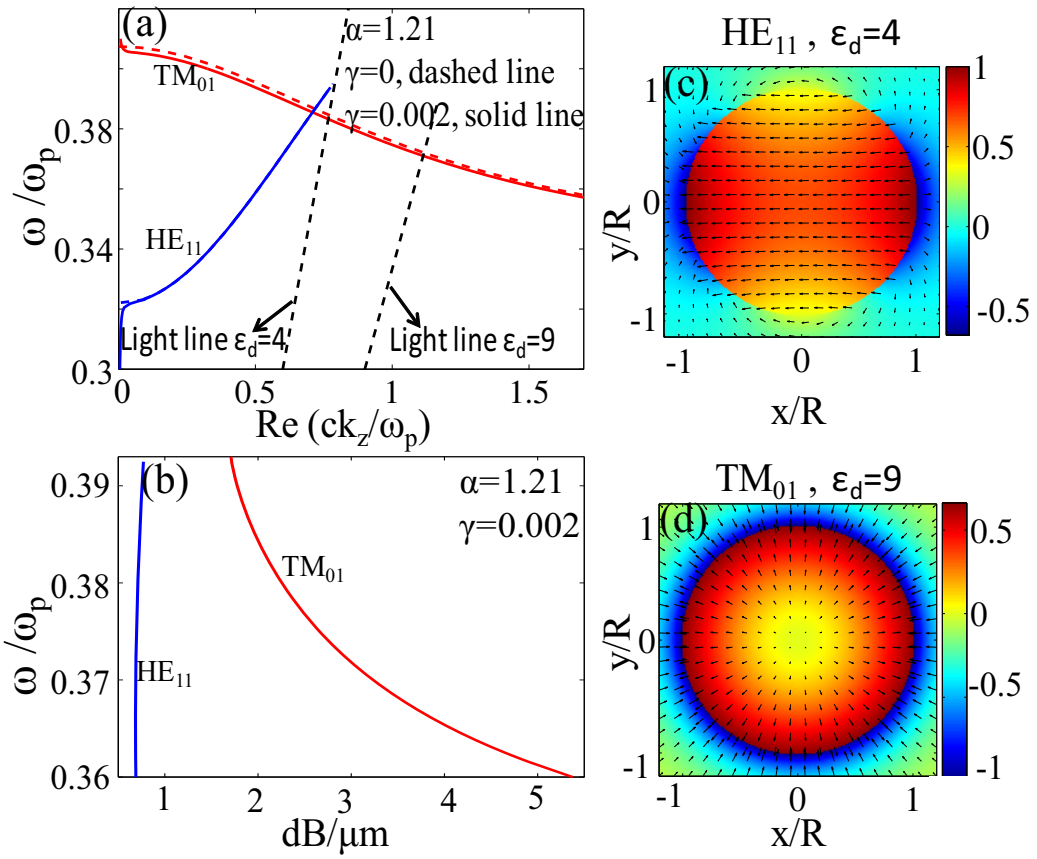

Figure 2.9: (a) Dispersion curve and (b) losses of TM_{01} mode for $\varepsilon_d = 9$ and HE_{11} mode for $\varepsilon_d = 4$. (c) and (d) Poynting vector component S_z (colourmap) and transverse electric field E_t (arrows) for HE_{11} mode and TM_{01} respectively at ω/ω_p=0.3856 with γ=0.002.

where $\alpha_1 = v_g(\omega-\delta)+v_{g3}(\omega+\delta)$ and $\alpha_2 = v_g(\omega-\delta)-v_{g3}(\omega+\delta)$. When $-8v_{g_3}v_g\kappa^2 \geq \alpha_2^2$, $k_{1,2}$ is a conjugate pair, indicating the existence of a spectral gap, while k_3 corresponds to the eigenmode:

$$\hat{a}(k,\omega) = \hat{a}_1(k,\omega) + \hat{a}_2(k,\omega), \tag{2.10}$$

where $\hat{a}_1(k,\omega)$ and $\hat{a}_2(k,\omega)$ denote orthogonal circularly polarized modes. Thus, k_3 corresponds to a linearly polarized HE_{11} mode, which is not coupled to the TM_{01} mode. This mode makes the gap dependent on the polarization. Figure 2.8(b) shows the results obtained using TCMT of $\delta = 0$ when values with $v_{g,g3}$ are extracted from the data shown in Fig. 2.9(a).

Full numerical simulation results using COMSOL (see Fig. 2.10) qualitatively agree with TCMT. In the lossless case $\gamma = 0$, the spectral gap is defined by a pair of complex conjugated propagation constants [see Figs. 2.10(a) and (b)]. The gap width increases with decreasing the distance D [see Fig. 2.10(f)], because the coupling coefficient becomes larger. When we incorporate some losses ($\gamma = 0.002$), all modes become complex, and the definition of width of the gap depends on how

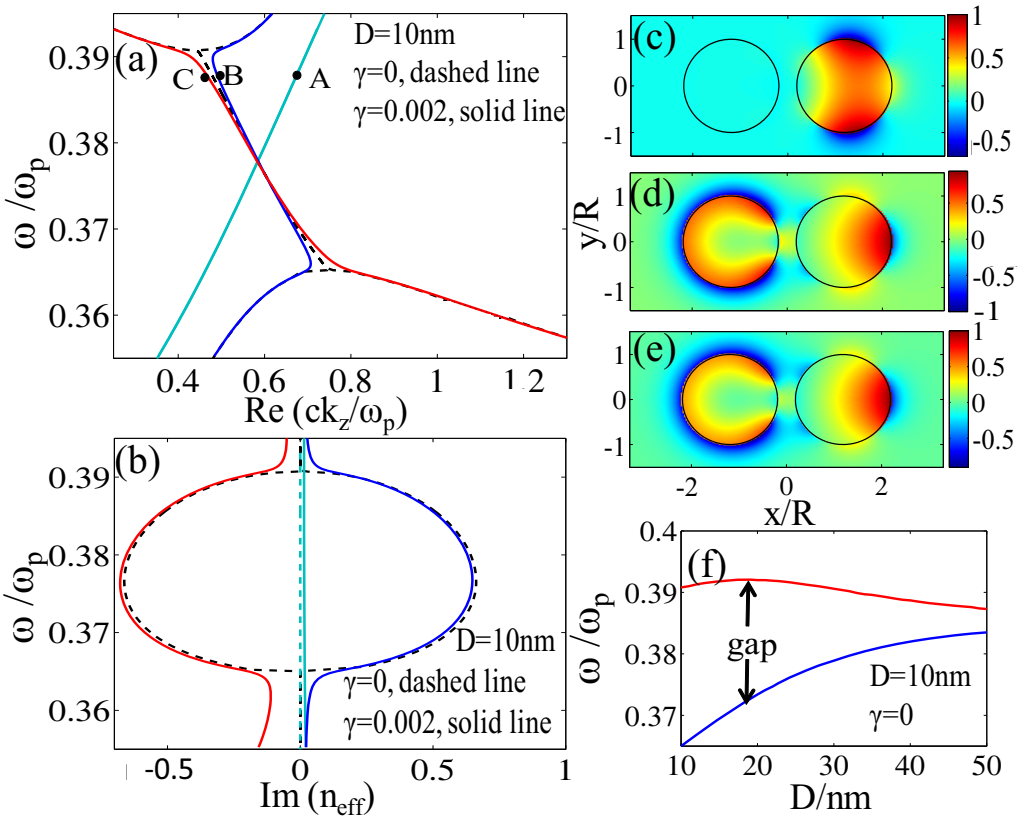

Figure 2.10: ((a) Dispersion and (b) losses (imaginary part of $n_{\text{eff}} = k_z/k_0 = k_z c/\omega$) of the three eigenmodes of the two-waveguide structure. Dashed black (γ=0), solid red and green (γ=0.002) curves correspond to modes of conjugate propagation constants. Blue curve (dashed curve almost overlaps the solid curve as the loss of this mode is comparatively low as shown in (b)) correspond to the HE_{11} mode that is not coupled to the TM_{01} mode as shown in (c). (c)-(e) S_z of modes at the points (A)-(C) marked in (a), respectively. (f) Gap region vs distance between waveguides when γ=0.

far it is from the observing point to the source. However, the gap width of lossless metal ($\gamma = 0$) may still serve as a guide and effective approximation as shown in Figs. 2.10(a) and (b) with dashed lines.

In addition to the modes of conjugate propagation constants, there exists one more HE_{11}-like decoupled mode. The energy flow of this mode is mostly confined inside $\varepsilon_1 = 4$ waveguide [see Fig. 2.10(c)]. Thus, the gap of the two coupled waveguides is incomplete and polarization dependent.

2.3.2 Symmetry induced polarization independent complete spectral gaps

To make modes of different preferred polarizations directions degenerate and obtain a full gap, symmetric structures could be used [125, 126]. One of the options

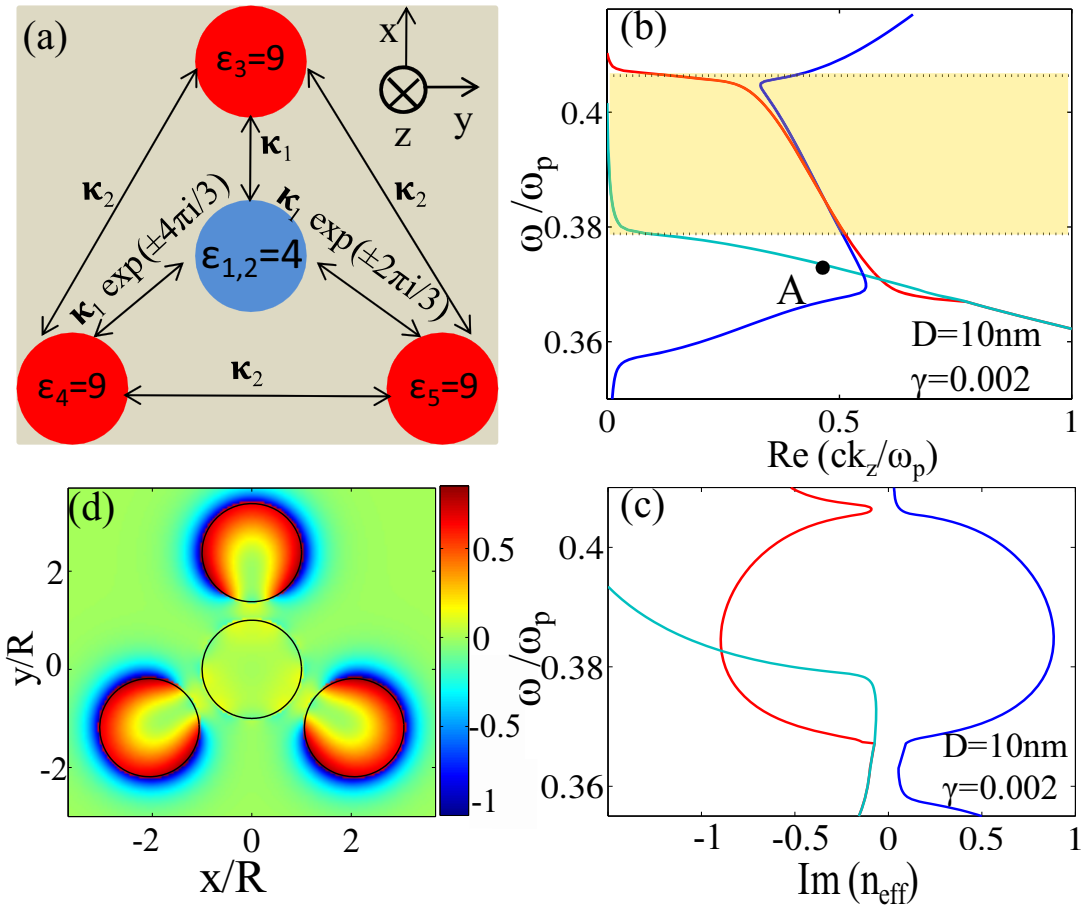

Figure 2.11: (a) Schematic of the four-waveguide structure with C_{3v} symmetry. The distance between $\varepsilon_{1,2}$ waveguide to $\varepsilon_{3,4,5}$ waveguides is D. (b) Dispersion and (c) losses of three eigenmodes. Blue curve corresponds to the E3 mode. The complete gap region in lossless case is colored yellow. (d) S_z of E3 mode at point (A) marked in (b).

is to utilize four-waveguide C_{3v} structure [see Fig. 2.11(a)]. We use subscripts $n = 1, 2$ to denote two HE_{11} modes of circular polarizations and $n = 3, 4, 5$ for three TM_{01} modes. Based on the symmetry and energy conservation law in the lossless case, the following relations are satisfied for mutual coupling coefficients:

$$\kappa_{12} = \kappa_{12} = 0, \quad \kappa_{1m} = \kappa_{m1}^* = \kappa_{2m}^* = \kappa_{m2} = \kappa_1 e^{\frac{2}{3}\pi(m-3)i}, \tag{2.11}$$

where $m, n = 3, 4, 5$ and $m \neq n$. Due to the C_{3v} symmetry, eigenmodes $\hat{a}(k, \omega) = \sum_{m=1}^{5} \beta_m \hat{a}_m(k, \omega)$ of preferred x polarization ($\beta_1 = \beta_2$) and those of preferred y polarization ($\beta_1 = -\beta_2$) should be degenerate [125, 126]. Thus using TCMT we can find five eigenmodes of three frequencies:

$$k_{1,2} = \left(\alpha_1 \pm i\sqrt{-12 v_{g3} v_g \kappa^2 - \alpha_2^2}\right) / 2 v_g v_{g3}, \tag{2.12}$$

which corresponds to two degenerate pairs of modes and the last mode of:

$$\omega = \omega_3(k) + 2\kappa_2. \tag{2.13}$$

Here $\alpha_1 = v_g(\omega - \delta + \kappa_2) + v_{g3}(\omega + \delta)$, $\alpha_2 = v_g(\omega - \delta + \kappa_2) - v_{g3}(\omega + \delta)$ and $\omega_3(k)$ is the dispersion of the individual TM_{01} mode. Again $k_{1,2}$ can be a conjugate pair, indicating the existence of a gap. $\omega = \omega_3(k) + 2\kappa_2$ corresponds to eigenmode (E3 mode) $\hat{a}(k,\omega) = \sum_{m=3}^{5} \hat{a}_m(k,\omega)$, which is a symmetric combination of TM_{01} modes. The cut-off frequency of E3 mode is shifted by $2\kappa_2$ compared with individual TM_{01} mode. Numerical results from COMSOL are shown in Fig. 2.11. This allows us to conclude that the spectral gap of four coupled waveguides indicated by the yellow region becomes polarization independent when the E3 mode is cutoff. For larger losses (metal in deep ultraviolet regime) the spectral gap still exists, but the effective width becomes smaller and eventually disappears as increasing losses make the differences between gap and non-gap region smaller. To enable coupling at longer-wavelength regimes, where losses of metal are lower, one could use dielectric waveguides with higher permittivities (GaAs or Si for example).

2.4 Summary

In this chapter after a brief introduction to backward modes and their existence in planar layered plasmonic structures, we study two basic plasmonic cylindrical structures: nanowires and nanocavities, and reveal the existence of the backward modes supported by them. We discuss the mode evolutions with size parameters and also the effect of loss of metal on the shape of the dispersion curves. Then we study a coupler based on two coupled nanocavities involving the coupling of backward and forward modes. By using the temporal coupled mode theory we have predicted a spectral gap in such a system without a periodic structure. This result has been verified by direct numerical simulations. Moreover, we have demonstrated that a complete polarization independent gap can be achieved by using four coupled nanocavities with C_{3v} symmetry. Similar coupling between surface plasmon polaritons (SPPs) can happen in metallic-wire structures when the radius is small enough to support backward SPPs modes. However, high losses of backward SPPs on metallic wires prevent them from realistic realizations. We anticipate that by incorporating materials with gain and/or nonlinearities, the proposed structure can be considered as a platform for the study of gap solitons, optical bistability, high-Q cavities, plasmonic nanolaser in various systems without periodicity.

CHAPTER 3

Beam shaping in plasmonic potentials

Flexible beam shaping and steering is an important functionality for plasmonic nanocircuits. The approaches proposed for beam shaping relying on employing nonlinear media or bending the plasmonic waveguides have severe drawbacks. For example, the nonlinear effects are usually very weak and highly dependent on the intensity of the signal, and bending the waveguides will induce extra scattering losses. In this Chapter we propose and demonstrate flexible and efficient beam shaping in plasmonic potentials. At the beginning we discuss the similarity between Schrödinger equation for matter waves and the paraxial wave equation for photons. We point out that the graded index plays the effective role of potentials for photons, similar to the potentials for matter waves. Then we introduce the concept of *plasmonic potentials* and demonstrate how to achieve different kinds of potentials for SPPs modes in various modulated metal-dielectric-metal (MDM) structures. We show firstly different kinds of parabolic plasmonic potentials in quadratically modulated MDM structures and the beam manipulations in such potentials, including polychromatic nanofocusing in full parabolic potentials, plasmonic analogue of quantum paddle balls in half parabolic potentials, and adiabatic nanofocusing in tapered parabolic potentials. In the last section of this chapter we show the existence of linear plasmonic potentials in wedged MDM structures and efficient steering of the Airy beams in those potentials.

3.1 Introduction

Formal scientific investigation on the similarities between classical particles and light date back to 1704 when Isaac Newton published his treatise *Optiks* [127]. This topic was further systematically studied by Hamilton and especially those founders of quantum mechanics, *e.g.* Einstein, Heisenberg, de Broglie, Schrödinger *etc* [118, 128, 129]. After the well establishment of quantum mechanics and the invention of the laser, many theories and concepts from quantum mechanics have been successfully adopted and demonstrated in the field of photonics (see, *e.g.* Ref. [130] and the references therein).

A well known example is the similarity between the scalar paraxial wave equation for photons and the Schrödinger equation [130–132]. The scalar paraxial wave

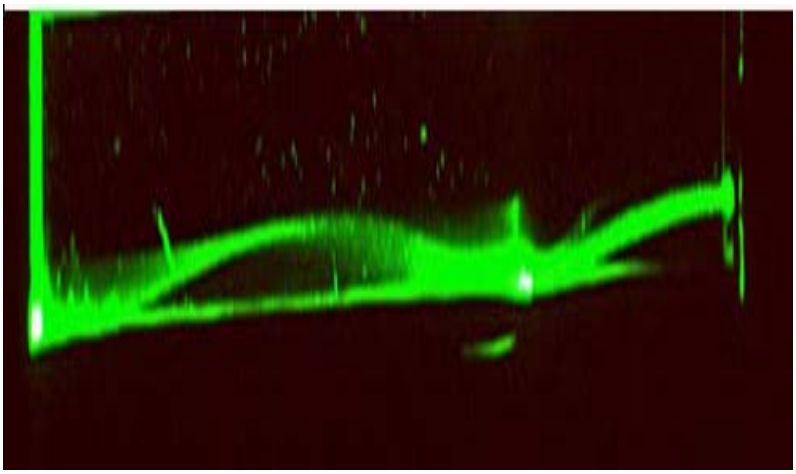

Figure 3.1: Photon bouncing under photonic gravity: The trajectory of a light beam ($\lambda = 532$ nm) through a tank of water filled with sugar. After Ref. [132].

equation is:

$$-i\frac{\partial\psi}{\partial z} = \left[k_0 n(x,z) + \frac{1}{2k_0 n(0,z)}\frac{\partial^2}{\partial x^2}\right]\psi, \tag{3.1}$$

where k_0 is the wavenumber in free space and $n(x,z)$ is the effective refractive index distribution. We note here that for the second-order partial derivation term of Eq. (3.1) we make the approximation that $n(x,z) = n(0,z)$ under the circumstance that the effective refractive index does not change significantly with x. For the case that the effective refractive index is independent of z, of which a special example is a uniform waveguide along z. The paraxial wave equation Eq. (3.1) can then be compared to the Schrödinger equation:

$$-i\frac{\partial\psi}{\partial t} = \left[V(x,t) + \frac{1}{2m}\frac{\partial^2}{\partial x^2}\right]\psi, \tag{3.2}$$

where $V(x,t)$ is the potential term for matter waves. If we compare Eq. (3.1) and Eq. (3.2) they are actually the same with the effective refractive index n playing the actual role as the potentials for matter waves. To directly visualize this similarity, in Fig. 3.1 we show a light beam passing through a tank of water filled with sugar [132]. Due to gravity, the density of sugar molecules will show a graded distribution along the vertical direction and thus form an effective potential (approximately linear potential) for photons passing through. The light follows more or less the trajectory of a series of parabolas, which is exactly the trajectory of a thrown bouncing ball under gravity.

Based on the similarity described above, using designated effective refractive index distributions to mimic different potentials (external forces), many photonic counterparts of matter wave phenomena have been demonstrated, such as Airy beam [133–136], Wannier-Stark ladder [137], Bloch oscillations [138], dynamic localization [139] and so on. Also due to this similarity, we refer to plasmonic graded index distributions as plasmonic potentials in the following text. The advantage

of doing so is that we can directly apply the well known analysis and results in quantum mechanics to plasmonic waveguides and achieve efficient beam shaping and steering.

3.2 Beam shaping in parabolic plasmonic potentials

In quantum mechanics, the most important model is probably the harmonic oscillator model of a particle in a parabolic potential and this model has been more widely employed in various fields, including atomic and molecular physics, solid state physics and even quantum optics [140–142]. In this section, we borrow this model and investigate different kinds of beam shaping in various parabolic plasmonic potential in quadratically modulated MDM structures, including polychromatic nanofocusing in full parabolic potentials, plasmonic analogue of quantum paddle balls in half parabolic potentials, and adiabatic nanofocusing in tapered parabolic potentials.

3.2.1 Polychromatic nanofocusing in full parabolic plasmonic potentials

In this section, we introduce the concept of polychromatic plasmonics and demonstrate the functionalities of a broadband plasmonic lens based on a metal-dielectric-metal (MDM) structure. We utilize quadratic modulation of the thickness of the dielectric layer in transverse direction to produce a parabolic optical potential which is practically wavelength independent. We develop analytical descriptions and employ numerical simulations to show its capability of three-dimensional subwavelength manipulations, including nanofocusing, self-collimation, and optical pendulum effect. The nanofocusing of our lens is demonstrated over a bandwidth exceeding an optical octave (> 500 nm) thus allowing for polychromatic plasmon focusing.

Background

The field of plasmonics experiences an explosive growth recently due to the ability of plasmonic components to confine light down to the nanoscale. Various plasmonic structures with miniaturization scales comparable to those of modern semiconductor electronics have been designed to realize different types of light waveguiding and control [13, 28, 143–147]. Despite the boom in research one can identify two major challenges for further applications of plasmonic devices: high propagation loss and strong wavelength dispersion. Different approaches to combat optical losses in metals have been explored, including incorporation of gain [44, 148] or nanofocusing [149, 150]. However, the concept of broadband control and nanofocusing of SPPs remains practically unattainable.

The concept of polychromatic light propagation is well developed for dielectric structures, of which the polychromatic dynamic localization is a noticeable

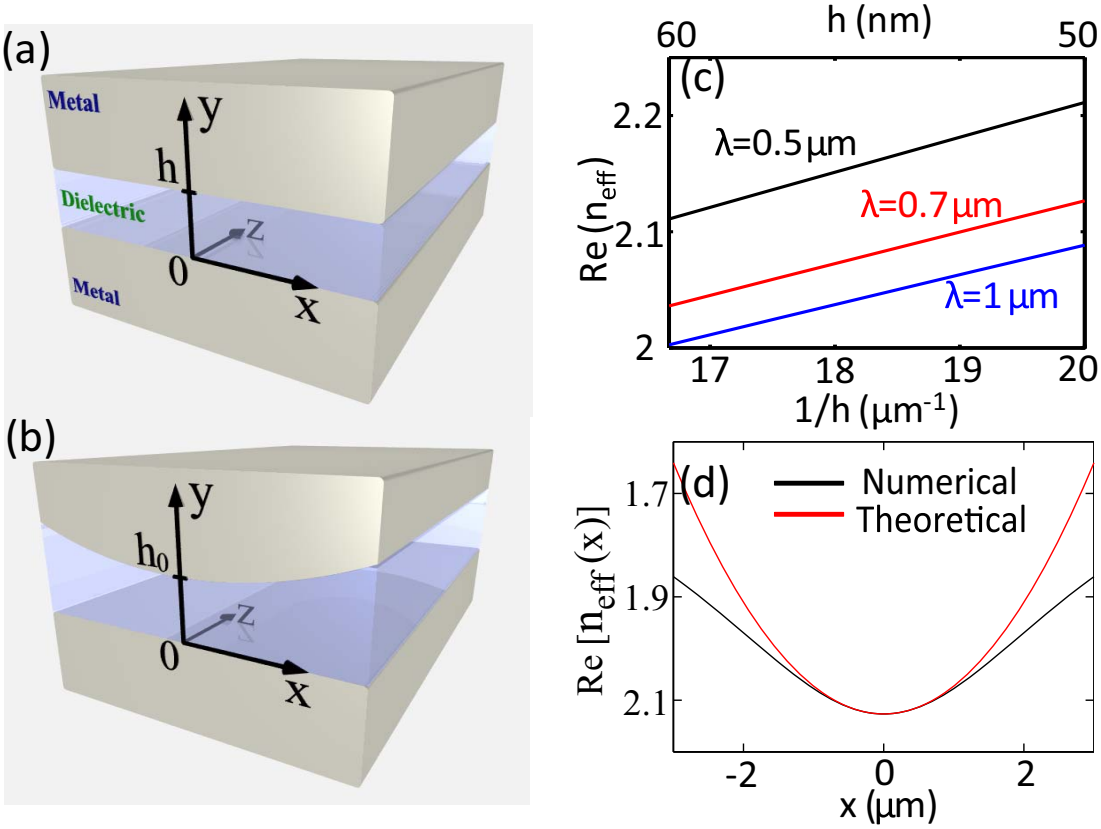

Figure 3.2: (a) Flat and (b) parabolically modulated MDM. (c) Real part of the symmetric mode index of the flat structure *vs.* $1/h$ for various values of free space wavelengths. (d) Real part of the effective permittivity (optical potential) of the structure (b), obtained using Eq. (3.5) (red) and numerically (black).

example [151]. In these structures, curved waveguides are employed to produce an effective wavelength invariant optical potential to compensate for the dispersion. In plasmonics, the engineering of the optical potentials for SPPs has been a key concept for designing plasmonic lenses and other elements [145, 146, 152]. Two kinds of structures with transverse [144, 147] or longitudinally varied effective index [149, 153] are mainly used. In the structures with transverse index modulation the plasmonic potentials are usually heavily wavelength dependent [144–147]. On the other hand, in longitudinally modulated structures light of different wavelengths can be focused asymptotically [153] in the same taper, however light is fully localized there and could not propagate beyond the focus point [149, 153]. Recently a variation of a plasmonic lens was shown to focus broadband light based on diffraction [154]. However, the focusing was obtained for light in free space rather than for propagating SPPs, thus with low focusing resolution. The focusing of polychromatic SPPs still remains an unsolved challenge.

Parabolic potentials in quadratically modulated MDM structures

To address this challenge, first we consider a flat MDM waveguide shown in Fig. 3.2(a). We only consider the symmetric modes of the structure (with respect to the magnetic field distribution) because it is primarily excited by simple end-fire coupling, while the antisymmetric mode experiences a cut-off for the parameters of our work [13]. The dielectric is chosen to be silica glass with permittivity $\epsilon_d = 2.25$, and the metal is silver for which we use the Drude model, $\varepsilon_{\rm m} = 1 - \omega_p^2/(\omega^2 + i\omega\omega_c)$, where ω, ω_p, ω_c are the angular frequency, plasma frequency and collision frequency, respectively. This model is proven to be a good approximation for noble metals, including silver in the spectral range above 500 nm. For silver we take $\omega_p = 1.37 \times 10^{16}$ rad/s and $\omega_c/\omega_p = 0.002$. The effective index of the symmetric mode can be obtained through solving the following equation [10, 13]:

$$\tanh(\frac{1}{2}k_d h) + \frac{\varepsilon_d k_m}{\varepsilon_m k_d} = 0, \tag{3.3}$$

where $k_{m,d} = \sqrt{\tau^2 - \varepsilon_{m,d}}$, $\tau = \frac{2\pi n_{\rm eff}}{\lambda}$ ($\rm n_{eff}$ is the effective refractive index for the symmetric mode and λ is the wavelength in free space). Figure 3.2(c) shows the real part of the effective mode index, versus the inverse thickness of the dielectric for three different wavelengths. The dependence is linear, consistent with the theoretical approximation [155, 156],

$$n_{\rm eff} = a/h + b, \tag{3.4}$$

where both a and b are complex parameters and could be extracted from data fitting. Most importantly, the slope a of these curves is practically *wavelength independent* which allows for the design of broadband optical potential and polychromatic plasmon propagation.

Using the effective refractive index in Eq. (3.4), it is possible to construct a parabolic optical potential [131] for SPPs. This is achieved by a MDM waveguide with one flat and one parabolically curved surfaces as shown in Fig. 3.2(a). The thickness of the dielectric is $h(x) = h_0 + x^2/2R_0$, with R_0 as an effective radius ($R_0 \gg h_0, |x|$).

In this waveguide, we obtain a parabolic optical potential under the condition of $x^2 \ll 2h_0R_0$:

$$n_{\rm eff}(x) = n_0(1 - \frac{1}{2}\Omega^2 x^2), \tag{3.5}$$

where $n_0 = a/h_0 + b$, and $\Omega = \sqrt{a/(n_0 R_0 h_0^2)}$ is the focusing strength. Figure 3.2(d) shows the results calculated by Eq. (3.5) and numerically for $h_0 = 50\,$nm, $\lambda = 0.7\,\mu$m, and $R_0 = 100\,\mu$m.

Expressions for the eigenmodes

Using the effective index method for the structure shown in Fig. 3.2(b), we can express the vertical electric field as [156, 157]:

$$E_y(x, y, z) = A(x)B(x, y)\exp(i\beta z), \tag{3.6}$$

with $B(x,y)$ as the eigenmode field and $A(x)$ as the envelope function. Through substituting Eq. (3.6) into the Helmholtz equation in isotropic media,

$$\nabla^2 E_y + k^2 \varepsilon_{m,d} E_y = 0 \tag{3.7}$$

and neglecting $\partial B(x,y)/\partial x$ and $\partial B^2(x,y)/\partial x^2$ when $R_0 \gg |x|, h_0$, we get the differential equation for $B(x,y)$:

$$\partial^2 B(x,y)/\partial y^2 + \left[k_0^2 \varepsilon - \zeta^2(x)\right] B(x,y) = 0\,, \tag{3.8}$$

where $\zeta(x) = n_{\text{eff}}(x)k$. The expression of $B(x,y)$ is similar to that of E_y in flat metal-dielectric-metal structure, with slight dependence on x [10]:

$$B(x,y) = \gamma \cosh(\vartheta_d y) \tag{3.9}$$

when $0 < y < h(x)$ and

$$B(x,y) = \exp(-\vartheta_m |y - \frac{1}{2}h(x)|) \tag{3.10}$$

when $y < 0$ or $y > h(x)$. In the above two equations Eq.(3.9) and Eq.(3.10), $\gamma = \varepsilon_m \exp[-\frac{1}{2}\vartheta_m h(x)]/\varepsilon_d \cosh[-\frac{1}{2}\vartheta_d h(x)]$, $\vartheta_{m,d} = \sqrt{\zeta^2(x) - k^2\varepsilon_{m,d}}$ and $h(x) = h_0 + x^2/(2R_0)$.

The differential equation for $A(x)$ is [131, 158]

$$\frac{d^2A(x)}{dx^2} + \left[\zeta^2(x) - \beta^2\right] A(x) = 0, \tag{3.11}$$

where $\zeta(x) = kn_{\text{eff}}(x)$ and $\zeta_0 = kn_0$, $k = 2\pi/\lambda$. This is exactly the linear harmonic oscillator equation in quantum mechanics:

$$-\frac{\hbar^2}{2m}\frac{d^2\psi(x)}{dx^2} + (\frac{1}{2}m\omega_0^2 x^2 - E)\psi(x) = 0. \tag{3.12}$$

Based on the well known results of this kind of equation, the eigenmodes of Eq.(3.11) are [131, 158]:

$$A_m(x) = (\sqrt{\pi}\eta_0 2^m m!)^{-\frac{1}{2}} H_m(x/\eta_0) \exp\left(-x^2/2\eta_0^2\right), \tag{3.13}$$

where $\eta_0 = (\zeta_0\Omega)^{-\frac{1}{2}}$ is the characteristic width of the plasmonic waveguide and H_m is the Hermite polynomial. The effective indices of different modes under the paraxial approximation are:

$$n_{\text{eff}}(m) = [\zeta_0 - \frac{1}{2}(2m+1)\Omega]/k. \tag{3.14}$$

We also calculate the eigenmodes of this structure using commercial Mode Solutions (MS) software (Lumerical) with the parameters $x \in [-3,3]\,\mu$m, $y \in [-1,1.05]\,\mu$m, $R_0 = 100\,\mu$m, $h_0 = 50\,$nm and $\lambda = 0.7\,\mu$m. The results of our

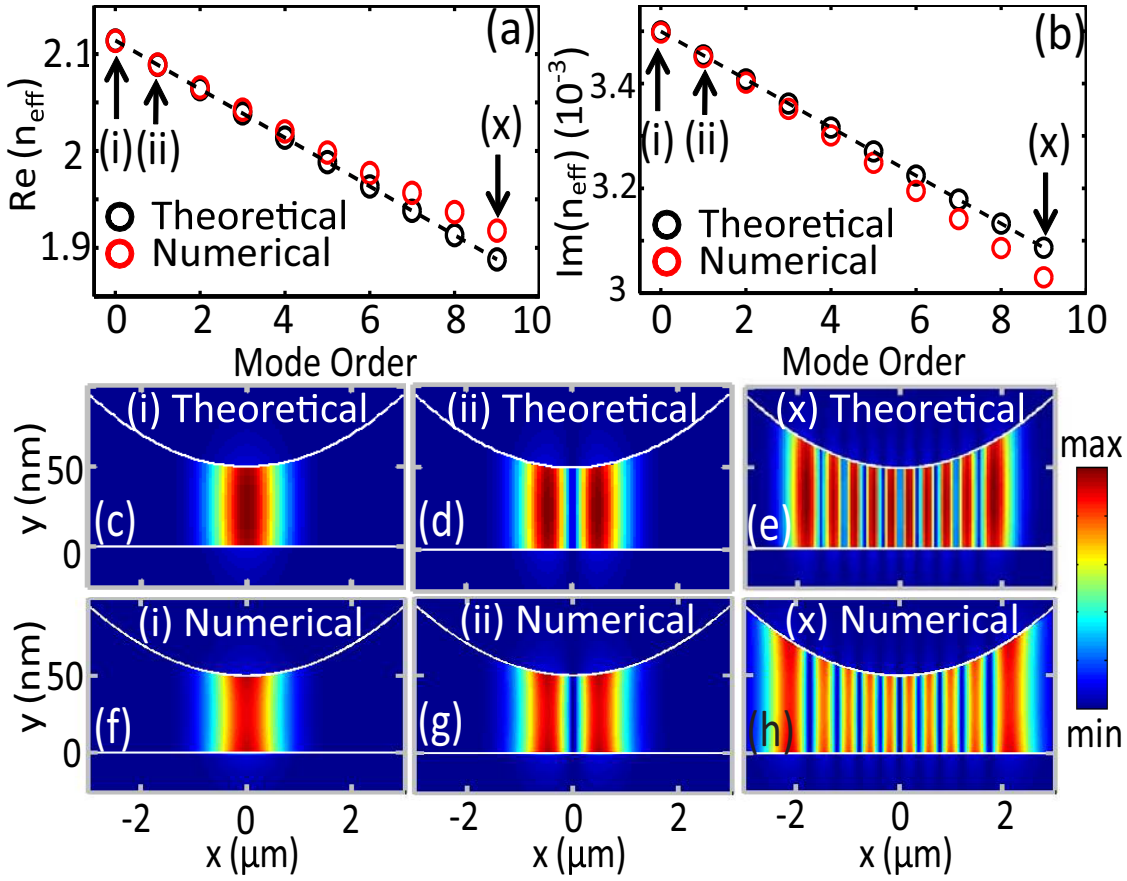

Figure 3.3: (a) Real and (b) imaginary parts of n_{eff} for different order modes. Theoretical (black circles) and numerical (red circles) results are shown. (c-h) Transverse mode profiles of the fundamental, second and tenth order modes. (c-e) Theoretically and (f-h) numerically calculated mode profiles ($|E_y|$).

analytical theory [Eqs. (3.11)-(3.14)] and the MS calculations are summarized in Fig. 3.3. Figure 3.3(a,b) shows the real and imaginary parts of n_{eff} for different modes with the theoretical field distribution of $|A_m(x)B(x,y)|$ [Fig. 3.3(c-e)] and numerically calculated total field $|E_y|$ [Fig. 3.3(f-h)], which show a good agreement for low order modes. For higher order modes, larger discrepancy appears in terms of both effective index and field distribution. This is consistent with the results in Fig. 3.2(d), as the higher order modes spread out to the larger x values, where the assumption $x^2 \ll 2h_0R_0$ does not strictly hold and the potential is not exactly parabolic.

Periodic beam oscillation

Next we study the SPPs propagation in the structure. An incident beam could excite modes of different orders, which will then interfere with one another, producing different intensity patterns inside the structure. As a result of this interference, a range of SPPs beam manipulations is possible, including focusing, self-collimation,

and optical pendulum effect [131, 158].

For an incident beam $C(x, y, 0)$, we can expand it into a complete set of orthogonal modes:

$$C(x, y, z) = \sum_{m=0}^{\infty} \chi_m A_m(x) B(x, y) \exp(i\beta_m z), \tag{3.15}$$

where $\chi_m = \langle A_m(x)B(x, y)\,,\ C(x, y, 0)\rangle$. The inner product is defined as:

$$\langle \psi_1\,,\ \psi_2\rangle = \iint \psi_1^* \psi_2 \, dxdy \tag{3.16}$$

When $C(x, y, 0) = C(x, 0)C_2(y, 0)$, $A(x)$ could be decoupled from $B(x, y)$, and $B(x, y)$ changes slowly with x, we get:

$$\chi_m = \int B(x, y)^* C_2(y, 0) dy \int A_m(x)^* C(x, 0) dx. \tag{3.17}$$

This means that the beam expansions along x and y are independent. Considering that the beam distribution along y could be fully characterized by $B(x, y)$, we check only the beam dynamics in the $x - z$ plane [158]:

$$C(x, z) = \sum\nolimits_{m=0}^{\infty} a_m A_m(x) \exp(i\beta_m z), \tag{3.18}$$

where a_m is the expansion coefficient of the m-order mode $a_m = \int A_m(x)^* C(x, 0) dx$. If the initial beam has a Gaussian distribution:

$$C(x, 0) = \pi^{-\frac{1}{4}} w_0^{-\frac{1}{2}} \exp[-(x - x_0)^2/2w_0^2], \tag{3.19}$$

where w_0 is the beam width, then the expansion coefficient is [131, 158]:

$$a_m = \frac{\sqrt{\pi}}{2^{m/2}\sqrt{m!}} \frac{\sqrt{2} w_0 \xi_0}{\sqrt{\xi_0^2 + w_0^2}} \left(\frac{\xi_0^2 - w_0^2}{\xi_0^2 + w_0^2}\right)^{m/2} H_m\left(\frac{w_0 x_0}{\sqrt{\xi_0^4 - w_0^4}}\right) \exp[-\frac{1}{2} x_0^2/(\xi_0^2 + w_0^2)]. \tag{3.20}$$

and the beam inside the structure, under paraxial approximation, is [131, 158]:

$$C(x, z) = \frac{1}{\sqrt[4]{\pi q^2(z)}} \exp\left\{-\frac{[x - x_0\cos(\Omega z)]^2}{2\eta^2}\right\} \times \exp\left[i(k_0 z + \tfrac{1}{2} k_0 \rho^{-1} x^2)\right] P(x_0), \tag{3.21}$$

where $\eta^2 = |q(z)|^2$, $\rho^{-1} = \eta^{-1} d\eta/dz$, $P(x_0) = \exp\{i(\eta_0/w_0)^2[x x_0 \sin(\Omega z) - \frac{1}{4} x_0^2 \sin(2\Omega z)]\}$ and $q(z) = w_0 \cos(\Omega_z) + i(\eta_0^2/w_0)\sin(\Omega z)$. In the lossless case with $\omega_c = 0$, the beam amplitude can be expressed as:

$$|C(x, z)| = \pi^{-\frac{1}{4}} \eta^{-\frac{1}{2}} \exp\left\{-\left[x - x_0\cos(\Omega z)\right]^2 / 2\eta^2(z)\right\} \tag{3.22}$$

and the dynamic beam width varies along propagation:

$$\eta(z) = \sqrt{w_0^2 \cos^2(\Omega z) + \eta_0^4/w_0^2 \sin^2(\Omega z)}\ . \tag{3.23}$$

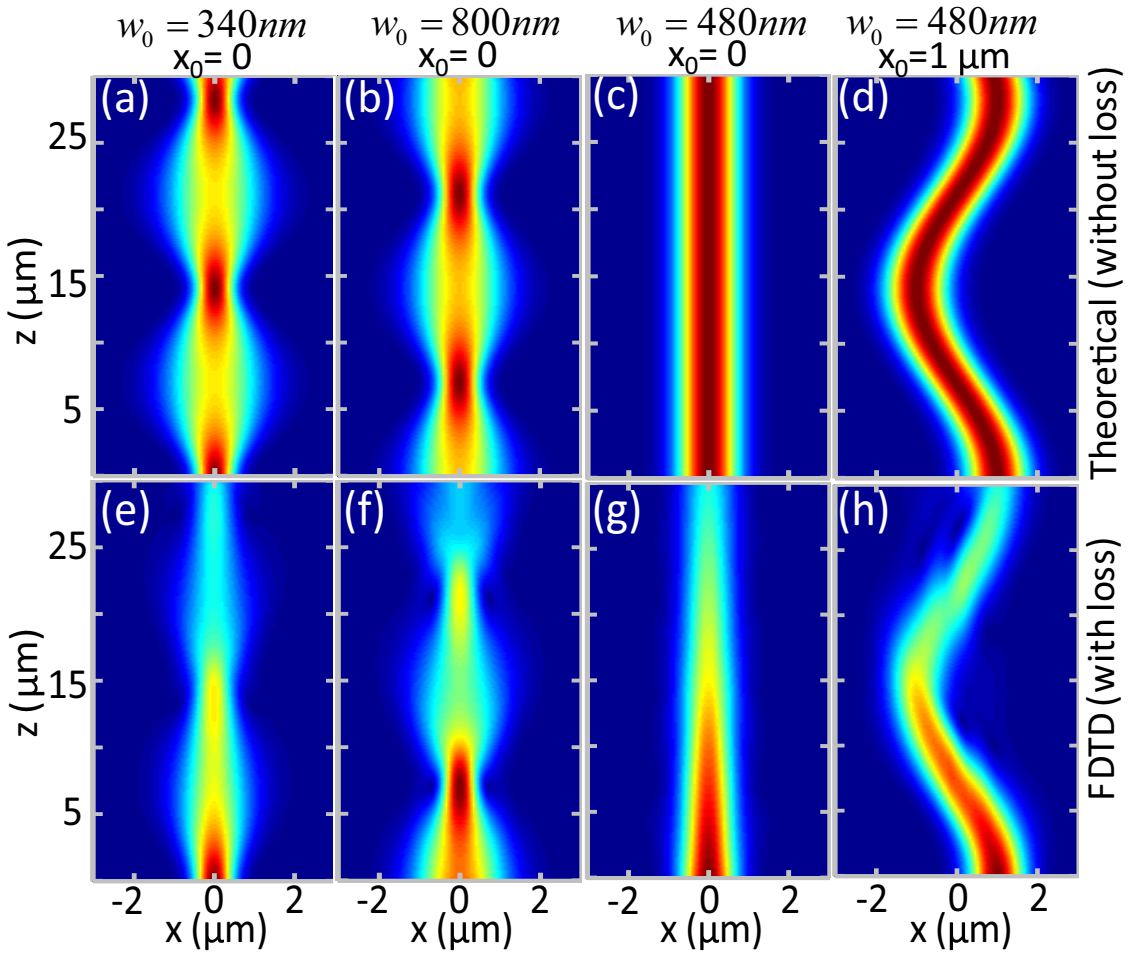

Figure 3.4: (a-d) Theoretical field distribution without loss and (e-h) FDTD simulations with loss (shown $|E|$) in the $x-z$ plane in the middle of the gap ($y = h_0/2 = 25\,\text{nm}$). Plots (a, b, e, f) show typical effects of self-imaging with nanofocusing; (c, g) self-collimation; and (d, h) optical pendulum effect. The corresponding characteristic beam width is $\eta_0 \approx 480\,\text{nm}$.

The plasmon polariton beam is thus oscillating periodically along z. It is easy to prove that the maximum and minimum dynamic beam widths are constrained by [131] $\eta_{\max}\eta_{\min} = \eta_0^2$, indicating that the beam is trapped in the parabolic optical potential.

To confirm our theoretical analysis, we preform finite-difference-time domain (FDTD) simulations (Lumerical). All initial beams are y-polarized with transverse Gaussian distributions to guarantee the excitation of SPPs modes, as the plasmonic waves are TM polarized. The structure parameters are the same as in the MS simulation, with $z \in [0, 30]\,\mu$m and $x \in [-3, 3]\,\mu$m, $y \in [-1, 1.05]\,\mu$m. Also we place perfectly matched layers at the boundaries and field distribution monitors within the gap in the $x-z$ plane. To model the fine features of this structure especially the metal dielectric interface along y, we make the minimum mesh size along y as 0.5nm and 25nm along x and z. We have also tried finer meshes to make sure that

the simulation results are convergent. The analytical results without loss and the numerical results with loss are presented in Fig. 3.4. The data are shown for the $x-z$ plane in the middle of the gap, $y = h_0/2 = 25\,\text{nm}$.

For an on-axis input beam ($x_0 = 0$) [Fig. 3.4(a, b, e, f)], one can observe periodic beam focusing with a period of

$$F = \pi/\Omega = \pi\sqrt{R_0 h_0(1 + h_0 b/a)}\,. \tag{3.24}$$

The points of maximum intensity correspond to the focusing when all excited modes interfere constructively. There is an initial phase shift depending on the ratio of the incident beam width and the characteristic width of the plasmonic waveguide w_0/η_0. When these two widths match $w_0 = \eta_0$, one can observe self-collimation effect - diffractionless propagation of the beam [see Fig. 3.4(c, g)]. For an off-axis input beam ($x_0 \neq 0$) there are transverse oscillations [see Fig. 3.4(d, h)], and the plasmon polariton beam propagation exhibits an analog of optical pendulum behavior in a parabolic potential. The comparison with FDTD results suggests that losses do not affect the beam propagation except for attenuation along z direction.

Polychromatic nanofocusing of the plasmonic waves

Equation (3.24) has some important implications for propagation of polychromatic SPPs beams. As a is practically wavelength independent while b varies slowly [Fig. 3.2(c)], the focusing strengths Ω and the oscillation period F are nearly the same for different wavelengths. For example, in Fig. 3.5(a) we show both the theoretical (solid line) and FDTD (circles) results for an input beam with $w_0 = 800\,\text{nm} > \eta_0$ for three different thicknesses h_0 in the wide wavelength range $0.5 - 1.0\,\mu\text{m}$. The different color beams focus at the planes of $z = F_1 = F/2$. The dispersionless characteristic of F enables broadband SPPs focusing and distinguishes our plasmonic structure from other highly wavelength dependent structures [144, 147]. In Fig. 3.5(b-d) we show the field distribution $|E|$ on the $x-z$ plane of $y = h_0/2 = 15\,\text{nm}$ for the three points marked in Fig. 3.5(a) at $h_0 = 30\,\text{nm}$. False colors are used to indicate schematically the three different wavelengths. It is important to note that the focal planes of all spectral components coincide within 500 nm (less than one wavelength deviation in the spectral range $0.5 - 1.0\,\mu\text{m}$) and are practically indistinguishable. Note that the focal depth is in the range of $2-3\,\mu\text{m}$ for the different spectral components. Figure 3.5 proves that this structure acts as a lens for broadband polychromatic light focusing, a functionality that has not been discussed in other plasmonic structures. From Fig. 3.5 and Eq. (3.24), it is clear that one can control the position of the focusing points by varying the thicknesses h_0 and/or the wire curvature R_0, which enables wide reconfigurability of our structure.

Focusing resolution of the plasmonic waves

Finally, we investigate the focusing resolution of this structure, which is characterized by the full width at half maximum (FWHM) along x direction at the focal

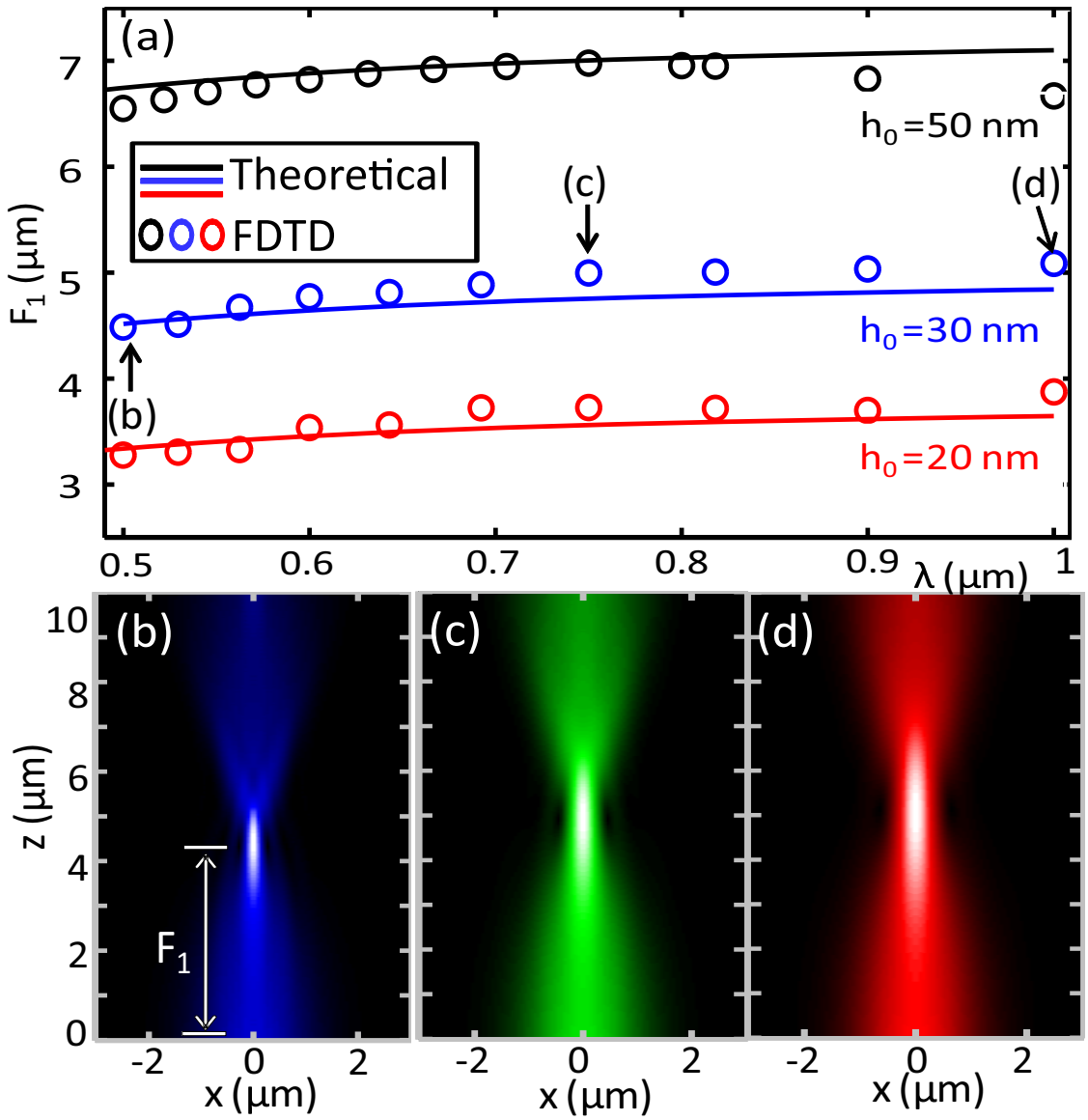

Figure 3.5: (a) Focusing position $z = F_1$ for wavelengths in the range $0.5 - 1.0\,\mu$m at h_0 values of 20 nm, 30 nm and 50 nm. Solid lines: theoretical results; circles: FDTD simulations. (b-d) SPPs propagation for the three wavelengths marked in (a).

plane. (Along the vertical direction the resolution can be approximately characterized by the thickness of the dielectric layer as shown in the insets of Fig. 3.6.) We define the wavelength of the SPPs, $\lambda_{\text{spp}} = \lambda/n_{\text{eff}}$, which is smaller than the light wavelength in the dielectric, $\lambda_p = \lambda/n_d$. What makes SPPs special is that its wavelength could be made as small as required, even vanishing for localized surface plasmons [13]. In our lens-like structure, if we want to improve the focusing resolution, we could decrease λ_{spp}. For a fixed vacuum wavelength, the simplest approach to increase n_{eff} is to make the thickness h_0 smaller. Figure 3.6 shows the dependency of FWHM along x at the focal plane for a fixed wavelength $\lambda = 0.7\,\mu$m and $w_0 = 800$ nm. Figure 3.6(a, b) shows the field distribution $|E|$ along propagation

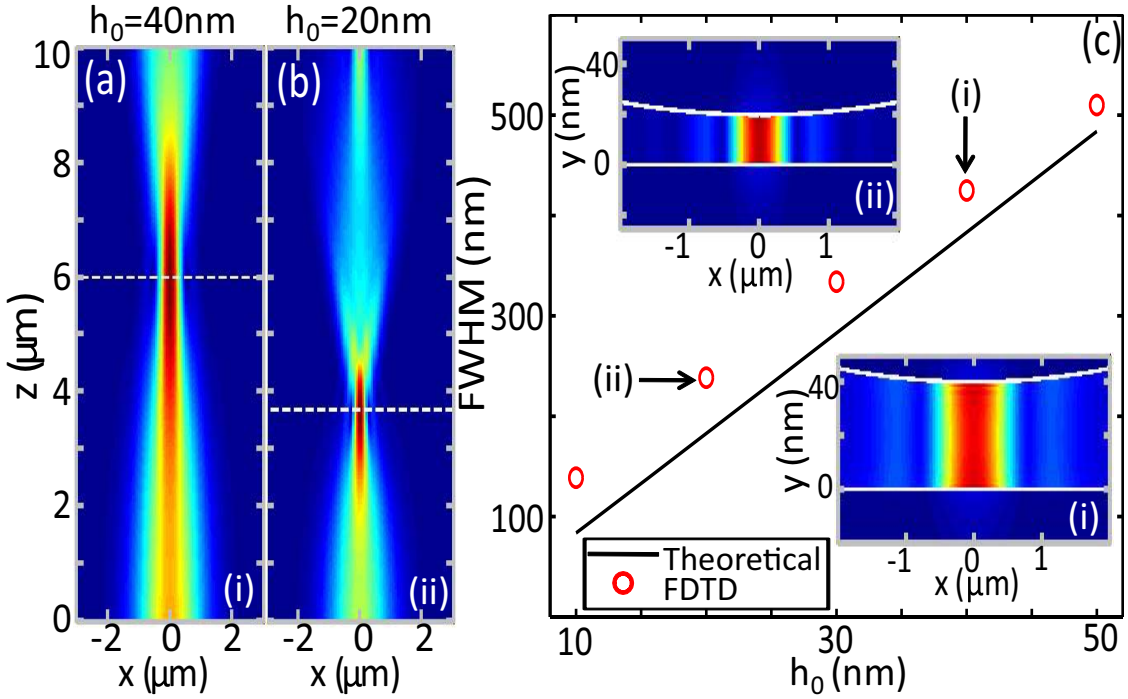

Figure 3.6: (a,b) FDTD results for the field distribution, $|E|$, in the $x-z$ plane $y = h_0/2$ ($h = 40\,\text{nm}$ and $20\,\text{nm}$) and $\lambda = 0.7\,\mu\text{m}$. White dashed lines indicate the focal plane. (c) FWHM in the focal plane *vs.* h_0. Marked points correspond to the cases (a) and (b), respectively. Insets: transverse field distributions $|E|$ in the two marked focal planes.

for the two points marked in Fig. 3.6(c) in the $x-z$ plane of $y = h_0/2$ (20 nm and 10 nm, respectively). The white dashed lines indicate the focal planes. Insets (i) and (ii) show the transverse field distribution of $|E|$ at the two focusing planes. As shown in Fig. 3.6, the FWHM could be as small as 100 nm. This could be further improved by decreasing R_0 and/or increasing the focusing strength Ω. Our results clearly show that the light is fully confined in the dielectric along y and trapped in the optical parabolic potential along x.

Conclusion

In conclusion, we have suggested the concept of polychromatic plasmonics and demonstrated a broadband plasmonic lens based on a parabolically modulated MDM structure. We have shown the plasmonic lens allows for complete three-dimensional subwavelength control of a beam, bringing a potential functionality for manipulation of ultra-short optical signals. The focusing capability of this plasmonic lens could be further improved by tapering the dielectric layer along the propagation direction [159]. We anticipate the proposed structure is a promising candidate for broadband plasmonic applications including subwavelength white light imaging, polychromatic plasmon solitons, and ultrashort pulse plasmonic nanolasers. Furthermore, our ideas can be extended beyond the field of plasmonics, to include quan-

tum particles in parabolic potentials, considering the similarity between Shrödinger equation and paraxial wave equation.

3.2.2 Plasmonic analogue of quantum paddle balls in half parabolic plasmonic potentials

In this section, we suggest a plasmonic analogue of the quantum paddle ball by employing a half parabolic potential with a fully repulsive wall (paddle ball potential). The potential is obtained in a MDM structure with a quadratically modulated dielectric layer and a metallic reflecting wall on one side. Employing such a potential, we demonstrate both analytically and numerically, the wave revivals, oscillations, and interference patterns (in the region close to the reflecting surface) of the plasmonic beam. Furthermore, as the proposed plasmonic quadratic potentials are effectively non-dispersive, the plasmonic paddle ball can be achieved with broad bandwidth polychromatic light, thus finding possible applications in subwavelength beam steering and manipulations for ultra-short laser pulses.

Background

In recent years optics has offered remarkable opportunities to test wave phenomena in various physical systems, including solid state, relativistic and non-relativistic quantum physics [160]. This is due to the ability to directly visualize the wavefunction of light beams as well as to build up with unprecedented accuracy the optical potentials, thus engineering the dispersion of waves in the system. Important examples constitute the optical demonstration of Bloch oscillations, dynamic localization, relativistic trembling motion of a free Dirac electron, and quantum bouncing ball [160–162]. The latter originates from the implementation of a half-linear potential model [141], finding its counterparts in cold atoms [163] and neutron physics [164, 165]. The linear potentials however are anharmonic, leading to fractional revivals, phase collapses and aperiodic oscillations of the bouncing ball [141, 162].

Therefore the fundamental harmonic oscillator model of a particle in a parabolic potential has been more widely employed in various fields, including atomic and molecular physics, solid state physics and quantum optics [140–142]. The related half parabolic potential model, corresponding to a harmonic oscillator with a rigid wall, was also proposed and investigated in terms of a *quantum paddle ball* [140, 141]. In a sharp contrast to the anharmonic bouncing balls, paddle balls experience full wave revivals and periodic beam oscillations with no phase collapses [141]. Also due to its simplicity and harmonicity, the quantum paddle ball can serve as a basic model to explain the full wave dynamics of matter waves scattered by high potential barriers [141, 166], to investigate atomic wave diffraction and interference [166, 167], to study the van der Waals force between atom and barrier [168], and to investigate chaotic quantum bouncers [169]. So the direct optical visualization of the wave-dynamics of paddle balls is an attractive milestone, however never studied before.

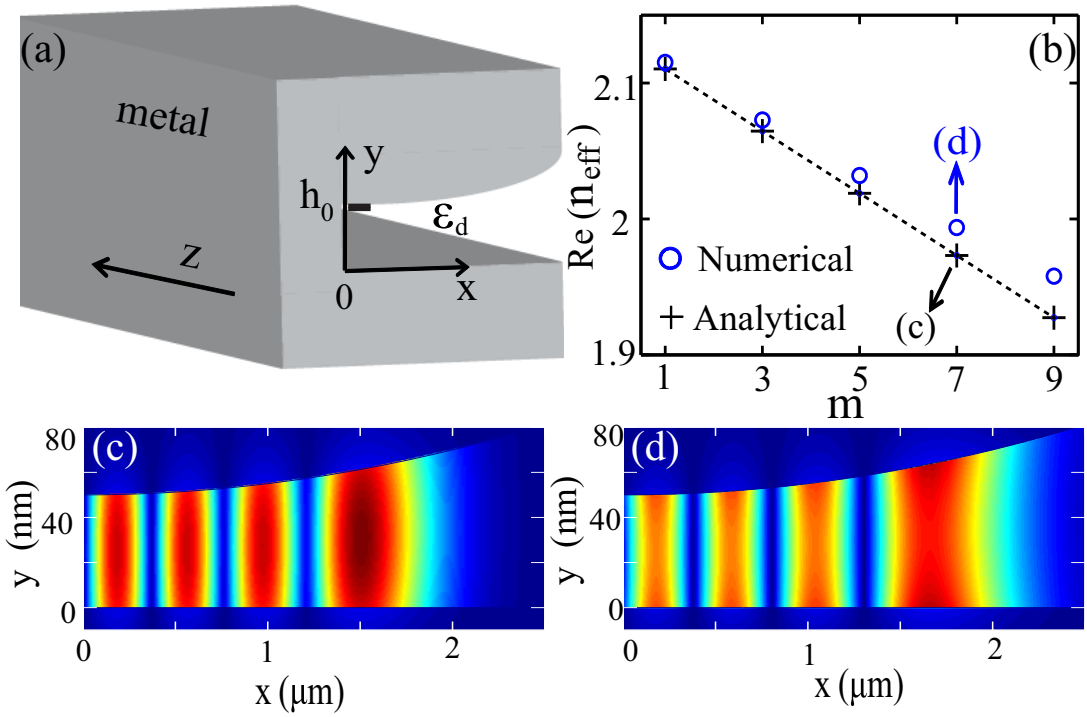

Figure 3.7: (a) Quadratically modulated MDM structure with a side reflecting metal wall. (b) Real part of the effective refractive index of the modes supported by the structure shown in (a). Both analytical [Eq. (3.26)] and numerical (mode solver, Lumerical) results are shown. The field distribution of the mode $m = 7$ is shown in (c) (analytical, $|B_m(x, y)|$) and (d) (numerical, $|E_y|$). The metal is silver, which is described by the Drude model and other parameters are $h_0 = 50\,\text{nm}$, $\lambda = 0.633\,\mu\text{m}$, $R_0 = 100\,\mu\text{m}$ and $\varepsilon_d = 2.25$.

The implementation of a plasmonic potential rather than dielectric optical potential carries a number of advantages to our work. The field of plasmonics not only offers a chance to confine light down to the nanoscale [28], but also provides a novel tool to visualize the wave effects which are not easy to realize in photonics [170]. This is because in plasmonics one can construct photonic potentials with large absolute values of amplitude and gradient, which are elusive in dielectric structures [156, 170].

Eigenmodes in half parabolic potentials

In the modulated MDM structure shown in Fig. 3.7(a) (the thickness of the dielectric layer is $h(x) = h_0 + x^2/(2R_0)$ for $x \geq 0$, with a pure metal wall for $x < 0$), we obtain a plasmonic paddle ball potential (half parabolic potential) under the condition of $x^2 \ll 2h_0R_0$:

$$n(x) \approx \begin{cases} \infty & (x < 0) \\ n_0\,(1 - \Omega^2 x^2/2) & (x \geq 0) \end{cases}, \tag{3.25}$$

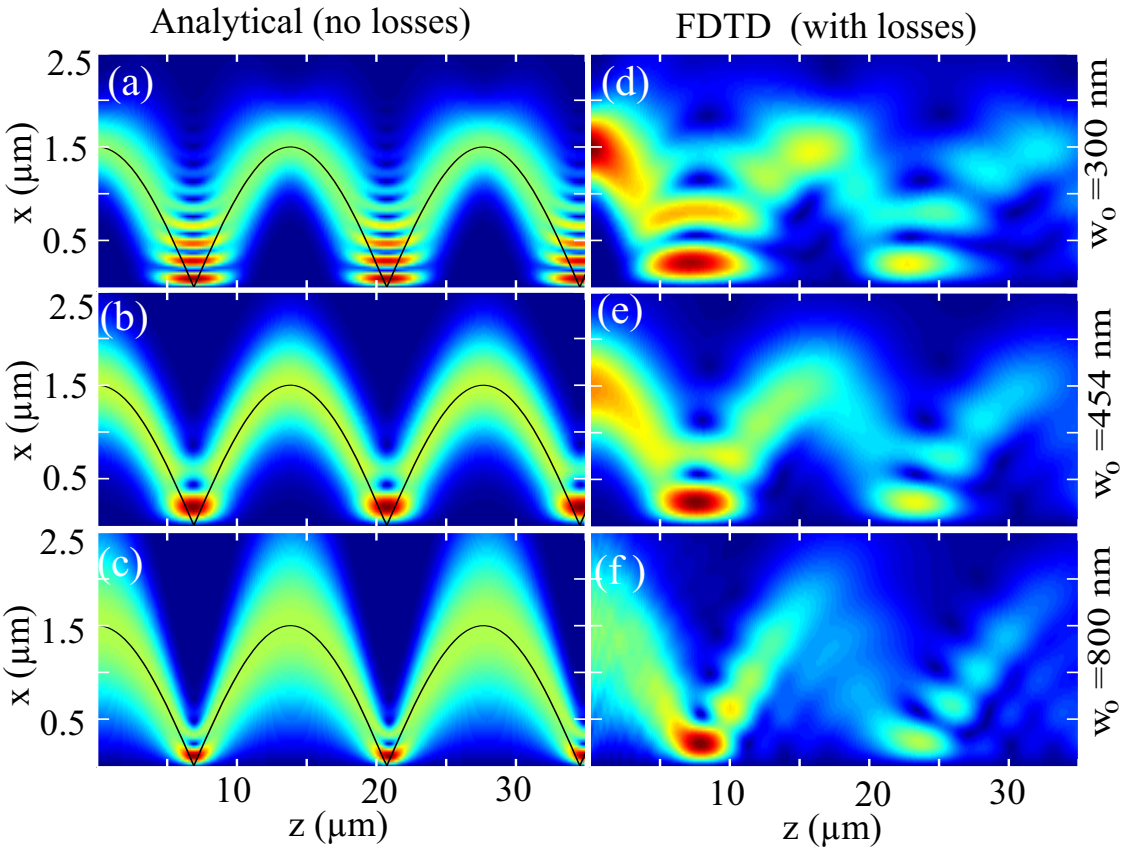

Figure 3.8: (a-c) Analytical results [Eq. (3.29)] for the beam propagation with three input widths: $w_0 = 300$ nm, 454 nm, and 800 nm. Black curves represent the classical trajectories of the beams calculated from Hamiltonian optics. (d-f) Numerical FDTD results ($|E|$) in the plane $y = h_0/2 = 25$ nm. Parameters are the same as in Fig. 3.7.

where $n_0 = a/h_0 + b$, and $\Omega = \sqrt{a/(n_0 R_0 h_0^2)}$ is the potential strength. It is worth noticing that in Eq. (3.25) we neglect the field penetration into the left metal wall on the side and the consequent effects, such as phase modification, Goos-Hänchen shift and bulk mode excitations [171]. The eigenvalues (termed as effective refractive index in the realm of optics) and corresponding eigenmodes of this paddle ball potential can be easily obtained from its counterpart of complete parabolic potential $n(x) = n_0(1 - \frac{1}{2}\Omega^2 x^2)[x \in (-\infty, +\infty)]$: only modes with odd parities of the full potentials can exist in the corresponding paddle ball potentials, with exactly the same effective refractive index. Those half modes actually provide a complete orthogonal set for the paddle ball potentials [141]. The eigenvalues of the paddle ball potential of the structure in Fig. 3.7(a) are [corresponding to effective refractive index of odd modes in the full parabolic potential in Eq. (3.14)]:

$$n_{\text{eff}}(m) = n_0 - \Omega(m + 1/2)/k \quad (m = 1, 3, 5...), \tag{3.26}$$

where $k = 2\pi/\lambda$ is the wavenumber in vacuum and the field distributions of the corresponding eigenmodes are: $B_m(x, y) = A_m(x, y)$ $(x \geq 0)$; $B_m(x, y) = 0$ $(x < 0)$, where $A_g(x, y)$ $(g = 0, 1, 2...)$ denotes the eigenmodes of the full potential counter-

part in Section 3.2.1. In Fig. 3.7(b) we show the real parts of the effective refractive index and the field distributions of the eigenmodes supported in the structure shown in Fig. 3.7(a). Both analytical [Eq. (3.26)] and numerical (Mode solver, Lumerical) results are shown. The dielectric layer between the metal plates is glass with $\varepsilon_d = 2.25$ and the metal is silver, for which we use the Drude model with the same parameters as in Section 3.2.1. Other parameters for Figs. 3.7(b)-(d) are $h_0 = 50\,\mathrm{nm}$, $\lambda = 0.633\,\mu\mathrm{m}$, and $R_0 = 100\,\mu\mathrm{m}$. Both analytical and numerical results agree very well, except for higher-order modes. This is because higher-order modes spread out more to the larger x region [as shown in Figs. 3.7(c-d)], where the approximation $x^2 \ll 2h_0R_0$ does not fully hold, and consequently the potential deviates from being exactly parabolic.

Bouncing plasmonic waves in half parabolic potentials

As the next step, we investigate analytically the beam evolution in the plasmonic potential. Similar to the full parabolic potential case the propagation of any incident beam $F(x, y, 0)$ could be expanded into the eigenmodes of this paddle ball potential:

$$F(x, y, z) = \sum\nolimits_m \beta_m B_m(x, y) \exp[ikxn_{\mathrm{eff}}(m)], \tag{3.27}$$

where $\beta_m = \iint F(x, y, 0)B_m^*(x, y, 0)dxdy$ are the expansion coefficients. Meanwhile, considering the special boundary condition in the model the expansion could also be expressed as [141, 172]:

$$F(x, y, z) = \begin{cases} 0 & (x < 0) \\ \psi(x, y, z) - \psi(-x, y, z) & (x \geq 0) \end{cases}. \tag{3.28}$$

Here $\psi(x, y, z) = \sum_g \alpha_g B_n(x, y) \exp[ikxn_{\mathrm{eff}}(g)]$ and $\alpha_g = \iint F(x, y, 0)A_g^*(x, y, 0)dxdy$ is the corresponding expansion coefficient (expanded into the eigenmodes of the full potential). If the initial beam has a Gaussian distribution along x: $F(x, 0) = \pi^{-\frac{1}{4}} w_0^{-\frac{1}{2}} \exp[-(x - x_0)^2/2w_0^2]$, where w_0 characterizes the initial beam width and x_0 is the beam center offset, the beam in the $x - z$ domain is [141, 172] (under paraxial approximation and ignoring the metallic loss of the plasmonic potential):

$$|F(x, y, z)| = (\tfrac{2}{\xi(z)\sqrt{\pi}})^{1/2} \exp\left\{-\tfrac{1}{2}\tfrac{x^2 + x_0^2\cos^2(\Omega z)}{\xi^2(z)}\right\} |P(x) - P(-x)|, \tag{3.29}$$

where $P(x) = \exp[xx_0\cos(\Omega z)/\xi^2(z) + ixx_0\sin(\Omega z)/w_0^2]$ and the dynamic beam width is:

$$\xi(z) = \sqrt{w_0^2\cos^2(\Omega z) + \eta_0^4/w_0^2\sin^2(\Omega z)}, \tag{3.30}$$

with $\eta_0 = (n_0 k\Omega)^{-1/2}$ as the characteristic potential width. The beam experiences periodic oscillations with the period of $L = 2\pi/\Omega$.

The dynamic beam width is constrained by the potential:

$$\xi_{\max}\xi_{\min} = \eta_0^2, \tag{3.31}$$

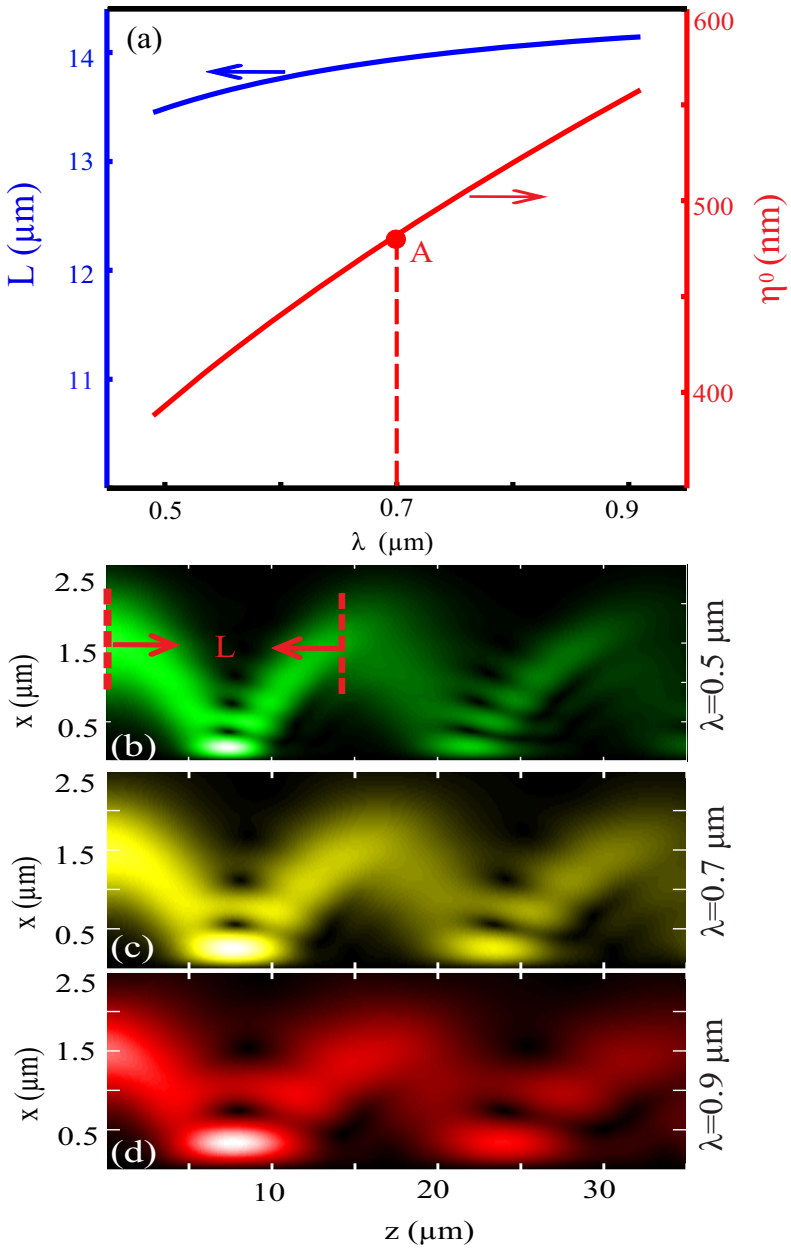

Figure 3.9: (a) Characteristic potential width η_0 and oscillation period L for the wavelength range of $0.5 - 0.9$ μm. (b)-(d) FDTD results ($|E|$) for beam propagation in the plane $y = h_0/2 = 25$ nm for three wavelengths of $\lambda = 0.5$ μm, 0.7 μm and 0.9 μm. For all the three cases, w_0 is fixed at 482 nm, which is the characteristic potential width of $\lambda = 0.7$ μm, as indicated by point A in (a). Except for the wavelength, other parameters are the same as in Fig. 3.7.

and the beam width is a constant $\xi(z) = w_0$ only if the initial beam width is $w_0 = \eta_0$. When the beam hits the wall, the beam width is:

$$\xi_w = \xi(\Omega z = \pi/2) = \eta_0^2/w_0, \tag{3.32}$$

which is inversely proportional to w_0. In Figs. 3.8(a-c) we show the analytical results

of Eq. (3.29) with three initial beam widths: $w_0 = 300$ nm, 454 nm and 800 nm when $\lambda = 0.633\,\mu$m. The parameters are the same as in Fig. 3.7 and correspondingly $\eta_0 =$ 454 nm. The classical trajectories, calculated through Hamiltonian optics [173], are shown by black curves.

Plasmonic paddle balls shown in Figs. 3.8(a-c) experience full beam revivals and periodic beam oscillations. This is due to the harmonic nature of the paddle ball potentials, in other words, the symmetry of the Hamiltonian in phase space and thus the equidistant energy levels (or equidistant effective refractive index of eigenmodes in optics) [141, 174]. Meanwhile, similar to photonic bouncing balls, plasmonic paddle ball shows significant interference patterns in the region close to the walls, which come from the interference of the incoming and reflecting beams. It is worth mentioning that smaller w_0 would lead to larger dynamic beam width ξ_w [Eq. (3.32)] and thus larger overlapping region of the incoming and reflecting beams, resulting in larger interference regions [Figs. 3.8(a-c)].

In Figs. 3.8(d-f) we show correspondingly the FDTD results for $|E|$ on the plane $y = h_0/2 = 25$ nm (Lumerical), with the Ohmic losses of metal included. The discrepancies between the analytical and the numerical results come from both metallic losses and the paddle ball potential approximation [Eq. (3.25)].

Finally, we study the dispersion of the plasmonic paddle ball potentials. The period of the beam oscillations L depends on the potential strength Ω. As Ω is practically wavelength independent, we expect multi-color plasmonic paddle balls with the same oscillating period: polychromatic plasmonic paddle balls. In Fig. 3.9(a) we show both the characteristic potential width η_0 and oscillation period L for the wavelength range of $0.5 - 0.9$ μm. Other parameters are the same as in Fig. 3.7. It is obvious that for this wavelength range of more than an optical octave, L is almost the same and the aberration is within 1 μm.

Then we show the beam distributions on the plane $y = h_0/2 = 25$ nm for three wavelengths of $\lambda = 0.5$ μm, 0.7 μm and 0.9 μm in Figs. 3.9(b-d) respectively (FDTD, $|E|$). The initial beam width w_0 is fixed at 482 nm, which is the characteristic potential width for $\lambda = 0.7$ μm [point A in Fig. 3.9(a)]. It is seen that the plasmonic analogue of a paddle ball of different colors exhibits almost dispersionless oscillation period, justifying the claim of polychromatic behavior of the plasmonic analogue of a paddle ball. Meanwhile η_0 is of significant differences for beams of different wavelengths [Fig. 3.9(a)]. This means that with fixed w_0, the dynamic beam width ξ_w changes with wavelength [Eq. (3.32)], leading to different interference scopes for light of different wavelengths.

Conclusion

In conclusion, we have introduced a plasmonic analogue of a quantum paddle ball through employing a quadratically modulated metal-dielectric-metal structure with a reflecting wall on the side. We have described beam revivals, periodic beam oscillations, and significant interference patterns close to the wall, which resemble the full wave dynamics of the corresponding propagating matter waves. We have also demonstrated that the plasmonic paddle ball operates in a polychromatic

regime, which may find applications in broadband subwavelength beam manipulations, polychromatic plasmon focusing, and ultrashort pulse plasmonic nanolasers.

The structure proposed in this section is quite practical considering that it corresponds to a broad metal wire (with diameter of several hundred microns) above a metal plate with another reflecting metal wall on the side. Also when reflecting walls are introduced at the potential bottom, the plasmonic paddle ball potential could be realized in air-polymer-metal structures, which could be characterized directly by fluorescence imaging or leakage radiation microscopy [170, 175]. It is worth mentioning that paddle ball potential is not confined to the field of plasmonics and could be easily extended to other branches of nanophotonics and graded index structures.

3.2.3 Adiabatic nanofocusing in tapered parabolic plasmonic potentials

In this section we propose and investigate the adiabatic nanofocusing of the fundamental modes in plasmonic parabolic potentials. The potentials are obtained in the MDM structure, of which the dielectric layer width is modulated quadratically in the horizontal direction and linearly in the longitudinal direction. In such a structure, light is compressed in both transverse directions due to increasingly stronger parabolic potentials and decreasing dielectric layer width. We show by both closed from analytical descriptions and by simulations that there is a critical tapering angle, above which the field could be enhanced. In contrast to previously reported tapered structures in the adiabatic regime without transverse potentials, the structure proposed in this section shows stronger focusing capability and allows monotonic increasing field enhancement over longer propagation distances.

Background

SPPs are highly lossy due to the intrinsic Ohmic loss of metal and this poses a great challenge for its further applications, which requires significant field enhancement. To address this challenge, various structures are proposed and experimentally verified for nanofocusing of SPPs (see Refs. [149, 177–179] and references therein). Among all the structures proposed, tapered MDM slot waveguides have attracted large attention due to the fabrication simplicity, high coupling efficiency and strong focusing effects [37, 150, 159, 178–183]. In two dimensional MDM structures shown in Refs. [180–182], although significant field enhancement can be achieved, for realistic beams carrying finite energy, light is confined in only one transverse direction within the dielectric layer but would diffract in the other direction, thus rendering the nanofocusing incomplete.

Different approaches have been employed to compress light in the other transverse direction, including decreasing the transverse dimensions [176, 183] [shown in Fig. 3.10(a)], introducing a extra potential by transverse modulation [159] [shown Fig. 3.10(b)] or through incorporating materials with nonlinearities [150] [shown in Fig. 3.10(c)]. However, all those approaches have specific problems. For structures truncated finite in the transverse direction as shown in Refs. [176, 183], as the field

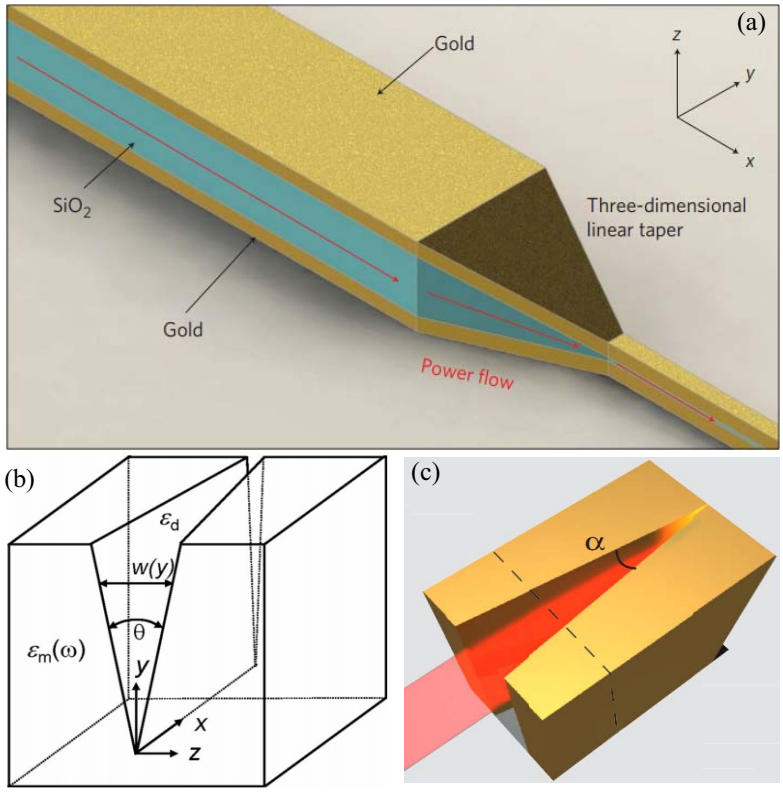

Figure 3.10: Different approaches for efficient plasmonic wave nanofocusing based on: (a) shrinking directly the transverse dimension, (b) constructing effective Coulomb potentials and (c) introducing nonlinearities in the focusing structure. From Refs. [150, 159, 176].

is still strong in the region close to the edge, the edge effects would be strong and SPPs confined would be too sensitive to the edge roughness and other surrounding perturbations. For the structure shown in Ref. [159] where a Coulomb potential is introduced, light is fully localized within the edge when the opening angle is smaller than the critical angle and thus this structure is hard to be applied for applications in visible light regime (the critical angle of visible light is large and this will set a limit for the opening angle and hence significantly suppress the nanofocusing effects). Moreover, the Coulomb potential is asymmetric and the coupling efficiency would be low if the incident beam is symmetric. Although introducing nonlinearities [150] would avoid problems mentioned above, the nanofocusing would be undermined by the nonlinear saturation [94] and also nonlinearity based devises would be highly intensity sensitive, which is not desirable for on-chip signal processing.

Expressions for field evolutions in tapered parabolic potentials

In this section we introduce symmetric plasmonic parabolic potentials to confine light in one of the transverse directions. In the MDM structure shown in Fig. 3.11(a), the dielectric layer width is modulated quadratically in the horizontal direction to produce a parabolic potential and tapered linearly in the longitudinal direction with

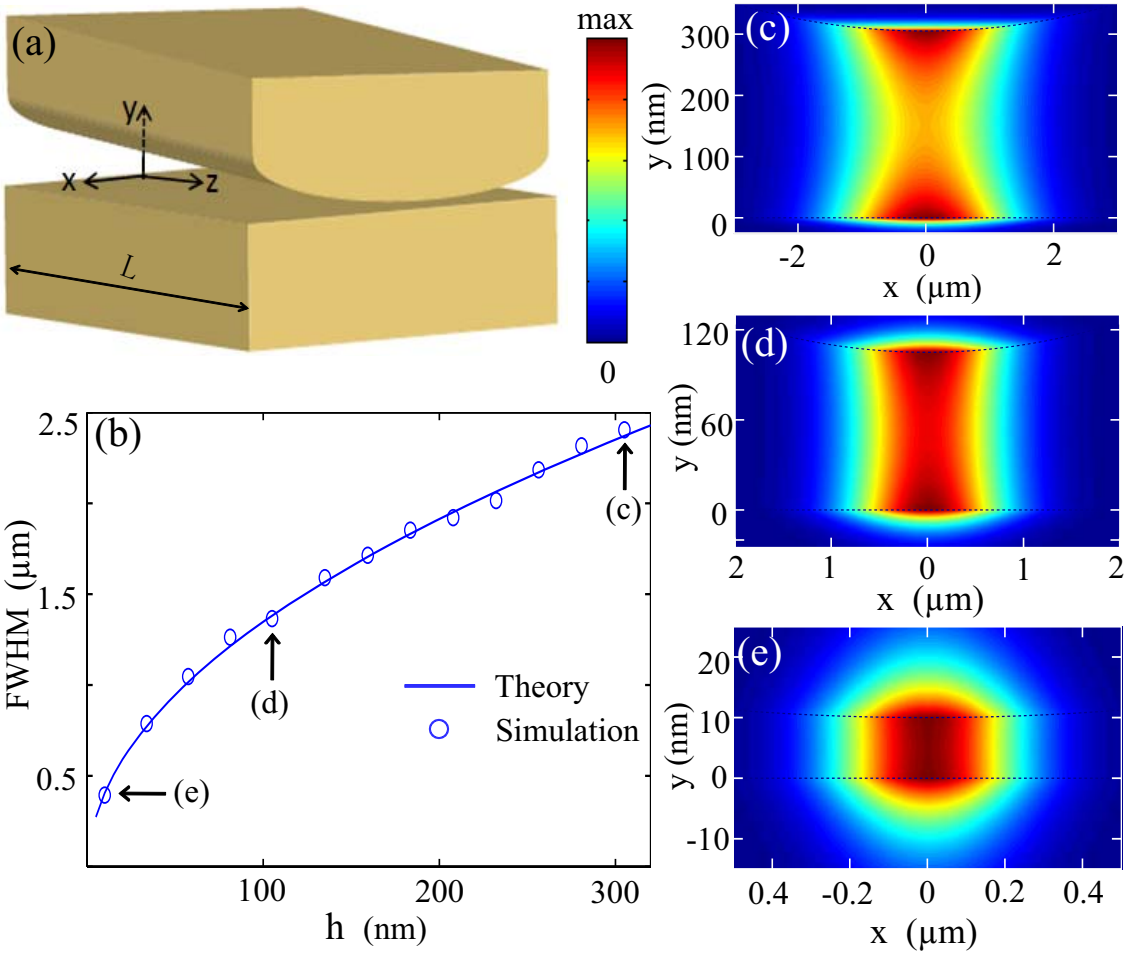

Figure 3.11: (a) A MDM structure with quadratic and linear modulation of the dielectric layer width in the x and z direction respectively. The tapering angle along z direction is θ and the structure length is L. (b) FWHM of $|H|^2$ along the x direction for the fundamental modes with different dielectric layer widths in the $x = 0$ plane ($R_0 = 100\ \mu m$). Both theoretical (solid lines) and numerical (circles) results are shown. (c)-(e) Transverse filed distributions (simulation, $|H|^2$) for the three cases marked in (b).

a tilting angle θ. During propagation, light would be more and more tightly confined in both transverse directions due to the increasingly stronger potential and narrower dielectric layer width. To describe the nanofocusing process, we derive closed form analytical formulas and deploy simulations to show the field evolution.

In our study, the dielectric is air ($\varepsilon_d = 1$) and the metal is silver, for which we use the Drude model with the same parameters as in Section 3.2.1. In a flat MDM structure, the effective refractive index of the symmetric mode (with respect to the magnetic field distribution) can be expressed as [similar to Eq. (3.4)]:

$$n_{\text{eff}}(h) = a/h + b = (a_1 + ia_2)/h + b_1 + ib_2, \tag{3.33}$$

where both a and b can be extracted from data fitting. In the structure shown in

Fig. 3.11(a), the width of the dielectric layer is

$$h(x,z) = h(0,z) + x^2/2R_0, \tag{3.34}$$

where R_0 is the effective radius [$R_0 \gg h_0 = h(0,0), |x|$]. We define that $h(z) = h(0,z)$, and with a tilting angle θ we get

$$h(z) = h_0 - \theta z. \tag{3.35}$$

In this waveguide, we obtain a longitudinally changing parabolic plasmonic potential under the condition of $x^2 \ll 2h(z)R_0$:

$$n_{\text{eff}}(x,z) = n(z)(1 - \frac{1}{2}\Omega^2(z)x^2), \tag{3.36}$$

where $n(z) = a/h(z) + b$, and $\Omega(z) = \sqrt{a/[n(z)R_0h^2(z)]}$ is the focusing strength. In this potential, we consider only the adiabatic nanofocusing of the fundamental modes, as it is symmetric along horizontal direction and is mainly excited by end-fire coupling (see Fig. 3.11). Throughout this section, for simplicity we characterize the nanofocusing effect by the enhancement of the magnetic filed, which is similar to what is shown Ref. [180]. Based on the expressions of the fundamental mode in parabolic potentials shown in Eq. (3.13), the adiabatic approximation [149] and the TM mode approximation (ignore the components of H_y, H_z and E_x), the magnetic field can be expressed as:

$$H(x,y,z) = H_x(x,y,z) = H_0(z)\exp[i\int_0^z \beta(z)dz]\exp[-\tfrac{x^2}{2\mu^2(z)}]A(x,y,z). \tag{3.37}$$

with

$$H_0(z) = H_x(0,0,z); \quad \beta(z) = n(z)k_0 - \Omega(z)/2 = \beta_1(z) + i\beta_2(z), \tag{3.38}$$

and the effective mode width along x:

$$\mu(z) = [k_0 n(z)\Omega(z)]^{-1/2}, \tag{3.39}$$

where k_0 is angular wavenumber in vacuum, and $A(x,y,z)$ is the eigenfield distribution of H_x, which can be found in Ref. [10].

The full width at half maximum (FWHM) of $|H|^2$ for the fundamental mode can be expressed as:

$$\text{FWHM} = 2\sqrt{\ln 2}\,|\mu(z)|\,. \tag{3.40}$$

In Fig. 3.11(b) we show FWHM for the fundamental mode along x direction at different h with $R_0 = 100$ μm and $\lambda = 632.8$ nm. For simulation we use Lumerical Mode Solutions (the calculation is based on eigenmode axial coupling method [121]). In Figs. 3.11(c)-(e) we show the simulation results of the transverse field distribution of $|H|^2$ at three points marked in Fig. 3.11(b) of $h = 10$ nm, 105 nm and 305 nm respectively. It is obvious that with decreasing h, the mode is more and more

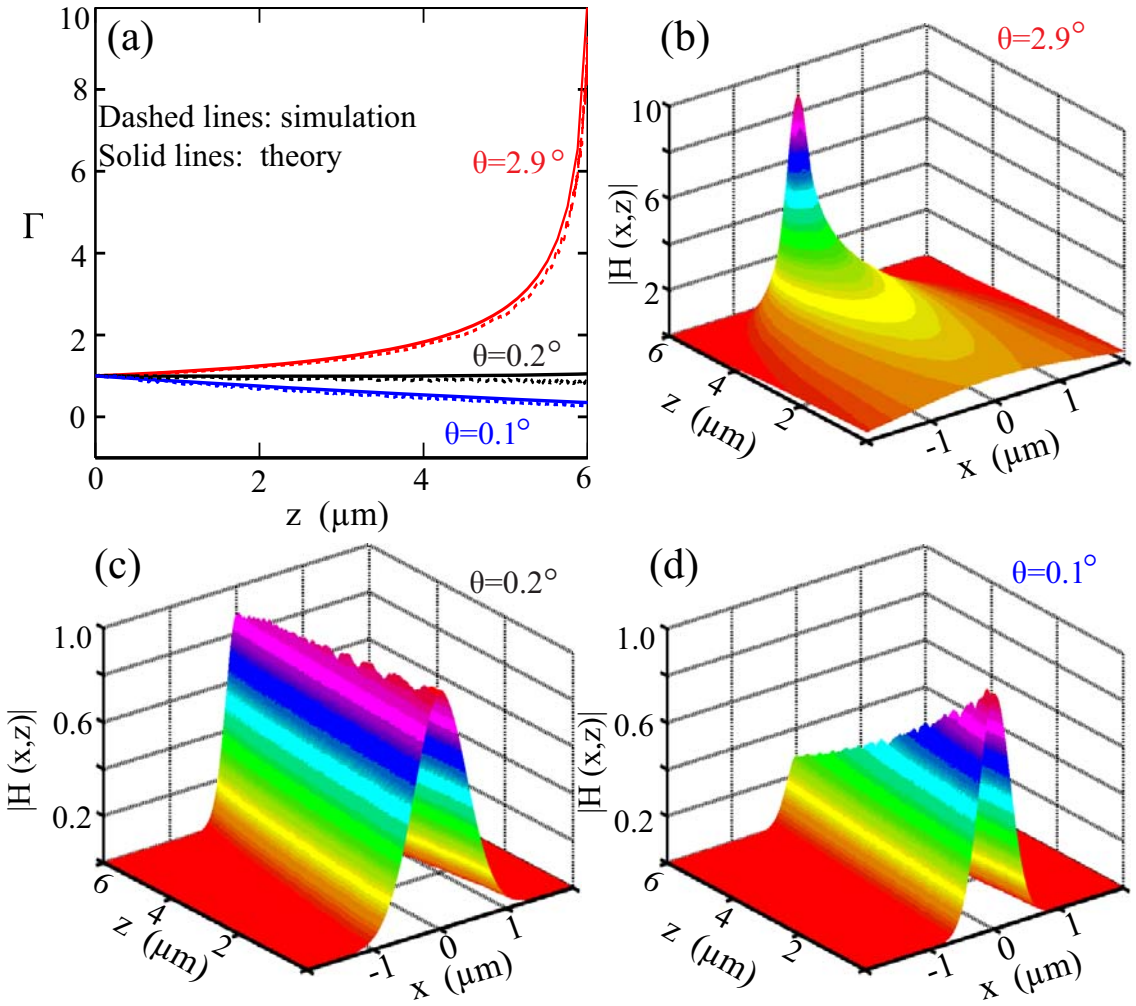

Figure 3.12: (a) Field enhancement along propagation with $L = 6\ \mu m$, output dielectric layer width $h(L) = 5$ nm and $R_0 = 100\ \mu$m. Both theoretical (solid lines) and numerical (dashed lines) are shown for three angles $\theta \approx 2.9°,\ 0.2°,\ 0.1°$. The corresponding critical angle is approximate 0.2°. (b)-(d) Simulation results of the filed distribution ($|H|^2$ in the plane $y = 0$) for the three cases shown in (a).

compressed in both transverse directions [we note here that Figs. 3.11(c)-(e) are shown in different scales].

When $R_0 \gg h_0$ and $x^2/2R_0 \ll h(z)$, the filed distribution along the two transverse directions can be decoupled. Based on Eq. (3.37), the integrated energy flow along z direction is:

$$P(z) = \frac{c^2\sqrt{\pi}}{8\pi\omega}\,|\mu(z)|\,|H_0(z)|^2 \exp[-L(z)]P_y(z), \tag{3.41}$$

where $L(z) = 2\int_0^z \beta_2(z')dz' \approx 2k_0a_2/\theta \ln[h(0)/h(z)] + 2k_0b_2z$ which is a factor indicating the accumulated Ohmic loss, c is the speed of light and ω is the angular frequency. $P_y(z)$ is the energy flow integrated along y in the $x = 0$ plane and the specific expression can be found in Ref. [180]. We define a field enhancement factor: $\Gamma(z) = H_0(z)/H_0(0)$ and according to the law of energy conservation this factor

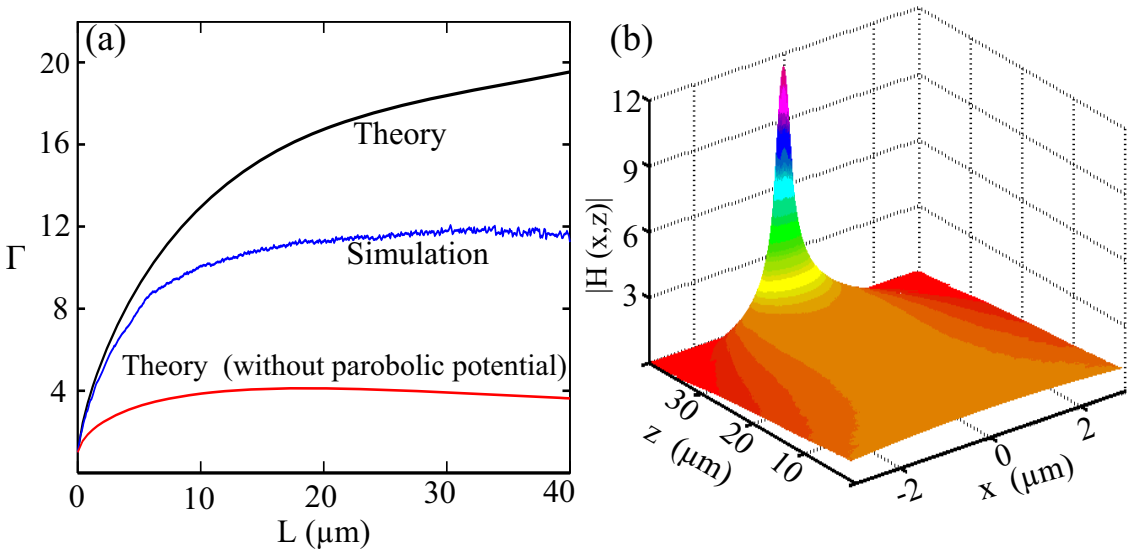

Figure 3.13: a) Filed enhancement for different waveguide lengths L and other parameters are the same as in Fig. 3.12. The nanofocusing of the taper in Refs. [180, 182] (without parabolic potential) is also shown for comparison(bottom line). (b) Simulation results of the filed distribution ($|H|^2$ in the plane $y = 0$) for $L = 40$ μm.

satisfies:

$$\Gamma(z) = \sqrt{|\mu(0)/\mu(z)|}\sqrt{P_y(0)/P_y(z)}\exp\left[-L(z)\right]. \tag{3.42}$$

The three terms on the righthand side of Eq. (3.42) come from increasingly stronger parabolic potentials, decreasing dielectric layer widths and Ohmic losses, respectively. Compared to the structures shown in Refs. [180–182], the extra term originating from the tapered parabolic potentials ($\sqrt{|\mu(0)/\mu(z)|}$) makes the focusing capabilities of our proposed structure stronger.

Field enhancement in tapered potentials

To show specifically the focusing capabilities, firstly we fix the length of our structure to $L = 6$ μm. Also the height at the output is fixed at $h(L) = 5$ nm. We summarize our results in Fig. 3.12 for three tilting angles $\theta \approx 2.9°,\ 0.2°,\ 0.1°$ (the corresponding input heights are $h_0 = 305$ nm, 25 nm, 10 nm and $\lambda = 632.8$ nm, all in the adiabatic regime), and theoretical [Eq. (3.42)] and simulation results (Lumerical Mode Solutions) agree well. The critical tapering angle for this structure is approximately $\theta \approx 0.2°$ and at this angle the Ohmic losses can be fully compensated in terms of field amplitude maintain, as shown in Fig. 3.12(a). The filed can be further enhanced at tapering angles larger than the optimal angle. We show more details of the light focusing processes for three tapering angles in Figs. 3.12(b)-(d) (simulation, $|H|^2$ in the plane $y = 0$). It is obvious that during propagation light is more and more suppressed by the increasingly stronger parabolic potentials along x direction.

Finally we study how the structure length L affects the focusing capabilities. For simplicity we the fix tapering angle to $\theta \approx 2.9°$ and $\lambda = 632.8$ nm. As discussed in Refs. [159, 180, 182], for longer propagation distances, Ohmic losses will balance or even eliminate the focusing effects. We investigate the structure up to a $L = 40$ μm. In Fig. 3.13(a), monotonic increasing field enhancement is observed, and compared to the structures studied in Refs. [159, 180, 182] this unusual feature is obviously due to strong focusing effects of the symmetric parabolic potentials we introduce. For comparison, we show the nanofocusing of transverse uniform taper investigated in Refs. [180, 182] (without parabolic potential) in Fig. 3.13(a) (bottom line), which shows monotonic increasing field enhancement only up to 18 μm and the enhancement factor is much lower. Filed distribution for $L = 40$ μm is shown in Fig. 3.13(b) (simulation, $|H|^2$ in the plane $y = 0$). For larger L, the fundamental mode will spread out more [the confinement along x is characterized by mode width $\eta(z)$, see Fig. 3.11(b)]. Then our theoretic model will be less accurate considering the parabolic potential approximation condition $x^2 \ll 2h(z)R_0$. Larger discrepancies with increasing L are observed as shown in Fig. 3.13(a).

Conclusion

In conclusion we have proposed and studied adiabatic nanofocusing of the fundamental modes in plasmonic parabolic potentials. The potentials are obtained in MDM structures with quadratic modulation of the dielectric layer width in the horizontal direction and linear modulation in the longitudinal direction. We show that there is a critical tapering angle above which the field enhancement can be achieved. Moreover, we demonstrate that our structure shows better focusing capabilities and supports monotonic increasing field enhancement over longer propagation distances compared to those previously reported in the adiabatic regimes [159, 180, 182]. The field enhancement can be further improved by extending it to nonadiabatic regimes [181] (larger tapering angles) or/and decreasing the output heights of the dielectric layers. The structure proposed here corresponds to a broad metal wire above a metal plate and thus is feasible to fabricate. We anticipate that the mechanism of suppressing light by increasingly stronger symmetric potentials can find a variety applications, such as plasmonic lasers, nanoparticle probing, hyperfine spectroscopy, and enhanced nonlinear effects, where significant local field enhancement is required.

3.3 Plasmonic Airy beam manipulation in linear potentials

In this section we demonstrate, both theoretically and numerically, the efficient manipulation of plasmonic Airy beams in linear optical potentials produced by a wedged metal-dielectric-metal structure. By varying the angle between the metallic plates, we can accelerate, compensate or reverse the self-deflection of the plasmonic Airy beams without compromising the self-healing properties. We also show that in the linear potentials the Airy plasmons of different wavelengths could be routed

into different directions, creating new opportunities for optical steering and manipulation.

3.3.1 Photonic and plasmonic Airy beam in free space

The study of Airy wavepackets dates back to the work of Berry and Balz in 1979 [184]. They found that for the Schrödinger equation in free space, if the wavepacket has an initial Airy distribution, there are two unusual features for the evolution of the wavepacket in time domain: (1) the wavepacket maintains the nonspreading Airy distribution and (2) the wave packet is self-accelerating following a parabolic trajectory. It is worth mentioning that both features, especially the second one of self-accelerating in free space, are quite counterintuitive, but they do not contradict the Ehrenfest theorem [118] as the ideal Airy wave packet proposed by Berry and Balz carries infinite energy and thus there is no well defined centre of the wavepacket.

As we discussed before (Section 3.1) there is close similarity between the Schrödinger equation and the paraxial wave equation. So it is quite natural to introduce the concept of the Airy wavepacket to the photonic regime, which is then termed as Airy beam [133, 185]. The first challenge for the real experimental demonstration on the Airy beam is that the ideal Airy beam carries infinite energy, and thus should be truncated to make it carry finite energy. An exponential truncation was firstly proposed in Ref. [185] and shortly afterwards the Airy beam was demonstrated experimentally [133]. Also the same group predicted that plasmonic Airy beam can be excited on the metal surface [186] and then three other groups demonstrate such beams almost at the same time with different experimental setups and techniques [134–136]. In Fig. 3.14 we show the first demonstration of the Airy beams in Fig. 3.14(a), prediction of plasmonic Airy beam on metal surface in Fig. 3.14(b), one of the experimental setups and the observation of plasmonic Airy beams in Fig. 3.14(c) and (d), respectively.

Those features of asymmetric field profile and self-deflection of Airy beams have been employed for various applications, including optical trapping [187], plasma guiding [188], and light bullet generation [189, 190]. Being combined with the virtue of surface plasmon polaritons, the plasmonic Airy beams could be a promising candidate for subwavelength beam manipulation and on-chip signal processing, in the emerging fields of nanophotonics and plasmonics.

3.3.2 Airy beam steering in linear plasmonic potentials

The manipulation of Airy beams has been demonstrated in both linear and nonlinear regimes [191–194]. However, these schemes are reliant on the Airy beam generation processes, and are highly dependent on the amplitude (nonlinear) or phase (linear) of the incident light. The drawbacks prevent those manipulation methods to be widely used. The development of more robust and flexible Airy beam manipulation mechanisms and techniques are important but still unavailable.

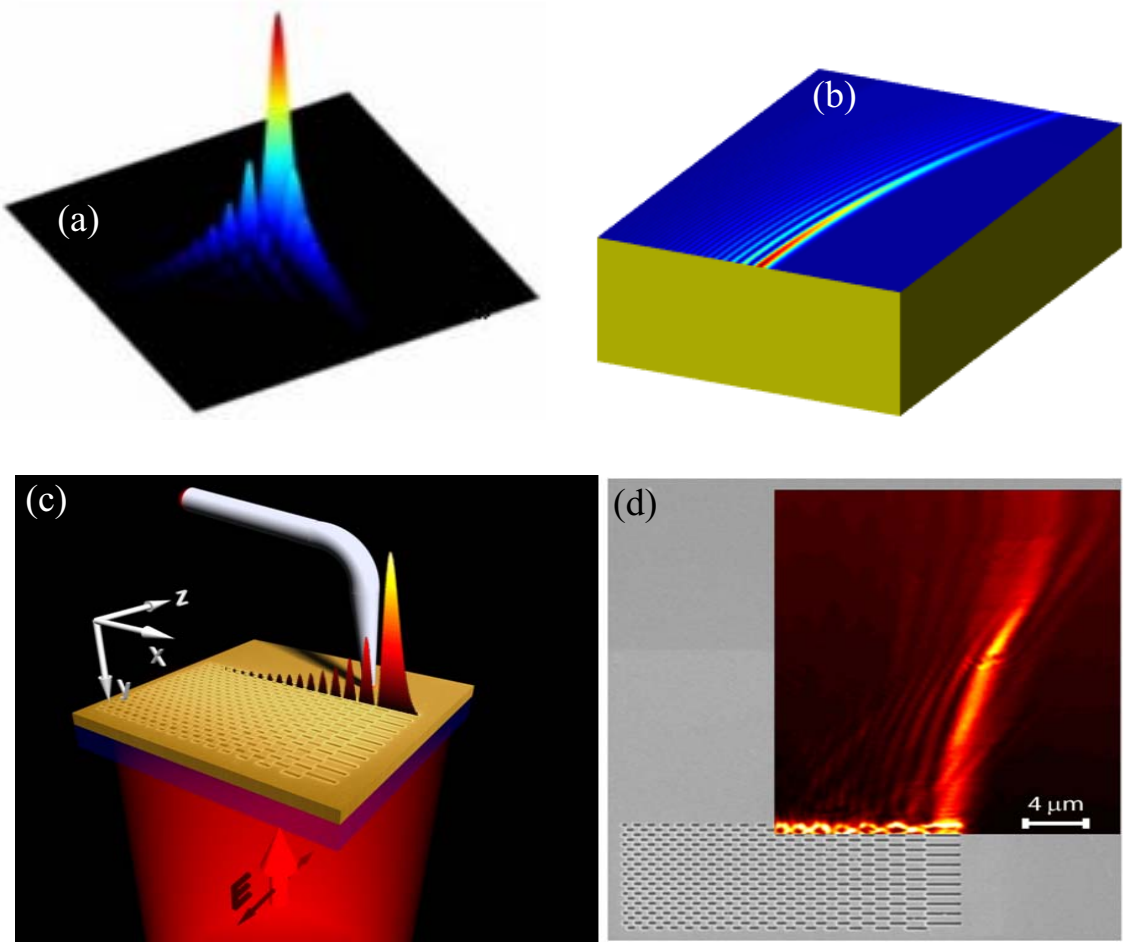

Figure 3.14: (a) First experimental demonstration of the Airy beam. (b) Plasmonic Airy beam on metal surface. (c) and (d) show one of the experimental setups and the observation of plasmonic Airy beams. After Refs. [133, 134, 186].

Linear plasmonic potentials and Airy beam steering

The control of Airy beams by linear potentials was firstly discussed by Berry and Balazs more than thirty years ago [184], but it has not attracted much attention since. In fact, the *linear potential* is the only potential that could be used to change the propagation direction of Airy beams, while preserving its non-diffracting properties [195]. To achieve a linear optical potential in the transverse direction, we utilize a linear modulation of the thickness of the dielectric layer along the x-axis, as shown in Fig. 3.15(a). In an unmodulated metal-dielectric-metal structure, the effective refractive index of the symmetric mode (with respect to the magnetic field distribution) could be expressed as [see Eq. (3.4)]: $n_{\text{eff}}(h) = \alpha/h + \beta$, where h is the width of the dielectric layer. Correspondingly, in the wedged structure shown in Fig. 3.15(a) (the tilting angle is θ and the gap width in the middle is h_0), we obtain a linear effective index distribution (linear optical potential) under the approximation of $|\theta x| \ll h_0$:

$$n(x) = n_0 - \alpha\theta x/h_0^2, \tag{3.43}$$

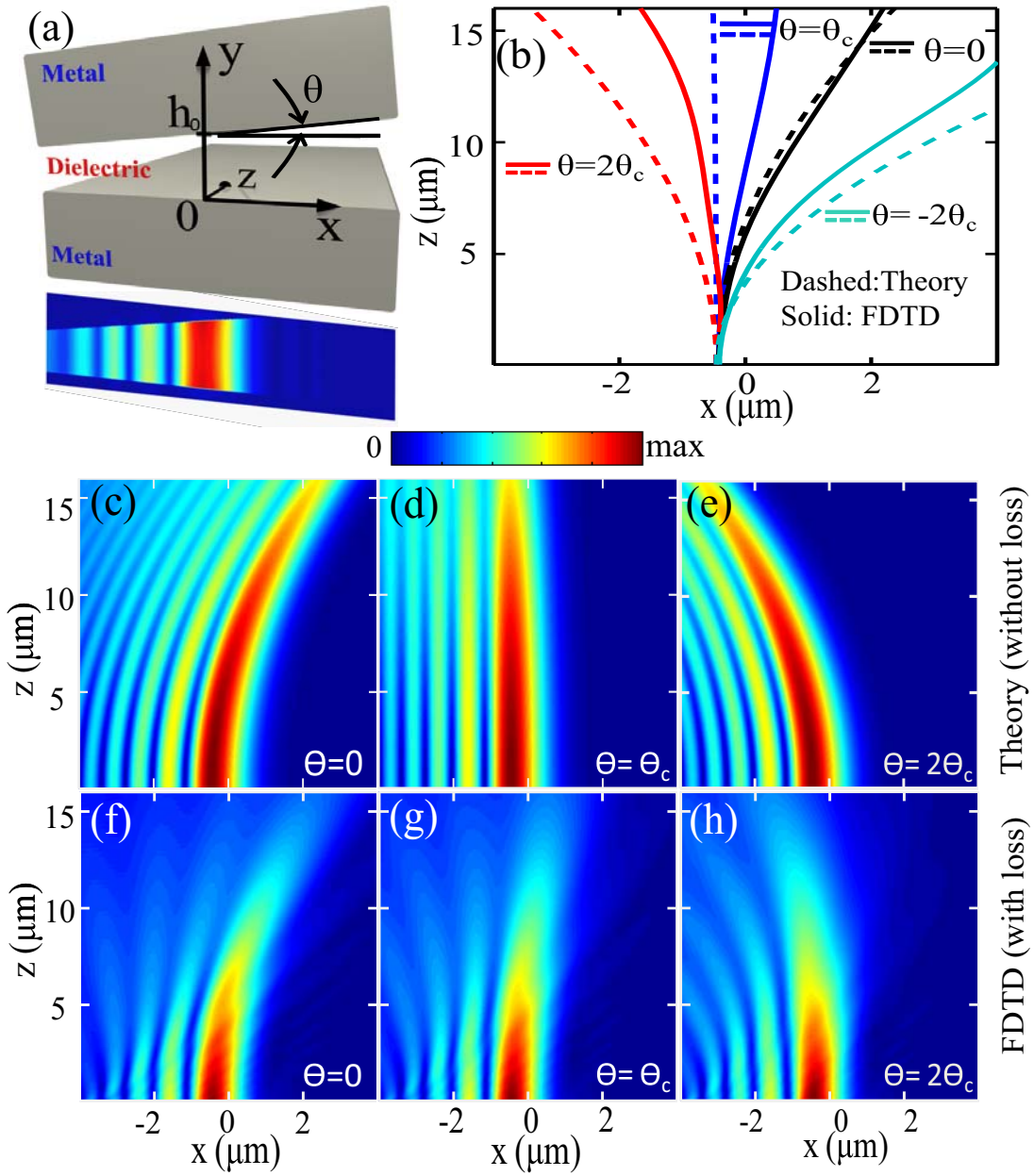

Figure 3.15: (a) Wedged metal-dielectric-metal structure with a tilting angle θ. The transverse field distribution is shown schematically below. (b) Positions of the main-lobe center of the plasmonic Airy beam for four tilting angles. Both theoretical (no losses, dashed lines) and numerical (with losses, solid lines) results are shown. Field distributions of the plasmonic Airy beam in the plane $y = 0$ are shown in (c-e) (theory, $|\psi(x, z)|$) and (f-h) (numerical, $|E|$). The parameters are: $\lambda = 632.8\,\text{nm}$, $h_0 = 60\,\text{nm}$, $a = 0.1$, and $x_0 = 500\,\text{nm}$. The corresponding critical angle is $\theta_c = 0.175°$.

where $n_0 = n_{\text{eff}}(h_0)$. Using the effective index method, we can express the vertical electric field as [156] $E_y(x, y, z) = A(x, y)\psi(x, z)\exp(in_0kz)$, where $A(x, y)$ is the plasmon eigenmode field, $\psi(x, z)$ is the envelope function and k is the wavenumber

in vacuum. When $|\theta\Delta x| \ll h_0$, $A(x,y)$ and $\psi(x,z)$ can be decoupled [156]. While the expression for $A(x,y)$ can be found in Eq.(3.9) and Eq.(3.10), the equation for $\psi(x,z)$ under paraxial approximation is:

$$i\frac{\partial\psi}{\partial\xi} + fs\psi + \frac{1}{2}\frac{\partial^2\psi}{\partial s^2} = 0, \tag{3.44}$$

where $s = x/x_0$ (x_0 is the characteristic width of the first Airy beam lobe), $\xi = z/(n_0 k x_0^2)$, and $f = -\alpha\theta k^2 n_0 x_0^3/h_0^2$ is effective optical force. Equation (3.44) is exactly the Shrödinger equation for a particle in a linear potential (fs). This problem has a known solution [196, 197]:

$$\begin{aligned}\psi(s,\xi) = \sqrt{\tfrac{1}{2\pi i\xi}}\exp[i(fs\xi - \tfrac{f^2\xi^3}{6})]\int_{-\infty}^{+\infty}\psi(\chi,0)\\ \exp(\tfrac{i}{2\xi}[(s - \tfrac{f\xi^2}{2}) - \chi]^2)d\chi,\end{aligned} \tag{3.45}$$

where $\psi(\chi,0)$ is the initial beam distribution. For an initial truncated Airy distribution $\psi(s,0) = Ai(s)\exp(as)$ ($a > 0$ is the apodization parameter truncating the negative s part of the Airy beam distribution, and thus the deflection of Airy beam in free space is towards the positive x direction), we obtain the solution [185, 197]:

$$\begin{aligned}\psi(s,\xi) = Ai[s - \tfrac{1}{4}(1+2f)\xi^2 + ia\xi]\exp[a(s - \tfrac{f\xi^2}{2}\\ -\tfrac{\xi^2}{2})]\exp[i(-\tfrac{f^2\xi^3}{6} + fs\xi - \tfrac{f\xi^3}{4} - \tfrac{\xi^3}{12} + \tfrac{a^2\xi}{2} + \tfrac{s\xi}{2})].\end{aligned} \tag{3.46}$$

From Eq. (3.46) it follows that there exists a critical tilting angle $\theta_c = h_0^2/(2\alpha k^2 n_0 x_0^3)$ [satisfying the condition $f(\theta = \theta_c) = -1/2$] for which the Airy function becomes a stationary solution. Furthermore, Eq. (3.46) shows that when $a \ll 1$ the deflection of the plasmonic Airy beam could be accelerated ($\theta < 0$), compensated ($\theta = \theta_c$) or even reversed ($\theta > \theta_c$). We note that $\psi(x,z)$ is also the envelope function of E_z and therefore of $|E|$, considering the fact that $E_x \ll E_y, E_z$.

Next, we compare our theoretical results of Eq. (3.46) for $|\psi(x,z)|$ with numerical results ($|E|$) based on finite-difference time-domain (FDTD) technique (Lumerical) in Figs. 3.15(b-h). In the simulations, we make the mesh size to 0.5 nm in the region close to the metal dielectric interface and choose PML (perfectly matched layer) boundary conditions. Parameters used here are $\lambda = 632.8\,\text{nm}$, $h_0 = 60\,\text{nm}$, $a = 0.1$, $x_0 = 500\,\text{nm}$. The dielectric is air ($\varepsilon_\text{d} = 1$) and the metal is silver. We use the Drude model for silver, $\varepsilon_\text{m} = 1 - \omega_p^2/(\omega^2 + i\omega\omega_c)$, where $\omega_p = 1.37\times10^{16}\,\text{rad/s}$ and $\omega_c = 7.25\times10^{13}\,\text{rad/s}$. Figure 3.15(b) shows the positions of the main-lobe center of the Airy plasmons for four values of the tilting angle ($\theta_c = 0.175°$). For three cases, the field distribution in the plane $y = 0$ is shown in Figs. 3.15(c-h). We observe that the deflection of plasmonic Airy beams could be indeed accelerated [$\theta < 0$, Fig. 3.15(b)], compensated [$\theta = \theta_c$, Figs. 3.15(b,d,g)] or even reversed [$\theta = \theta_c$, Figs. 3.15(b,e,h)]. In general, there is a good qualitative agreement between our analytical theory and the numerical results showing that this analysis can be used to predict the behavior of plasmonic Airy beams. As θ increases, however, larger discrepancies between the theoretical and numerical results are observed [Fig. 3.15(b)]. This is because larger tilting angles render both the linear potential and paraxial wave approximations less accurate.

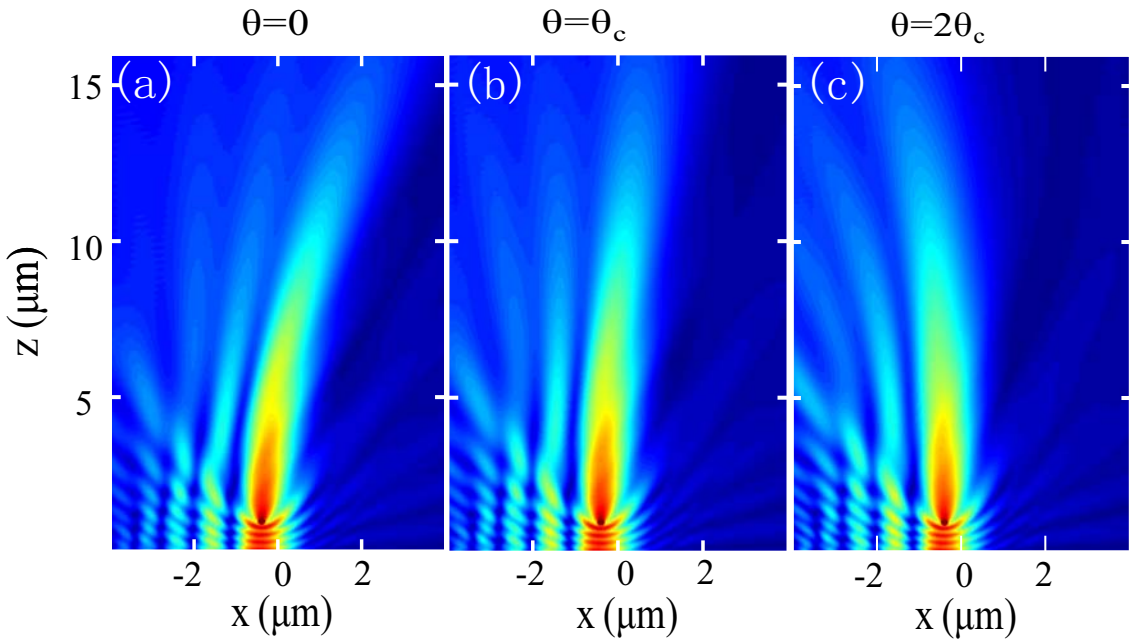

Figure 3.16: Numerical results for the field distribution ($|E|$) of plasmonic Airy beams in linear optical potentials with perturbations for three tilting angles. An ellipsoid particle ($\epsilon = 2.25$) with $(R_x, R_y, R_z) = (0.1, 0.025, 0.1)\,\mu$m is centered at $(x, y, z) = (-0.4, 0.025, 1)\,\mu$m. Other parameters are the same as in Fig. 3.15.

Self-healing properties of Airy beams in plasmonic linear potentials

One of the most important properties of Airy beams is their self-healing capability. This has been demonstrated both experimentally and theoretically for free-space Airy beams [187, 198], which are of a great significance for particle guidance. Here we demonstrate that the introduced linear potentials for the manipulation of Airy beams do not compromise their self-healing properties.

The diffraction patterns of the unperturbed and perturbed plasmonic Airy beam in linear potentials are denoted by $U_a(x, z)$ [as shown in Fig. 3.15(c-h)] and $U_p(x, z)$ respectively, with a small perturbation (*e.g.* a bump or dent or an extra particle) located at (x_0, z_0). Now let us think of a complementary case: the perturbation is removed and the occupied area is made transparent; other areas in the propagation plane are made opaque. The plasmonic Airy beam can be fully blocked by those opaque areas, and can only propagate through the aperture which is made by removing the perturbation. The scattering pattern of this complementary case is denoted by $U_{pa}(x, z)$. According to Eq. (3.45), the evolution of Airy beams in linear potentials obeys the Fresnel transform [196]. This means that we can understand the effects of perturbations on Airy beams by applying Babinet's principle [2, 198], irrespective of the existence of the linear potentials. According to Babinet's principle, as $U_{pa}(x, z)$ and $U_p(x, z)$ correspond to complementary diffraction screens, the following relation is satisfied: $U_{pa}(x, z) + U_p(x, z) = U_a(x, z)$. If the perturbation is of small size and thus rapidly diffracting [2, 187], in areas far from the perturbation position (x_0, z_0), we have $U_p(x, z) \approx 0$ and thus $U_{pa}(x, z) \approx U_a(x, z)$. This

means that after some propagation distances beyond the perturbation, the scattering pattern will be the same as that without the perturbation, indicating that in linear potentials the plasmonic Airy beams still possess self-healing capabilities as the free propagating Airy beams do [198]. In Figs. 3.16(a-c) we show our numerical results for the diffraction patterns of the plasmonic Airy beams in the wedged metal-dielectric-metal structure where we place an ellipsoid particle ($\epsilon = 2.25$) at the position $(x, y, z) = (-0.4, 0.025, 1)\,\mu$m with $(R_x, R_y, R_z) = (0.1, 0.025, 0.1)\,\mu$m. Other parameters are the same as in Fig. 3.15. Importantly, we observe the self-healing properties in all three cases.

Multi-color Airy beams steering in plasmonic linear potentials

Finally, we study how the linear potential affects the propagation of plasmonic Airy beams of different wavelengths. As the critical angle θ_c depends on the wavelength, plasmonic Airy beams generated at different wavelengths will be steered into different directions. Figure 3.17(a) shows the critical angles for the wavelength range of $0.5 - 1.5\,\mu$m at $h_0 = 60\,$nm. Shorter wavelength corresponds to smaller critical angle, and this means that the deflection of shorter wavelength plasmonic Airy beam is easier to control. For $\theta = 0.458°$ we obtain a critical linear potential that could compensate the deflection of the plasmonic Airy beam and force it to propagate straight. This is shown in Fig. 3.17(c) for $\lambda = 1\,\mu$m beam. When the corresponding critical angle is smaller, the deflection direction is reversed, as is shown in Fig. 3.17(b) for $\lambda = 0.6\,\mu$m. The action of the linear potential on longer wavelength plasmonic Airy beams is weaker, and then the deflection direction is only slightly modified, being still towards the positive x direction [see Fig. 3.17(d)]. As plasmonic Airy beams of different colors could be directed into different directions, the mechanism shown here could find possible applications in routing of signals on a photonic chip into different processing channels.

Conclusion

In conclusion, we have studied the propagation of Airy plasmon beams in linear optical potentials created by a transversely wedged metal-dielectric-metal structure. By employing an analytical model and direct numerical simulations, we have demonstrated that by changing the angle between the metallic plates, the deflection of the Airy plasmon could be enhanced, compensated, or even reversed without compromising their self-healing properties. We have also shown that the linear potential could be used to switch multi-color plasmonic Airy beams into different directions. The mechanism shown here opens a door to various applications, such as optical transportation, subwavelength beam manipulation, light bullets control, and on-chip signal processing.

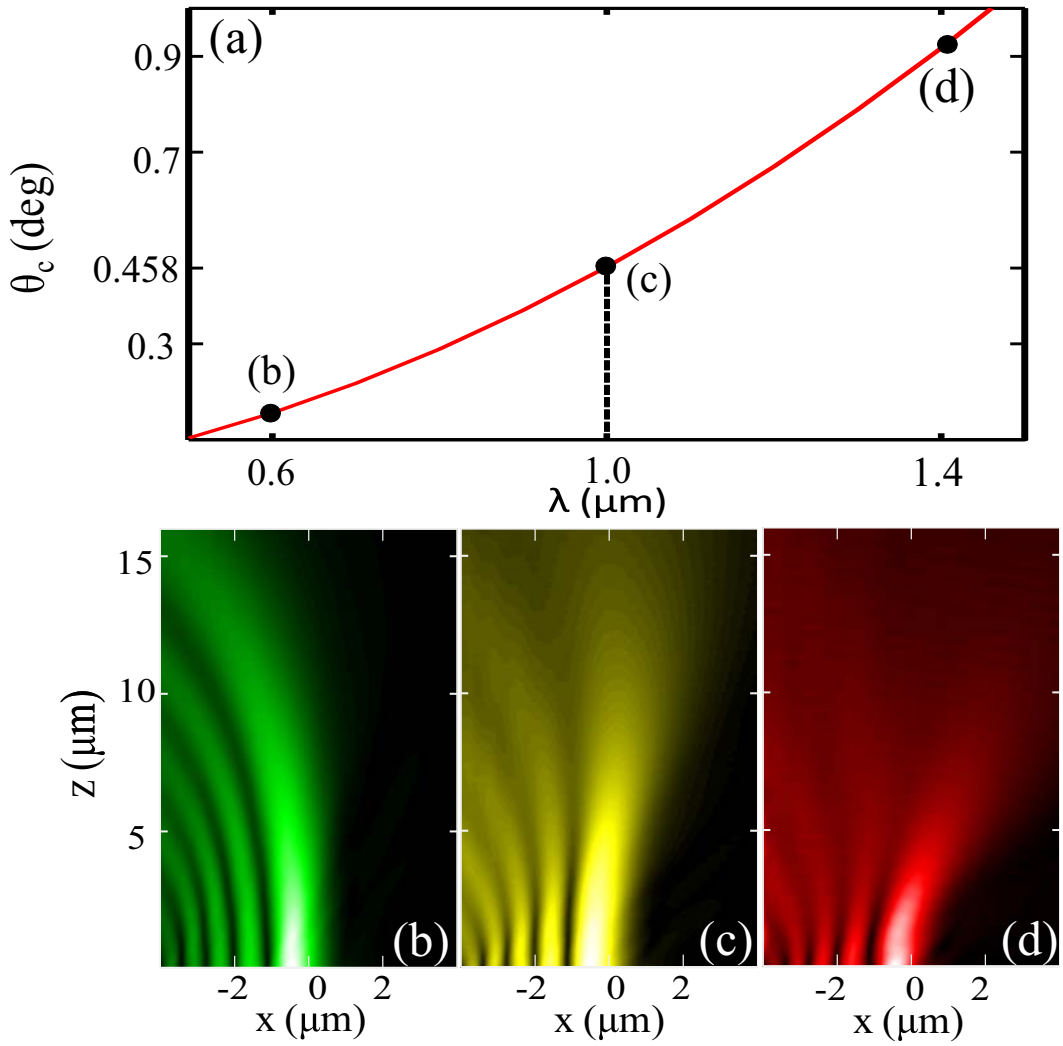

Figure 3.17: (a) Critical angle *vs.* wavelength in the range of $0.5 - 1.5\,\mu$m. (b-d) Numerical results for the field distributions ($|E|$) of three plasmonic Airy beams of wavelengths $0.6\,\mu$m, $1\,\mu$m and $1.4\,\mu$m presented in false colors. Parameters used are the same as in Fig. 3.15, with $\theta = 0.458°$, which is the critical angle at $\lambda = 1\,\mu$m (point c).

3.4 Summary

In this chapter, after a brief description of the similarity between Schrödinger equation and the paraxial wave equation, we introduce the concept of plasmonic potentials and employ different kinds of potentials for various beam manipulations. We achieve parabolic potentials in quadratically modulated MDM structures and related beam manipulations include: (1) polychromatic nanofocusing in full parabolic potentials; (2) plasmonic analogue of quantum paddle balls in half parabolic potentials; (3) adiabatic nanofocusing in tapered parabolic potentials. Also we achieve linear potentials in wedged MDM structures and demonstrate flexible Airy beam

manipulations there. Here we confine the research to fundamental potentials of parabolic and linear forms only, however surely more complicated potentials can be constructed in MDM structures or other plasmonic structures for beam shaping. We note that the principles demonstrated here can be extended beyond the field of plasmonics, to other graded index structures or even to include quantum particles in parabolic potentials, serving as an efficient platform for various investigations.

CHAPTER 4

Scattering engineering by magneto-electric nanostructures with both electric and magnetic resonances

For many surface plasmon resonance based applications, such as plasmonic nanoantennas, sensing with plasmonic nanospheres, photovoltaic devices and so on, efficient shaping of scattering pattern is playing a vitally important role. Nevertheless, most approaches on scattering shaping are based on engineering of the electric responses of the nanostructures due to the fact that for most structures only electric responses are supported, especially in the optical regime. In this chapter, we introduce artificial magnetic responses and manage to shape the scattering efficiently through the interference of both electric and magnetic responses in plasmonic nanostructures. The introduction of magnetic responses brings an extra dimension of flexibility and based on that we achieve efficient scattering shaping of core-shell nanoparticles, including broadband unidirectional scattering by core-shell nanospheres and scattering pattern engineering for core-shell nanowires. We also demonstrate polarization independent Fano resonances in arrays of core-shell nanospheres.

4.1 Introduction

The study of light scattering by small particles has a long history and it is of fundamental significance in different branches of physics, such as sensing, solar cells, optical communications, *etc.* Nanoparticles have found wide applications for biomedical labeling, impacting strongly on the fields like biology and medical research [60, 63, 64, 199, 200]. Recently fostered by the flourishing fields of plasmonics and metamaterials, various novel scattering phenomena have been demonstrated, *e.g.* clocking [96], super-scattering [25, 201, 202], control of the direction of the scattered light [61, 62], nonlinear second harmonic scattering [48], and artificial antiferromagnetism [203]. It is also shown that light scattering can be significantly enhanced with the incorporation of gain materials, based on which deep subwavelength nanoscale lasing could be achieved [49, 78, 204].

For most scattering problems, efficient shaping of the scattering pattern is one

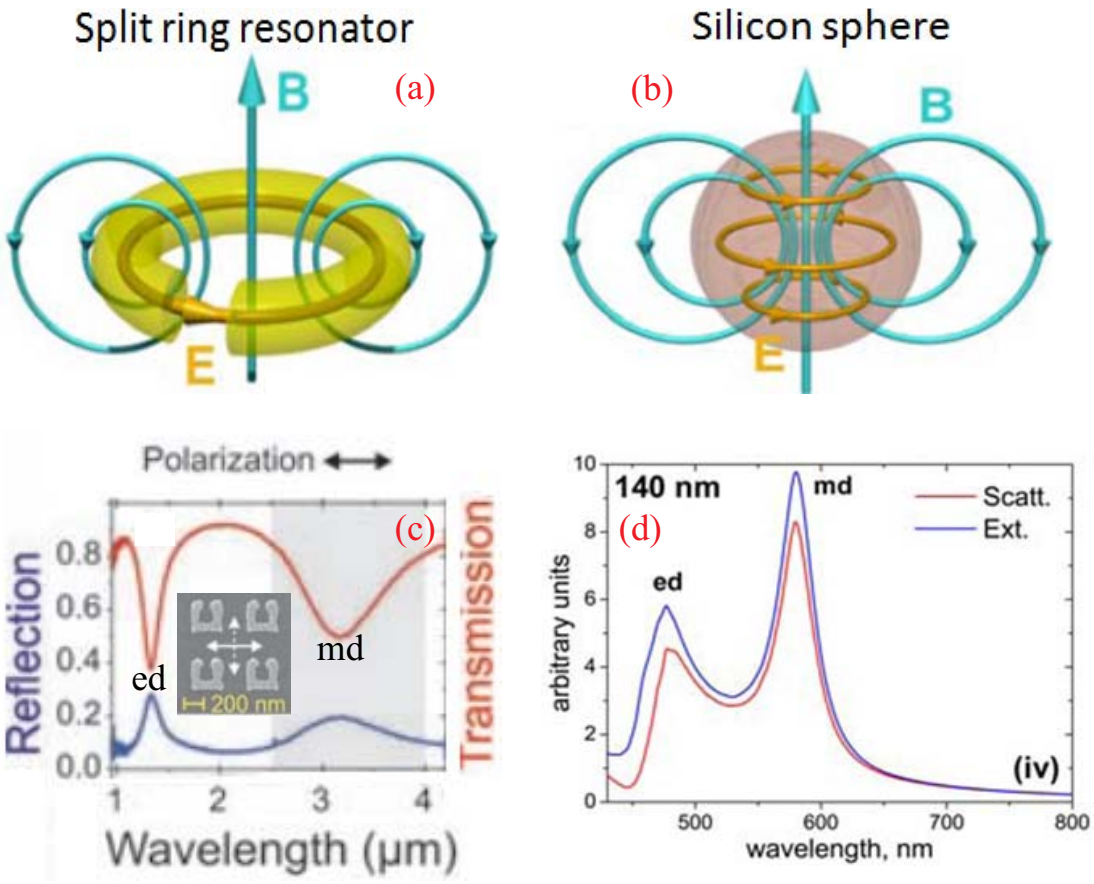

Figure 4.1: (a) and (b) show the split ring resonator and the silicon sphere respectively with strong circulating displacement currents which produce strong artificial magnetic response. (c) shows the spectral responses of the split ring resonator shown in the inset and (d) shows the spectral response of the silicon sphere of diameter 150 nm. After Refs. [205, 206].

of the most crucial issues. Nevertheless, most approaches on scattering shaping are based on engineering of the electric responses of the nanostructures. This is because most structures have only electric responses as there are very limited kinds of magnetic materials, which at the same time can usually only operate in narrow spectral regimes, and is accompanied by high losses. Of most scattering problems, the dominant response would be electric dipole (ED) response and two typical features of the scattering pattern of an ED are exhibited: (1) light will be scattered symmetrically in backward and forward directions [199] and (ii) the ED excited will have a specific orientations depending on the polarization of the incident wave, resulting in azimuthally asymmetric scattering patterns [199, 207]. However, for many applications based on the mechanism of resonant light scattering, such as nanoantennas [58, 59], sensing with nanospheres [52], and photovoltaic devices [60], usually unidirectional scattering is required. To suppress the unwanted backward scattering (reflection) and enhance the directional forward scattering, an extra reflector or coupled item [58, 59, 208–212], an extended substrate [212–215], Fabry-Pérot resonator

like structures [214, 216], and/or complicated structure engineering [217, 218] are usually employed.

We also note that if only magnetic dipole (MD) is supported in a structure, the scattering pattern would be the same as that of an individual ED due to the symmetry of Maxwell equations [199]. However, if an ED and a MD can coexist and interfere with each other, then there will be extra freedom and flexibilities for scattering shaping. Two related outstanding examples are Kerker's vanishing background condition [219] and the concept of Huygense source [220, 221]. For both examples the scattering pattern show two usual features compared to that of an individual ED or MD: (1) suppressed backward scattering and enhanced forward scattering; and (2) azimuthally asymmetric scattering. The features come directly from the interference of the ED and the MD, under the conditions of: (1) the ED and the MD overlap spectrally and (2) the ED and the MD are of the same magnitude. After the clarifications of the scattering features and the conditions, it is clear that two challenges are laying ahead: how to get the MD response and how to overlap the ED and the MD?

As we mentioned before, there are very limited kinds of materials that directly support magnetic responses, which at the same time can usually only operate in narrow spectral regimes, and is accompanied by high losses. However recently inspired by the emerging field of metamaterials [20–22], many non-magnetic structures are proven to be able to support artificial magnetic resonances, with examples include the split ring resonators [205, 222] and many other high permittivity dielectric structures [206, 223–232]. As such it is easy to excite the artificial MD but usually it is very challenging to overlap the ED and the MD. In Fig 4.1 (a) and (b) we show two well studied structures that support artificial magnetic responses: the split ring resonator and high permittivity dielectric sphere (silicon sphere). It is shown that due to the strong displacement currents, there is are strong magnetic responses of the structures [205, 206, 222]. In Fig 4.1 (c) and (d) we also show their spectral responses. It is clear that although both structures support both an ED and a MD, the two resonances are separated spectrally without efficient overlap.

4.2 Shaping the scattering of core-shell nanostructures through the interferences of electric and magnetic dipoles

In this section, we demonstrate that efficient overlapping of an ED and a MD is possible in symmetric core-shell nanostructures. We investigate two special cases of core-shell nanospheres and core-shell nanowires. It is shown that for both cases the ED and the MD are decoupled from each other and thus can be engineered to overlap spectrally. For core-shell nanospheres, the ED and the MD are of the same amplitude, thus leading to backward scattering suppression and forward scattering enhancement. For core-shell nanowires with incident p waves, as each ED corresponds to two angular momentum channels, the ED is twice the magnitude of the MD, thus leading to different scattering patterns from those of core-shell nanospheres.

4.2.1 Broadband unidirectional scattering by magneto-electric core-shell nanospheres

In this section we demonstrate the suppression of the backward scattering and enhancement of the forward directional scattering by superimposing electric and magnetic responses of core-shell nanospheres. We achieve azimuthally symmetric broadband unidirectional scattering using (metal) core - (dielectric) shell nanosphere structures without magnetic materials or extra reflectors being involved. Each nanosphere is effectively magneto-electric as it supports orthogonal ED and MD resonances, which can be engineered to coincide spectrally with the same strength [229, 233]. As the electric and the magnetic dipoles have the same strength, and they can interfere destructively in backward direction and constructively in forward direction, azimuthally symmetric unidirectional scattering can be achieved even for a single particle. Furthermore, we show that the directionality can be additionally enhanced in a chain of such particles. Although there is a tradeoff between energy confinement and directionality for different inter-particle distances, however the properties of vanishing backward scattering and azimuthal symmetry are always preserved. At the end, we demonstrate that the operating spectral regime of the unidirectional scattering is practically broadband.

Unidirectional scattering of a single core-shell nanosphere

The scattering of a spherical particle [see Fig. 4.2(a)] (single-layered or multi-layered) can be solved analytically using Mie theory [199, 234]. The far-field scattering of such particles can be expanded into orthogonal electromagnetic dipolar and multipolar scattering, with Mie coefficients a_n and b_n (both can be calculated analytically [199, 234]) corresponding to electric and magnetic moments respectively [199, 233]. The effective electric and magnetic dipolar polarizabilities can be expressed as [199]:

$$\alpha_1^e = \frac{3i}{2k^3} a_1, \;\; \alpha_1^m = \frac{3i}{2k^3} b_1, \tag{4.1}$$

where a_1 and b_1 are Mie scattering coefficients, which correspond to electric and magnetic dipole moments, respectively, and k is the angular wave number in the background material (vacuum in our case). In Fig. 4.2(b) we show the scattering efficiency spectra including the total scattering - total scattering cross section divided by the geometrical cross section of the particle (blue line) and the scattering contribution from a_1 (red line) of a silver sphere with a radius $R = 68$ nm, illuminated by a linearly polarized (along x) plane wave as shown in Fig. 4.2(a). For the permittivity of silver we use the experimental data from Ref. [235]. It is clear that the sphere can be approximated as an electric dipole for the wavelength range under consideration. The scattering patterns at the resonant wavelength of 440 nm are shown on the right of Fig. 4.2(c) for both p (line with crosses) and s (solid line) polarizations [scattering plane parallel ($\varphi = 0$) and perpendicular to the polarization ($\varphi = 90°$) of the incident plane wave, respectively]. The three-dimensional (3D) scattering pattern is shown on the left of Fig. 4.2(c) with a part cutoff for better

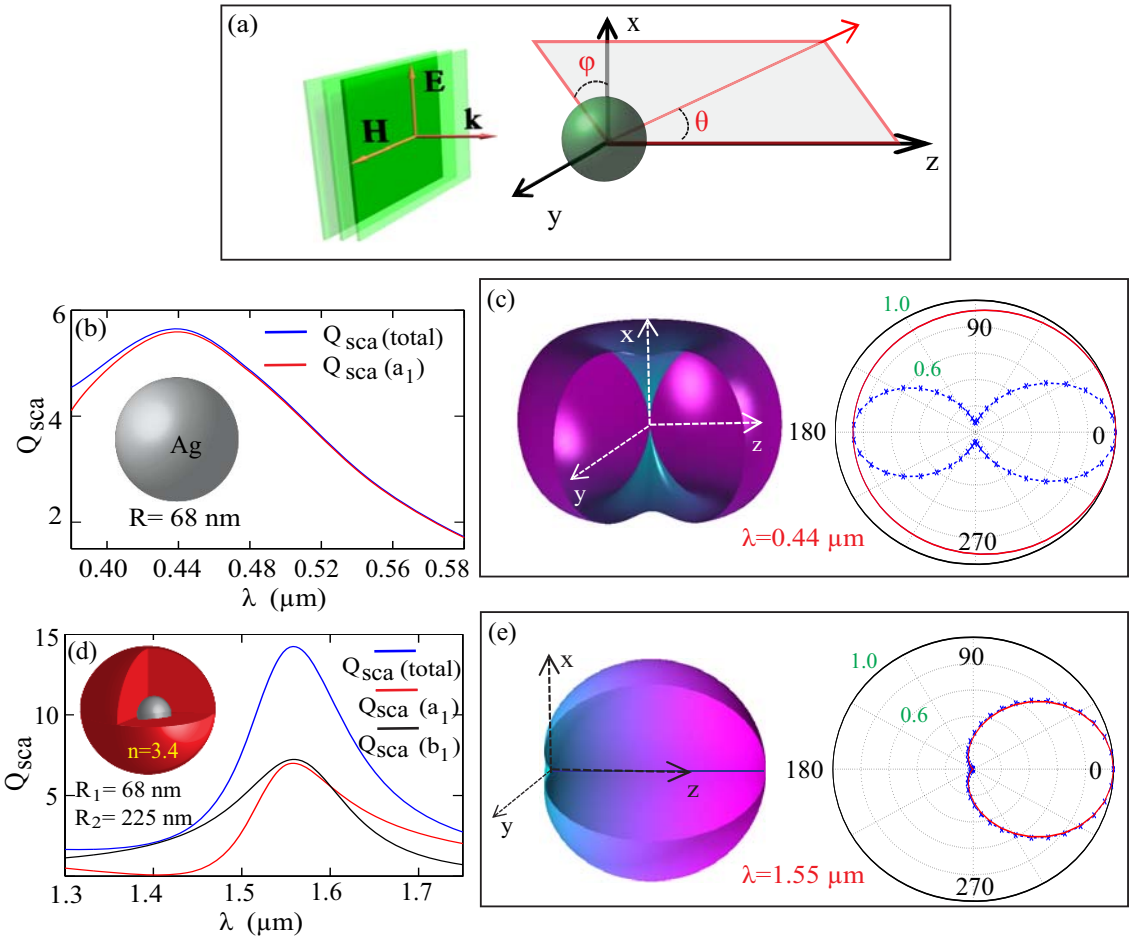

Figure 4.2: (a) Scattering of an incident plane wave by a spherical particle. The electric field is polarized along x and the wave is propagating along z. (b) Scattering efficiency spectra (total and the contribution from a_1) for Ag sphere (inset) of radius 68 nm and (c) left: corresponding 3D scattering pattern at the resonant wavelength of 440 nm (with a part cut for bettering viewing); right: scattering pattern for both s (solid line) and p (line with crosses) polarizations. (d) Scattering efficiency spectra (total and the contribution from a_1 and b_1) for a core-shell nanosphere (inset) with inner radius 68 nm and outer radius 225 nm. The core is silver and the shell is dielectric with $n = 3.4$. (e) Left: corresponding 3D scattering pattern at the resonant wavelength of 1550 nm; right: scattering patterns for both p and s polarizations.

visibility. Two typical features of the scattering by a single dipole are seen: (i) azimuthal asymmetry and (ii) symmetry in the backward and forward directions. We note that spherical symmetry of the silver sphere does not guarantee azimuthally symmetric scattering because the sphere has only dominant electric response.

In contrast, in Fig. 4.2(d) we show the scattering efficiency spectra for a core-shell nanosphere (total and the contribution from a_1 and b_1) with a silver core and dielectric shell of refractive index $n = 3.4$ (*e.g.* GaAs, Si or Ge) with inner radius $R_1 = 68$ nm and outer radius $R_2 = 225$ nm (inset). Considering that a_1 and b_1 correspond to the first order electric and magnetic eigenmodes of the core-

shell nanosphere respectively, the core-shell nanosphere can be effectively viewed as a combination of a pair of orthogonal electric and magnetic dipoles. We note here that spherical symmetry leads to the orthogonality of the two modes and thus they are not coupled to each other [236]. Due to the orthogonality, it is possible to superimpose these two modes spectrally. To match the strength of the electric and magnetic dipoles with the same strength, further geometric tuning (change of the radius aspect ratios) is required [229, 233]. For most structures that do not exhibit specific symmetries [236], although both electric and magnetic resonances are supported, they are coupled to each other and therefore the resonances are spectrally separated. Due to the coexistence of the ED and MD resonances, different from a single metal sphere, the core-shell nanosphere is effectively a magneto-electric scatterer according to Eq. (4.1).

When higher order modes excitation is negligible ($a_n = b_n = 0,\ n \geq 2$), the scattering intensity (correspond to the intensity of the scattering amplitude [199]) of a spherical particle can be derived as:

$$SI(\theta, \varphi) = \frac{9}{4}[\sin^2\varphi(a_1 + b_1\cos\theta)^2 + \cos^2\varphi(a_1\cos\theta + b_1)^2]. \tag{4.2}$$

When there is no dipolar magnetic response (b_1=0), as for the case of a silver sphere in Fig. 4.2(b), the scattering intensity is

$$SI(\theta, \varphi) = \frac{9}{4}a_1^2(\sin^2\varphi + \cos^2\varphi\ \cos\theta^2), \tag{4.3}$$

and this indicates a typical scattering pattern of an electric dipole as shown in Fig. 4.2(c). However when there are equal dipolar electric and magnetic responses ($b_1 = a_1 = c$), as for the core-shell nanosphere shown in Fig. 4.2(d), the scattering intensity is simplified to:

$$SI(\theta) = \frac{9}{4}c^2(1 + \cos\theta)^2, \tag{4.4}$$

where the φ dependence is eliminated, indicating that the scattering is azimuthally symmetric as shown in Fig. 4.2(e). Also according to Eq. (4.4), the forward scattering intensity is $SI(0) = 9c^2$, which is enhanced and backward scattering intensity is $SI(\pi) = 0$, which is canceled. The enhancement and cancelation of the scattering originates from constructive and destructive interference of the electric and magnetic dipoles respectively.

Unidirectional scattering of an array of core-shell nanospheres

Up to now, we have demonstrated azimuthally symmetric unidirectional scattering using a single core-shell nanosphere [Eq. (4.4) and Fig. 4.2(e)]. To further enhance the directionality, we employ a one-dimensional chain of such particles with the chain axis parallel to the propagation direction of the incident plane wave [Fig. 4.3(a)], where the inter-particle distance is d. To characterize the directionality of the scattering, we define the main lobe beamwidth α as shown in Fig. 4.3(b), which corresponds to the full width at half maximum of the scattering intensity. To

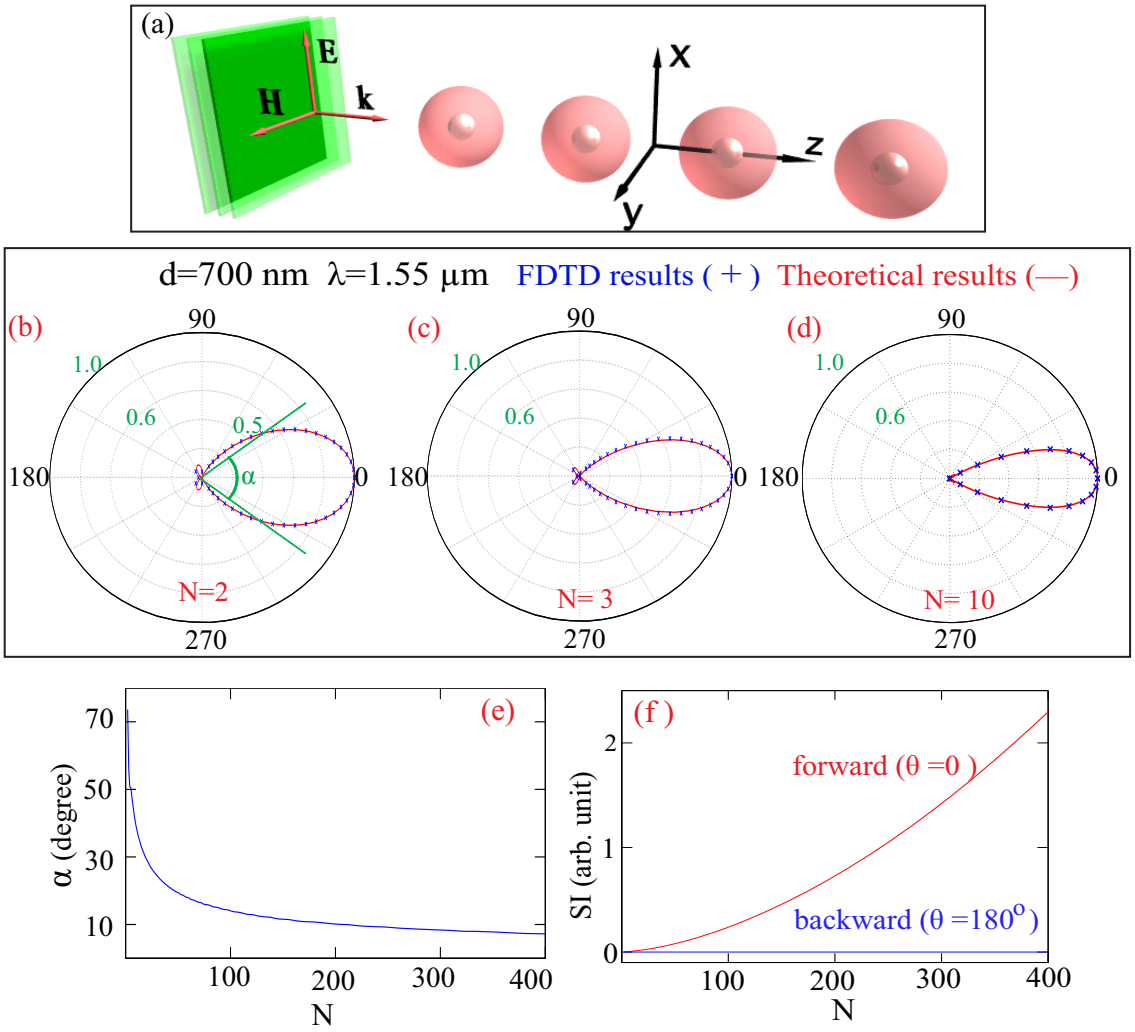

Figure 4.3: (a) A chain of core-shell nanospheres with inter-particle distance d. The chain axis is parallel to the propagation direction of the incident plane wave. (b)-(d) Theoretical (solid line) and FDTD (crosses) results of the scattering pattern (arbitrary scattering plane) by a chain of such particles with $N = 2, 3, 10$ particles, respectively. The wavelength is $\lambda = 1550$ nm and $d = 700$ nm. The main lobe beamwidth α is defined and shown in (b). (e) Main lobe beamwidth α and (f) forward and backward scattering intensity versus particle numbers in the chain. The parameters of a single nanosphere is the same as in Fig. 4.2.

investigate theoretically the scattering of the chain, each core-shell nanosphere is treated as a combination of orthogonal ED and MD with polarizabilities described by Eq. (4.1). The chain is comprised of N such particles and the i-th particle, located at the position of r_i, has an electric moment P_i and a magnetic moment M_i. According to the coupled dipole theory involving both electric and magnetic

dipoles [237, 238]:

$$\begin{aligned} P_i &= \alpha_1^e E_i^0 + \alpha_1^e \sum\nolimits_{j=1:N}^{j\neq i} (E_i^{P_j} + E_i^{M_j}) \\ M_i &= \alpha_1^m H_i^0 + \alpha_1^m \sum\nolimits_{j=1:N}^{j\neq i} (H_i^{P_j} + H_i^{M_j}) \end{aligned} \tag{4.5}$$

where E_i^0 and H_i^0 are the electric and magnetic fields of the incident wave at position r_i, respectively; $E_i^{P_j}$ and $H_i^{P_j}$ are electric and magnetic fields of radiation of P_j at r_i, respectively; $E_i^{M_j}$ and $H_i^{M_j}$ are the fields of radiation of M_j at r_i. By solving Eq. (4.5), both the electric and magnetic moments of each particle can be obtained and then the scattering pattern can be achieved as the superposition of the radiations of all the $2N$ interacting dipolar moments.

The symmetry of Maxwell's equations guarantees that in Eq. (4.5) P_i and $-M_i$, E_i and $-H_i$ are exchangeable when $\alpha_1^e = \alpha_1^m$. This means that each particle in the chain will have electric and magnetic moments of the same strength, thus leading to unidirectional scattering, similar to an isolated core-shell nanosphere. Considering also the azimuthal symmetry of the structure, the whole chain will scatter light unidirectionally independent on azimuthal angle. In Fig. 4.3(b)-(d) we show the scattering patterns at arbitrary scattering planes by a chain with particle number $N = 2, 3, 10$, according to Eq. (4.5). The operating wavelength is $\lambda = 1550$ nm, which is approximately the resonant wavelength of a single core-shell nanosphere [Fig. 4.2(d)], and the inter-particle distance is fixed at $d = 700$ nm. It is clear from Fig. 4.3(b)-(d) that by increasing the number of particles, the main lobe beamwidth will decrease, indicating a better directionality.

The dependence of α on the particle number is shown in Fig. 4.3(e) for N up to 400. In Fig. 4.3(f) we also show the scattering intensity in forward and backward directions for different number of particles in the chain. These dependencies confirm that the vanishing backward scattering feature is robust with increased particle number N and the forward scattering is enhanced for larger N. To verify the theoretical results, we also perform three dimensional finite-difference time-domain simulations of the chains, with the results shown in Fig. 4.3(b)-(d) (crosses). The simulations have been carried out using the commercial software Lumerical FDTD Solutions (http://www.lumerical.com/). The experimental data [235] is assigned for the permittivity of silver and the permittivity of the dielectric shell is $n = 3.4$. A total-field scattered-field plane wave source, and six two-dimensional frequency-domain field monitors are used to calculate the far-field scattering pattern directly. In simulations perfectly matched layer (PML) boundary condition is used for all the six boundaries and we decrease the mesh size until the results are convergent.

It is seen that the FDTD results agree well with the theoretical predictions, justifying the claim of azimuthally symmetric unidirectional scattering with enhanced directionality. Note here, that we do not use forward-backward ratio to characterize the scattering, which is impractical in our case, as this ratio is practically infinite even for very few core-shell nanosphere as shown in Fig. 4.3(b)-(d). We note here that the mechanism of the directionality enhancement by the nanosphere array is basically the same as that of Yagi-Uda antennas, where the interferences plays a

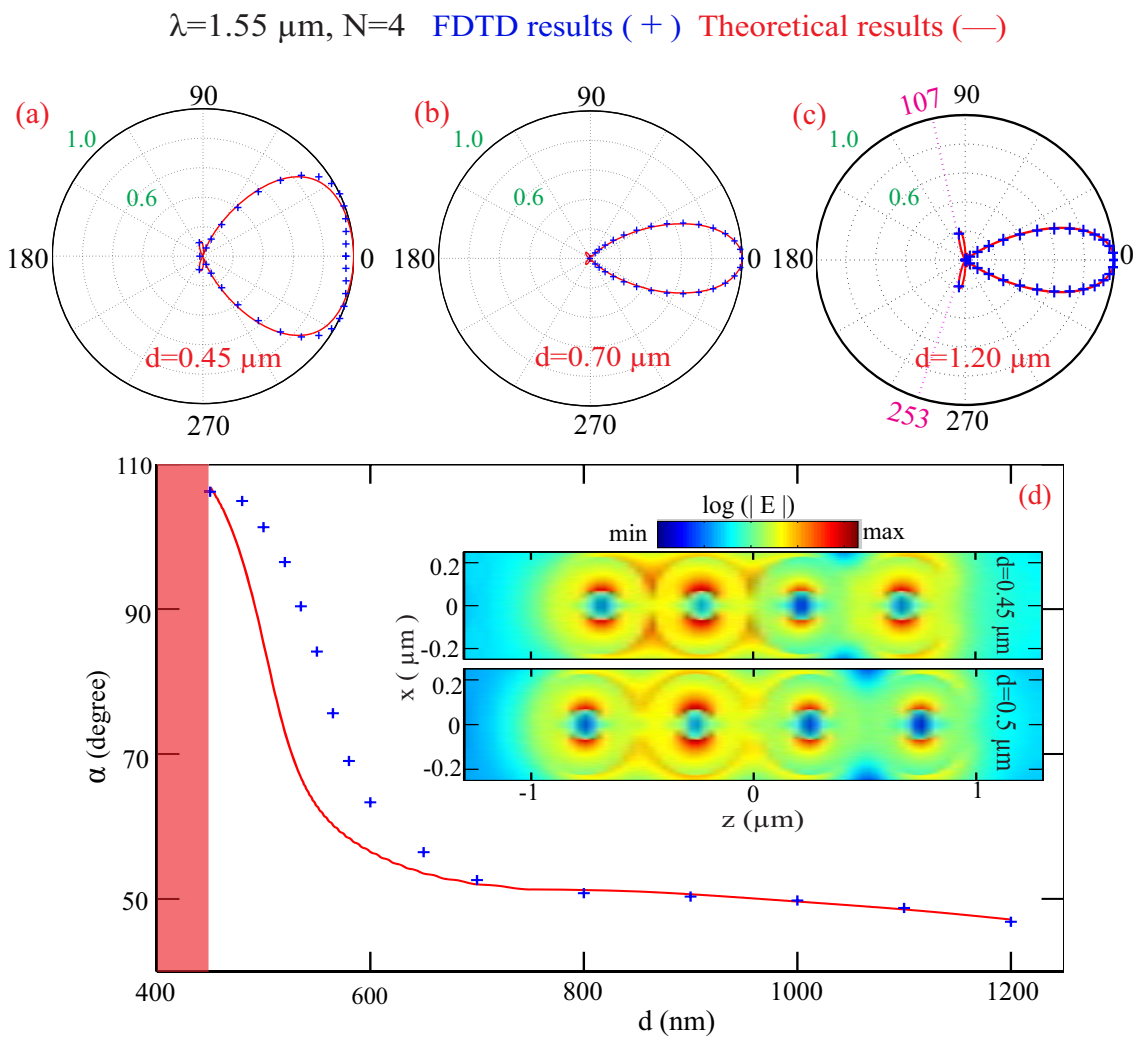

Figure 4.4: (a)-(c) Theoretical (solid line) and FDTD (crosses) results of the scattering pattern (arbitrary scattering plane) by a chain of core-shell nanospheres with $N = 4$ and $d = 450$ nm (touching particles), 700 nm, and 1200 nm, respectively. Two diffraction angles of 107° and 253° are indicated in (c). (d) Theoretical and FDTD results of α versus d. Inset: Near electric field distributions for two inter-particle distance (top) $d = 450$ nm and (bottom) 500 nm respectively. The parameters of a single particle is the same as in Fig. 4.2(d) and $\lambda = 1550$ nm.

major role [58, 208]. However, in contrast to the conventional Yagi-Uda antennas, in our structures the backward scattering is suppressed automatically based on the special feature of each nanosphere, without the need of extra reflectors to reflect the backward radiation.

As a next step, we investigate the dependence of the scattering by the chain on the inter-particle distance d. We fix $N = 4$ and $\lambda = 1.55$ μm. In Fig. 4.4(a)-(c) we show both the theoretical (solid line) and FDTD (crosses) results of the scattering patterns for three inter-particle distances: $d = 450$ nm (touching particles), 700 nm, and 1200 nm, respectively. Figure 4.4(d) shows the dependence of α on d for the

range of 450 nm to 1200 nm (both FDTD and theoretical results are shown). It is clear that when $d > 650$ nm, the theoretical results are in excellent agreement with the FDTD simulations, indicating the validity of the mixed dipole approximation. In the regime of $d < 650$ nm, the theoretical results agrees only qualitatively with the FDTD simulations, showing accurately the trend that with decreasing d, α increases, displaying worse directionality. The discrepancies come from the dipole approximation of spherical particles [Eq. (4.1)], which is based on the far-field scattering effect [199, 233], while the near-field features of spherical particles can not be fully captured by the dipole approximation. Viewing the core-shell nanosphere as combined dipoles will reflect the coupling with high accuracy when they are well separated ($d > 650$ nm). However when the particles are closer to each other and the near-field coupling is more pronounced, the dipole approximation can only qualitatively approximate the stronger near-field coupling and thus larger α and worse directionality. In Fig. 4.4(d-inset) we show the near-field distributions (electric field) for four core-shell nanospheres with two inter-particle distances, which show clearly stronger near-field coupling for smaller d. We emphasize that even for touching particles [Fig. 4.4(d)(top inset)], the dipole moments are still dominant. This is because within each core-shell nanosphere, the electric dipole is a result of a surface plasmon mode, with the fields confined at the interface of core and shell, while the magnetic dipole is a result of a cavity type mode in the high permittivity shell [199, 226], with most of the fields confined within the shell. Thus, the fields outside the core-shell particle and thus the induced coupling are relatively small. Therefore the dipole moments remain dominant irrespective of inter-particle distances [Fig. 4.4(d-inset)]. At the same time due to the symmetry of Eq. (4.5), the dominant electric and magnetic dipole moments of each particle have the same strength and this guarantees that the features of azimuthally symmetric and vanishing backward scattering are robust against different inter-particle distances [Fig. 4.4(a)-(d)], which are preserved even for touching particles [Fig. 4.4(a)].

According to Fig. 4.4(d), there is a clear trend that smaller distance d will lead to worse directionality and larger distance d can enhance the directionality. This feature can be intuitively understood simply through considering the far field interference of the nanospheres in the array. The phase delay between adjacent nanosphere is $\Delta\Phi = kd(1 - \cos\theta)$, which indicates that in the forward direction $\theta = 0$ all dipoles interfere constructively. As such, the scattering intensity is always strongest in the forward direction [Fig. 4.3(b-d)]. At the same time, better directionality means destructive interference for smaller θ, which requires larger d to produce sufficient phase delay. Here we also emphasize the tradeoff between the energy confinement and directionality for the chains with different d. Although larger d will lead to better directionality (Fig. 4.4), when $d > \lambda/2$, the phase delay between adjacent nanospheres will be sufficient to support collective grating diffractions, leading to significant energy leakage into other directions [Fig. 4.4(c)]. The angle of the first diffraction order is $\beta = \arccos(1 - \lambda/d)$, which corresponds to 107° and 253° when $d = 1200$ nm and $\lambda = 1550$ nm. As shown in Fig. 4.4(c), there is significant energy leakage into both of these directions due to the grating effect. On the other hand for smaller d, although there will be worse directionality (Fig. 4.4),

light would be better confined (less leakage to other channels) as a larger proportion of the Brillouin zone is located above the light line [239].

Broadband unidirectional scattering of core-shell nanospheres

A key feature of the scattering properties of the core-shell nanospheres is their relatively broadband spectral response. From 4.2(d) one can clearly see that there is a wide spectral region where a_1 and b_1 spectrally overlap. According to Eq. (4.4), azimuthally symmetric unidirectional scattering can be achieved when a_1 and b_1 coincide and, thus, the main features should be preserved in the entire overlapping spectral region. To obtain the spectral response of the scattering we fix the number of particles to $N = 4$ and the distance between them to $d = 700$ nm. In Fig. 4.5 we show the scattering patterns of the chain under plane wave illumination for three different wavelengths in the range 1.51 μm to 1.65 μm, covering the entire C and L-bands that are dominantly used in optical fiber telecommunications [240]. Both s (solid line) and p (circles) polarization scattering patterns are shown, demonstrating a 140 nm bandwidth of the unidirectional scattering. For wavelengths outside this spectral region, a_1 and b_1 are significantly different [Fig. 4.2(d)] and thus both the azimuthal symmetry and the vanishing backward scattering will be lost according to Eq. (4.4). We emphasize here that we call the response broadband in a relative sense because: (i) both electric and magnetic dipolar resonances overlap spectrally over a range that is as broad as the individual resonances [Fig. 4.2(d)], over which the unidirectionally scattering can be achieved. If the two resonances are not tuned to coincide spectrally and are effectively separated, the bandwidth of the unidirectional scattering will also be reduced and can be quite narrow compared to what we have achieved in this work; (ii) the achieved spectral regime covers the entire C band and L band that are primarily used in optical fiber communications [240].

We note that azimuthally symmetric unidirectional scattering can be achieved for any system that support dominantly electric and magnetic dipolar resonances that coincide spectrally with the same strength. For example, within a single high permittivity sphere, both ED and MD resonances can be supported dominantly and be of approximately the same strength at a specific wavelength regime [225]. The problem is that for such a sphere, the resonant wavelengths of electric and magnetic dipoles are separated, with the overlapping point far from either resonance. Therefore although unidirectional scattering can be achieved for a dielectric sphere, the scattering is off-resonant and generally weak. Also it is expected that in this case the operating wavelength range of unidirectional scattering will be narrow and the structure will have high frequency selectivity.

Conclusion

In conclusion, we have studied the scattering properties of (metal) core - (dielectric) shell nanospheres and have shown that they exhibit azimuthally symmetric unidirectional scattering. This unidirectional scattering originates from the interference of electric and magnetic dipolar resonances that coexist with the same strength

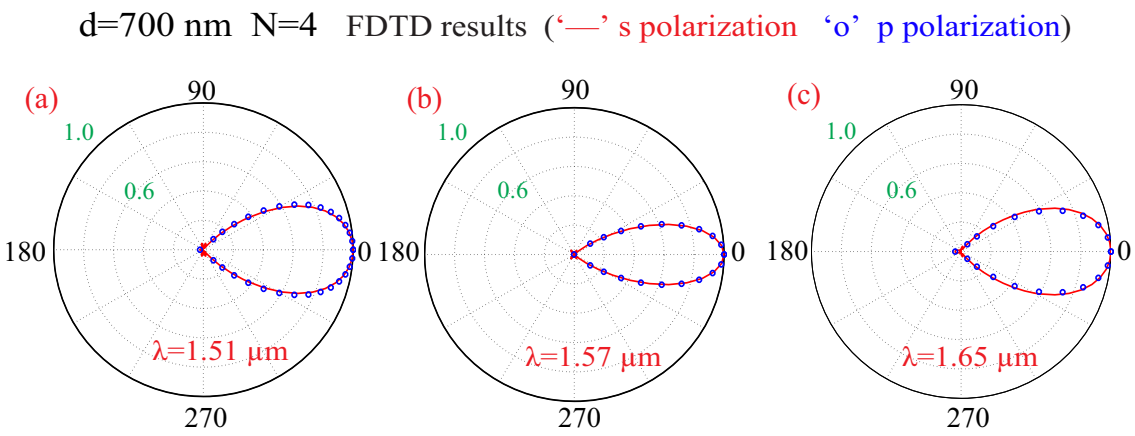

Figure 4.5: FDTD results of the scattering pattern of a chain of four core-shell nanospheres with $d = 700$ nm for three operating wavelengths of 1.51 μm, 1.57 μm, and 1.65 μm. Both s (solid line) and p (circles) polarization scattering patterns are shown. The parameters of a single core-shell nanosphere is the same as in Fig. 4.2(d).

within the particle itself. We have further shown that the directionality of a single core-shell nanosphere scattering can be enhanced when the nanospheres are arranged in a one-dimensional chain. For such a chain, there is a tradeoff between energy confinement and directionality for different inter-particle distances, however the features of vanishing backward scattering and azimuthal symmetry are always preserved, irrespective of the inter-particle distances, even when the particles touch each other. We also show that the operating wavelength range for unidirectional scattering of the chain is widely broadband, spanning over a bandwidth of 140 nm.

It is worth mentioning that the described features are valid under excitation of broad Gaussian beam (compared to the cross sections of the scatter) [199], which provides a feasible path to experimental observation of the predicted effects. For experimental realization, the fabrication of particles with metal-core and high-index dielectric shell is of key importance. Chemically synthesis of core-shell nanosphere is well suited for practical realizations [241], with numerous examples where metal-core with a shell of high-index oxides such as TiO_2 or ZrO_2 can be routinely synthesized [242]. At the same time, for shells made of materials with refractive index higher than 3, such as high-index semiconductors, one would probably need to resort on bottom-up approached, including double inversion with silicon deposition. Indeed, high index silicon shells have already been developed and used for low-Q whispering gallery mode cavities [243]. Similar shells might well be applicable for the fabrication of core-shell nanosphere considered in this work.

We note that the operating wavelength range of the core-shell nanosphere is highly tunable by changing the core-shell aspect ratios and the permittivity of the dielectric shell. Furthermore, there is extra freedom for resonance tuning if anisotropic materials are involved [244–246]. For the nanospheres studied here, at the resonant wavelength of $\lambda = 1550$ nm, the total scattering efficiency is approximately 14 and the absorption efficiency is approximately 0.3. The ratio is close to 50, which means that a very small proportion of the total energy is transferred

into heat rather than radiated. For operating wavelength where the loss of metal is higher or/and the loss of the dielectric shell is significant, the absorption efficiency will be higher. Loss can also change the position and strength of the resonances of the particles. However as long as the two resonances can be tuned to coincide spectrally with the same strength, the azimuthally symmetric unidirectional scattering could be achieved. Most importantly all our results can be extended to other particle geometries (rather than spheres) that support orthogonal electric and magnetic resonance pairs. We envisage that our findings on reflection suppression and broadband unidirectional scattering by superimposing electric and magnetic responses will be of great importance in various fields, especially in the flourishing fields of nanoantennas, photovoltaic devices and nanoscale lasers that require reflection suppression.

4.2.2 Scattering pattern engineering for magneto-electric core-shell nanowires

In this section we extend the study of 3D nanospheres to 2D core (metal)-shell (high permittivity dielectric shell) nanowires. we study the scattering of (metal) core-(high permittivity dielectric) shell nanowires, which support both electric and magnetic resonances. We find that for p-polarized incident waves, the ED and MD can be tuned to overlap spectrally. As the ED corresponds to two degenerate scattering channels while the MD corresponds to only one channel, its magnitude is twice the magnitude of the MD. Consequently, in sharp contrast to spherical structures investigated before, where the scattering is suppressed only at the backward direction, here we demonstrate a pair of angles along which the scattering is vanishing. It is also demonstrated that the scattering features are highly polarization dependent, and the vanishing scattering angles can also be obtained through the Fano resonance, which is induced by the interference of the broad MD and the narrow higher order electric modes.

Scattering pattern of core-shell nanowires

The structure we study is shown schematically in Fig. 4.6. The infinitely long nanowire is arranged along z direction with a silver core (the permittivity is from Ref. [235]) and a dielectric shell ($n = 3.5$). Here the incident plane wave propagates along x direction and the scattered light is confined at the $x - y$ plane. The electric field of the incident wave is either polarized along y (p-wave) or along z (s-wave). The scattering of a nanowire (single-layered or multi-layered) can be solved analytically and the scattering efficiency is [199, 247]:

$$Q_{sca}^{s,p} = \frac{2}{kr}\left[(a_0^{s,p})^2 + 2\sum\nolimits_{m=1}^{\infty}(a_m^{s,p})^2\right], \tag{4.6}$$

where k is the angular wave-number in the background material (vacuum in this study); r is the radius of the outmost layer; a_0 and a_m are the scattering coefficients, and the superscripts s and p corresponds to s-wave and p-wave, respectively. More

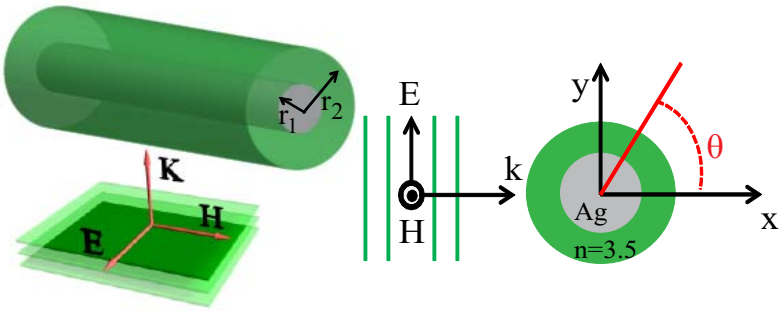

Figure 4.6: Schematic of scattering of normally incident p-polarized plane waves by a core-shell nanowire. The core nanowire is silver of radius r_1 and the shell is $n = 3.5$ dielectric of radius r_2. The scattering angle is defined as θ.

specifically a_0 and a_1 correspond to the magnetic (electric) and electric (magnetic) dipoles for p (s) waves, respectively [224]. The scattering coefficient a_m relates to an angular field distribution of $e^{\mathrm{im}\theta}$ [224], which corresponds to two angular momentum channels with angular momentums $\pm m\hbar$, where the scattering angle θ is defined in Fig. 4.6. In contrast a_0 corresponds to a uniform angular field distribution with no angular momentum along z direction [199, 247]. As a result, the contribution from a_m to the scattering efficiency is twice that from a_0. At the same time the angular scattering amplitude can be expressed as [199, 247]:

$$SA^{s,p}(\theta) = \sqrt{2/\pi k}\left|a_0^{s,p} + 2\sum\nolimits_{m=1}^{\infty} a_m^{s,p}\cos(m\theta)\right|. \tag{4.7}$$

In Fig. 4.7 we show the scattering efficiency spectra (SES) for incident p-wave, including the total scattering efficiency and the contributions from a_0^p (MD) and a_1^p (single channel, ED). Firstly we study a single-layered nanowire ($r_1 = 0$, $r_2 = 145$ nm) and the SES is shown in Fig. 4.7(a). It is clear that although both dominant ED and MD are supported with resonances centered at point E and M, respectively, they are spectrally separated. Above Fig. 4.7(a) we also show the near-field distributions of longitudinal magnetic field intensity ($|H_z|^2$,colourmap) and transverse electric field (E_t, arrows) of points E and M. Dashed green lines indicate the nanowire-background boundaries. It is clear that ED and MD are supported at points E and M respectively: at point E, the H_z field shows a typical dipolar distribution with transverse electric filed almost linearly polarized; at point M, H_z field is almost azimuthally symmetric inside the nanowire, accompanied by circulating displacement currents, indicating the existence of an artificial magnetic dipole [206, 225–228]. Fig. 4.7(c) shows the scattering patterns at both points. Typical dipole-like scattering patterns are observed: at point E the ED is dominant and oriented along y direction with a two-lobe scattering pattern in the $x-y$ plane; at point M the MD is dominant and oriented along z direction with an almost circular scattering pattern in the $x-y$ plane. Then we study a two-layered core-shell nanowire, shown in Fig. 4.6. As shown in Fig. 4.7(b) it is clear that when the inner radius $r_1 = 70$ nm and the outer radius $r_2 = 145$ nm, the ED and MD can overlap and thus creating a superscattering spectral regime (the corresponding

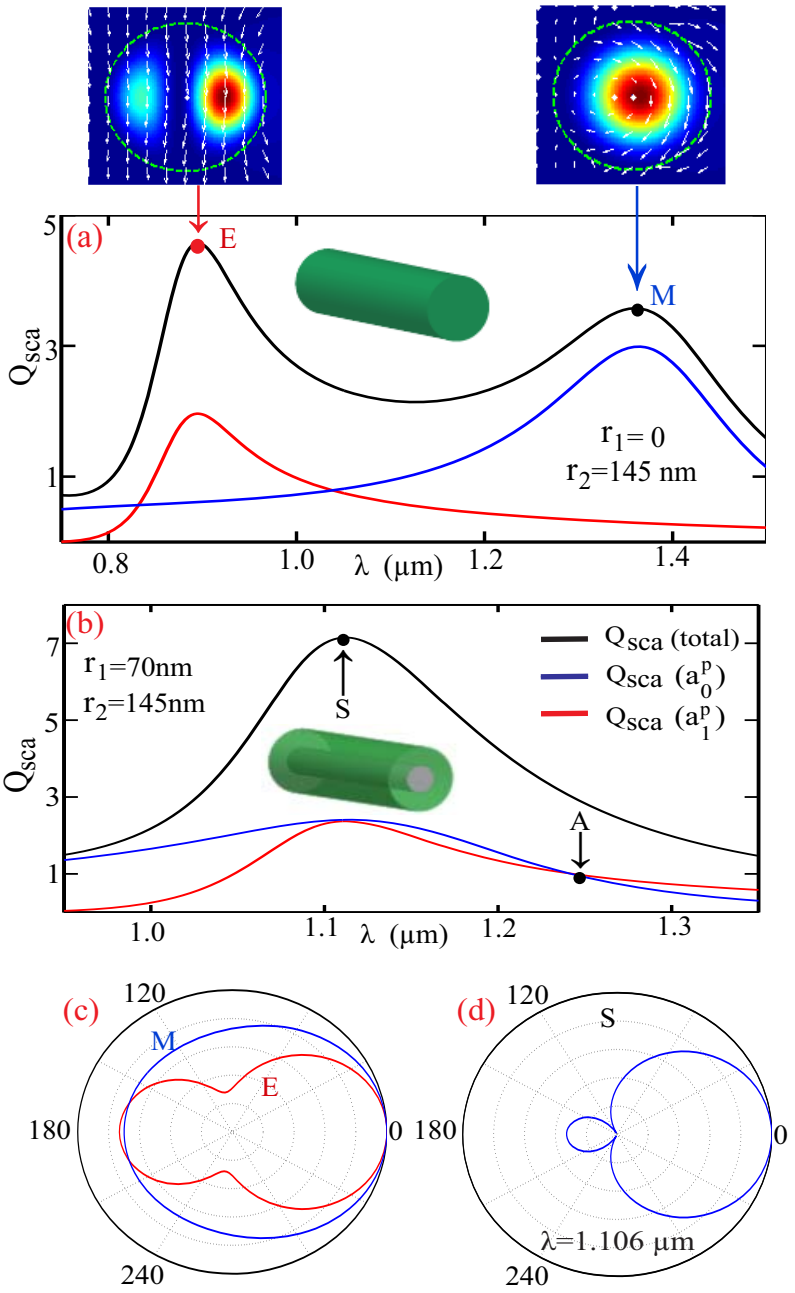

Figure 4.7: Scattering efficiency spectra of p-wave (total and the contribution from a_0^p and a_1^p) for (a) uniform dielectric nanowire with $r_1 = 0$, $r_2 = 145$ nm and (b) (silver) core - ($n = 3.5$ dielectric) shell nanowire with $r_1 = 70$ nm and $r_2 = 145$ nm. Above (a) the near-field distributions of $|H_z|^2$ (colourmap) and transverse electric field E_t (arrows) at points E and M are shown. Dashed green lines indicate the nanowire background boundaries. (c) and (d) show the scattering patterns for the points indicated in (a) and (b): $\lambda_S = 1.106$ μm, $\lambda_A = 1.242$ μm, $\lambda_E = 0.895$ μm, and $\lambda_M = 1.363$ μm.

single channel limit in terms of scattering efficiency is approximately 2.4) [25]. We

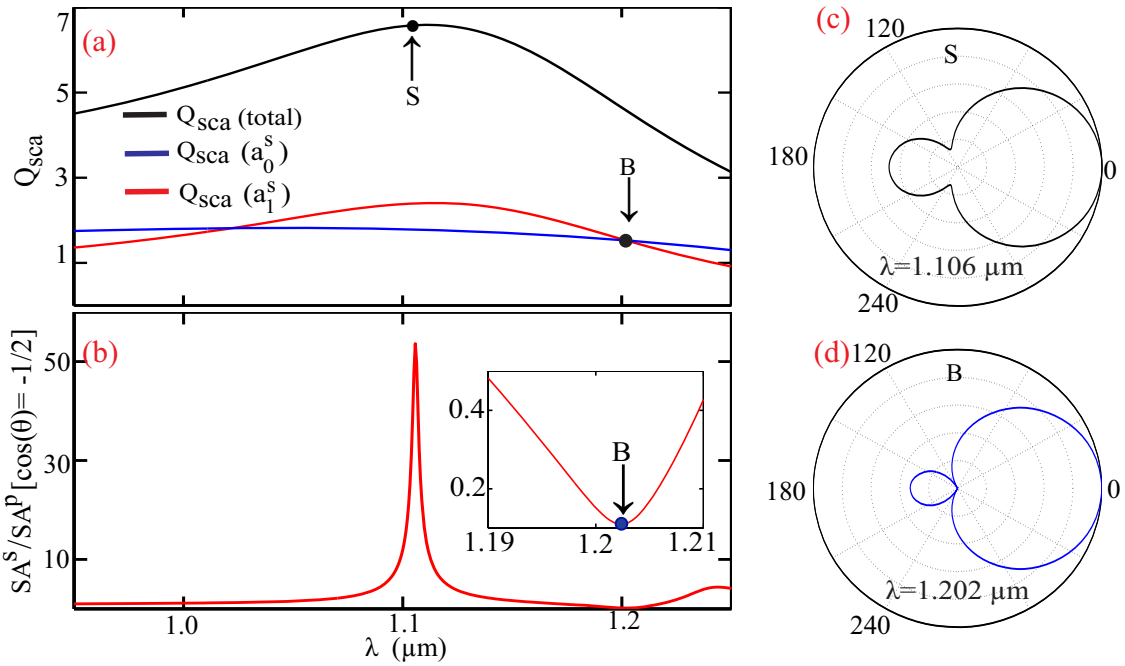

Figure 4.8: Same as in Fig. 4.7(b) but for incident s-wave. (b) The ratio of SA^s/SA^p with equal p-wave and s-wave incidence along $\theta = 120°$ and $240°$. The inset shows an enlarged area of $\lambda = 1.190 - 1.210$ μm. (c) and (d) show the scattering patterns for the points indicated in (a) and (b) with $\lambda_B = 1.202$ μm and $\lambda_S = 1.106$ μm.

note here that the overlapping wavelength of ED and MD for such structures is highly tunable, and can be shifted to shorter or longer wavelengths for smaller or larger scales of the nanowires with specific aspect ratios. Also in the spectral regime in Fig. 4.7(b), the ED and MD are dominant and Eq. (4.7) can be simplified as:

$$SA^p(\theta) = \sqrt{2/\pi k}|a_0^p + 2a_1^p \cos(\theta)|. \tag{4.8}$$

At the overlapping resonant point S, as indicated in Fig. 4.7(b), both a_0^p and a_1^p are real [247] and $a_0^p = a_1^p = b$. Thus at this point we have $SA^p(\theta) = b\sqrt{2/\pi k}|1 + 2\cos(\theta)|$, which indicates that when $\theta = 120°,\ 240°$ $[\cos(\theta) = -1/2]$ the scattering is vanishing. In Fig. 4.7(d) we show the normalized scattering amplitude at point S. We note that at point A indicated in Fig. 4.7(b), the scattering pattern is identical as that of point S. The difference is that point A is in the non-resonant regime and the overall scattering is less than half of that at point S.

Polarization dependence of the scattering of the core-shell nanowires

Next we change the incident wave to s-wave and show the SES for the core-shell nanostructure in Fig. 4.8(a). In contrast to p-wave incidence, at the point S, $|a_0^s| \neq |a_1^s|$. Thus the scattering at the vanishing scattering angles of the p-wave can not be neglected, as demonstrated in Fig. 4.8(c). This feature is similar to the reflection at the Brewster angle, which is highly polarization dependent. In Fig. 4.8(b) we show the amplitude ratio of $SA^s/SA^p[\cos(\theta) = -1/2]$ with equal

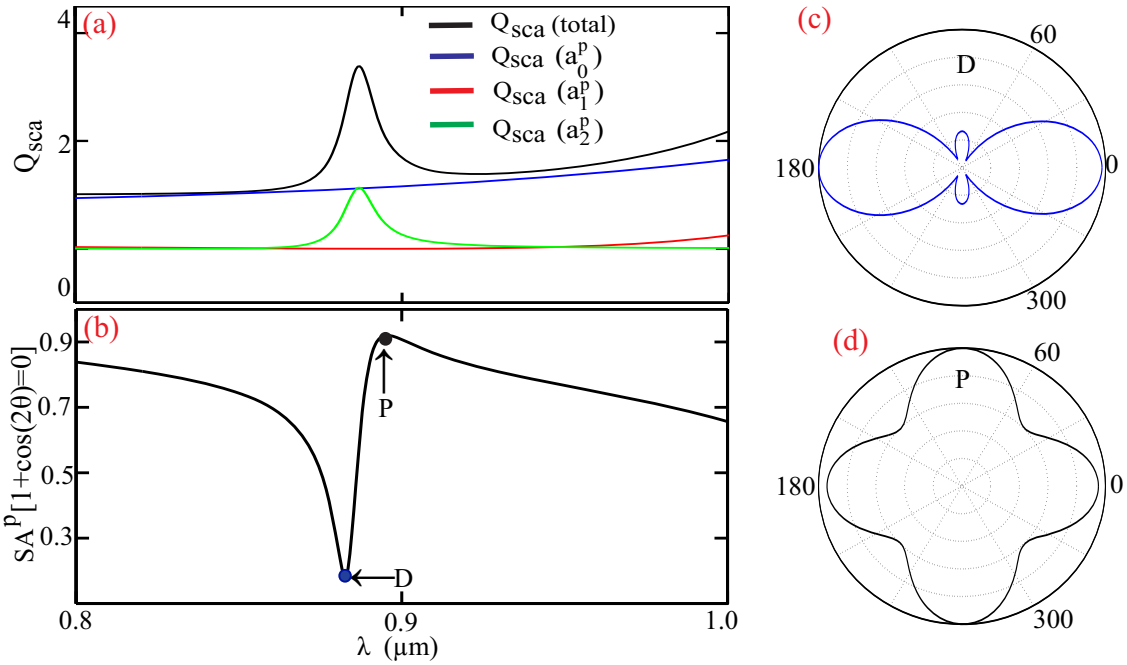

Figure 4.9: (a) Same as in Fig. 4.7(b) but in the spectral regime of $\lambda = 0.8 - 1$ μm. (b) normalized scattering amplitude along $\theta =$ 60°, 120°, 240° and 300°. (c) and (d) show the scattering patterns for the points indicated in (b) with $\lambda_D = 0.883$ μm and $\lambda_P = 0.895$ μm.

p-wave and s-wave incidence. There is a sharp peak centered at point S where the p-wave scattering is negligible [Fig. 4.7(d)] compared to that of the s-wave incidence along $\theta = 120°$ and 240° (the maximum intensity ratio can reach approximately 3500). At the same time, the width of such response is as narrow as 5 nm, indicating that it might be used for efficient polarization splitter and filters. We also note that there is a dip located at point B [inset of Fig. 4.8(b)], where the scattering of s-wave incidence along $\theta = 120°$ and 240° is vanishing [Fig. 4.8(d)].

Fano resonance induced scattering shaping of the core-shell nanowires

Finally, we study the interference of MD and the electric quadruple mode (QM, characterized by a_2) for p-wave. In Fig. 4.9(a) we show the SES for the same core-shell structure at the spectral range of 800-1000 nm. The contribution from QM and MD are dominant and then Eq. (4.7) can be expressed as:

$$SA^p(\theta) = \sqrt{2/\pi k}|a_0^p + 2a_2^p \cos(2\theta)|. \tag{4.9}$$

Compared to the QM, the MD response is rather broad, and its interference with the narrow QM will produce sharp Fano resonances [248–250]. In Fig. 4.9(b) we show the normalized scattering amplitude when $1 + \cos(2\theta) = 0$, and the two modes can almost cancel each other, resulting in vanishing scattering along two pairs of angles: $\theta = 60°$, 120°, 240° and 300°. Typical Fano asymmetric line-shape is observed. The specific scattering patters for the Fano dip (point D) and Fano peak (point P) are

shown in Fig. 4.9(c) and Fig. 4.9(d), respectively, showing clearly the destructive and constructive interferences along those angles.

Conclusion

In summary, we have studied scattering of core-shell nanowires, which support both electric and magnetic resonances. We have demonstrated how to achieve a pair of vanishing scattering angles in the superscattering regime of overlapped ED and MD for p-waves. We have also demonstrated the polarization dependence of these scattering features and Fano resonance induced vanishing scattering angles. Our study generalizes the proposal of Kerker for backward scattering suppression, and our approaches can be extended to higher order modes or to other non-cylindrical structures where different vanishing scattering angles can be obtained in the resonant strong-scattering regimes. Our results shed new light on the direction of scattering shaping based on interferences of both electric and magnetic resonances, which can play a major role in applications such as nanoantennas, nanolasers, sensors, solar cells and so on.

4.3 Fano resonance in arrays of core-shell nanospheres

4.3.1 Fano resonance in nanostructures

Fano resonance is characterized by a distinct asymmetric line-shape, which originates from an interference of a broad spectral line background state and a narrow discrete state [248, 249, 251]. As an ubiquitous wave inference phenomenon, the applications of Fano resonance spread rapidly from atomic physics, where it was first investigated systematically [251], to many other fields including nuclear physics, condensed matter physics, and classical optics [248, 249, 251]. Recently in the emerging fields of plasmonics and metamaterials, Fano resonance is attracting surging interest due to its observations and applications in different settings, such as individual asymmetric plasmonic structures [252], periodic plasmonic structures [253–256], plasmonic clusters [257] and metamaterials [258]. In Fig. 4.10 we show some basic information about Fano resonance. Firstly compared to the Lorentzian resonance which corresponds to a fundamental symmetric line-shape, Fano resonance is characterized by an asymmetric line-shape, with a Fano dip and a Fano peak. The Fano resonance can be viewed as a hybrid state coming from the interference of a discrete state with the continuum or a broad state: the destructive interference will leads to the Fano dip while the constructive interference leads to the Fano dip.

The Fano resonances studied up to now usually involve the interference of only two modes - with a spectrally broad background and a narrow resonant one. In photonic structures, for different polarizations of the incident waves, only modes of specific orientations can be excited and, thus, the overlapping and coupling between those modes are highly polarization dependent. As a consequence, the Fano resonance achieved in such structures, which comes directly from the coupling of modes, also inevitably show strong polarization dependence [202, 259, 260]. For

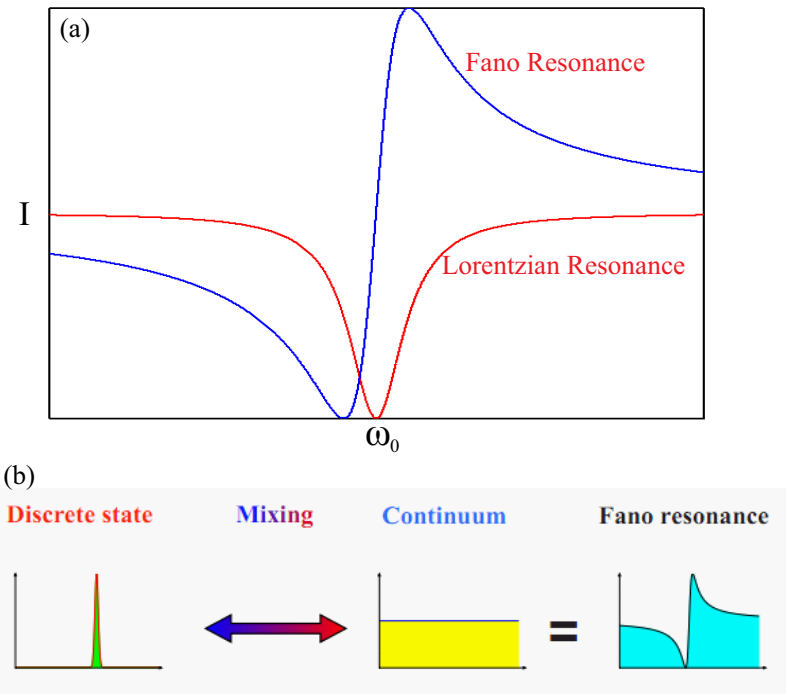

Figure 4.10: (a) Symmetric line-shape of Lorentzian resonance and asymmetric line-shape of Fano resonance. (b) Schematic illustration of the origin of Fano resonance: the interference of a discrete state with the continuum (or broad state).

many applications based on the Fano resonances, *e.g.* sensing [53, 54], nonlinear switching [259, 261], lasing [78] and so on, polarization independent Fano resonances are highly desirable, but has not been demonstrated yet.

4.3.2 Polarization independent Fano resonance in arrays of core-shell nanospheres

In this section, in contrast to the conventional approach, we employ the interference of three modes rather than two to achieve polarization independent Fano resonances in periodic structures. We demonstrate that such Fano resonances can be excited in arrays of various configurations of (metal) core - (dielectric) shell nanospheres. We find particular parameters of a single particle, which allow to support simultaneously a pair of orthogonal ED and optically-induced MD, which spectrally overlap and are of the same strength [229, 233]. These two resonant modes can interfere simultaneously with the geometric resonance (coherent collective response, also termed as Wood's anomaly [262–265]) of the periodic array through diffractive coupling, producing polarization independent Fano resonances, despite the fact that such periodic structures do not possess azimuthal symmetry. We further show that with different polarizations, the ED and the MD can be selectively controlled, thus opening new opportunities for near-field manipulations, which may find applications in sensing, lasing and nonlinear switching in plasmonic nanostructures and metamaterials.

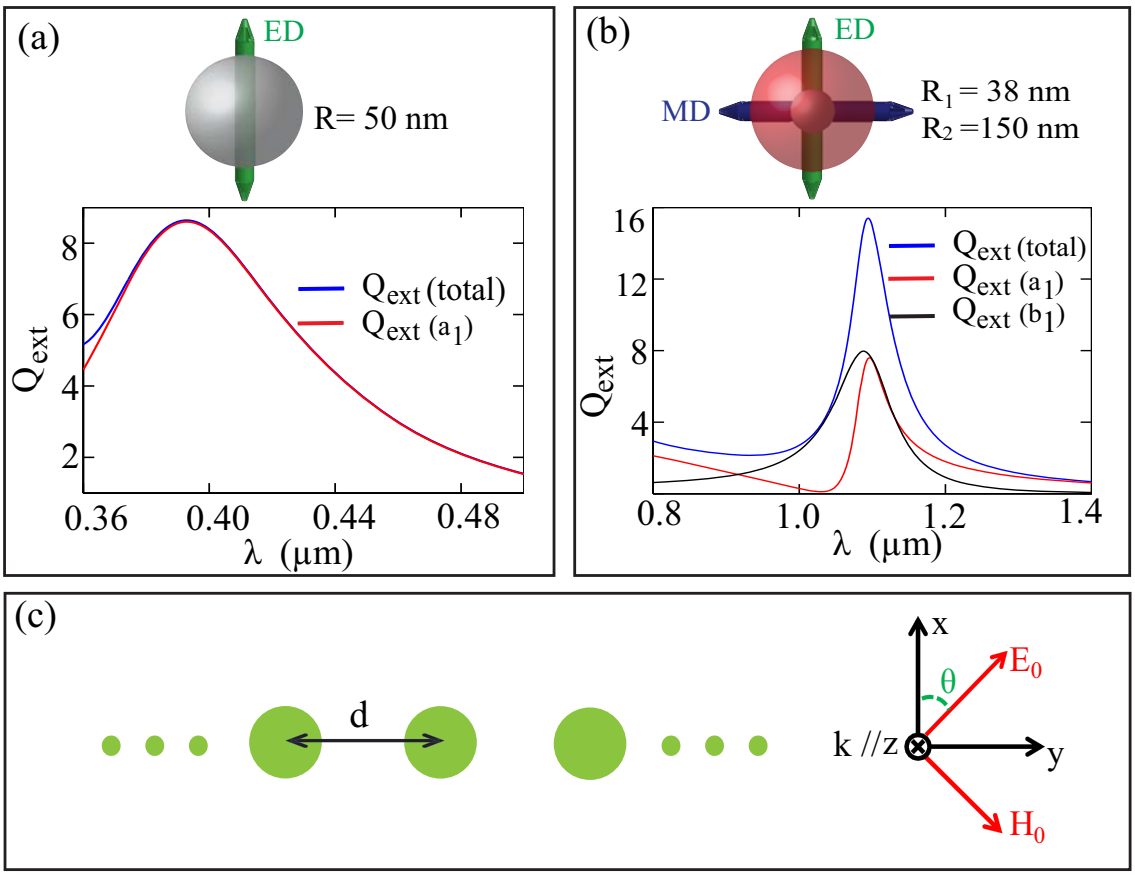

Figure 4.11: Extinction efficiency spectra for (a) silver sphere of radius 50 nm and (b) core-shell nanosphere (silver core and dielectric shell of $n = 3.5$) with inner radius 38 nm and outer radius 150 nm. The silver sphere can be viewed as an ED [top of (a)] and the core-shell nanosphere can be approximated as a pair of orthogonal ED and MD, which coincide spectrally with the same strength [top of (b)]. (c) Schematic geometry of the 1D structure under consideration. The unit cell particle could be either a silver sphere or core-shell nanosphere. The incident plane wave is propagating along z and the polarization angle (electric field with respect to x direction) is θ.

Polarization independent Fano resonance in the 1D arrays of core-shell nanospheres

The scattering of a spherical particle (single- or multi-layered) can be solved analytically using Mie theory [199]. For an incident plane wave illumination, the extinction efficiency can be expressed as [199]:

$$Q_{ext} = \frac{2}{k^2 R^2} \sum_{n=1}^{\infty} (2n+1)\mathrm{Re}(a_n + b_n), \tag{4.10}$$

where k is the angular wave number in the background material (it is vacuum in our study); a_n and b_n are Mie scattering coefficients, which correspond to electric and magnetic moments respectively [199]; R is the radius of outmost layer and Re means the real part. In the case of scattering by a small size particle the excitations

of higher order modes can be neglected [$a_n \ll 1, b_n \ll 1$ ($n > 1$)]. As such only the ED (a_1) and the MD (b_1) moments contribute to the overall extinction efficiency:

$$Q_{ext} = \frac{6}{k^2 R^2} \mathrm{Re}(a_1 + b_1). \tag{4.11}$$

In Fig. 4.11(a) we show the extinction efficiency spectra (both total and the contribution from a_1) of a silver sphere of $R = 50$ nm [on top of Fig. 4.11(a)] illuminated by a plane wave. For the permittivity of silver we use the experimental data from Ref. [235]. It is clear that a_1 contribute dominantly to Q_{ext} in the spectral range shown and thus the sphere could be effectively approximated as an ED. Figure 4.11(b) shows the extinction efficiency for a core-shell nanosphere with a silver core of a radius $R_1 = 38$ nm and a dielectric shell of refractive index $n = 3.5$ with an outer radius $R_2 = 150$ nm [top of Fig. 4.11(b)]. According to Fig. 4.11(b), only a_1 and b_1 dominantly contribute to Q_{ext} in the spectral regime of 1100 nm-1180 nm, therefore the core-shell nanosphere can be viewed as a pair of orthogonal ED and MD coinciding spectrally with the same strength. The ED and the MD are orthogonal and not coupled to each other due to the high symmetry of the core-shell structure [236].

We first investigate 1D periodic structures as shown in Fig. 4.11(c). For comparison, the unit cell particle can be either a silver sphere shown in Fig. 4.11(a) or a core-shell nanosphere shown in Fig. 4.11(b), with inter-particle distance d. The incident plane wave is propagating perpendicular to the array axis (along z direction) and the polarization angle is θ, which is the angle between electric field and x direction. Here we fix the wavenumber k of the incident plane wave perpendicular to the array axis as shown in shown in Fig. 4.11(c), which is the case of the strongest Fano resonance [254]. when the direction of k deviates from the normal of the array axis, the Fano resonance will split into several resonances with reduced strengths [254].

For spherical particles with only dipole resonances, the effective electric and magnetic polarizabilities are given by Eq. (4.1). For an ensemble of such spherical particles with particle number N, let us suppose that the i-th particle located at the position $\mathbf{r}_i$ has an electric moment $\mathbf{P}_i$ and magnetic moment $\mathbf{M}_i$. According to the coupled dipole approximation (CDA) with the presence of both ED and MD shown in Eq. (4.5), the electric and magnetic moments of each particle in the ensemble ($\mathbf{P}_i$ and $\mathbf{M}_i$) can be obtained. Then, the extinction efficiency of the ensemble can be found by combining all the contributions from the $2N$ interacting dipoles in the far-field [238]:

$$Q_{ext}^{N} = \frac{4k}{NR^2} \sum_{i=1}^{N} \left(\frac{\mathrm{Im}(\mathbf{P}_i \cdot \mathbf{E}_i^{0*})}{|E_0|^2} + \frac{\mathrm{Im}(\mathbf{M}_i \cdot \mathbf{H}_i^{0*})}{|H_0|^2} \right). \tag{4.12}$$

For the 1D periodic array shown in Fig. 4.11(c), each particle in the array has

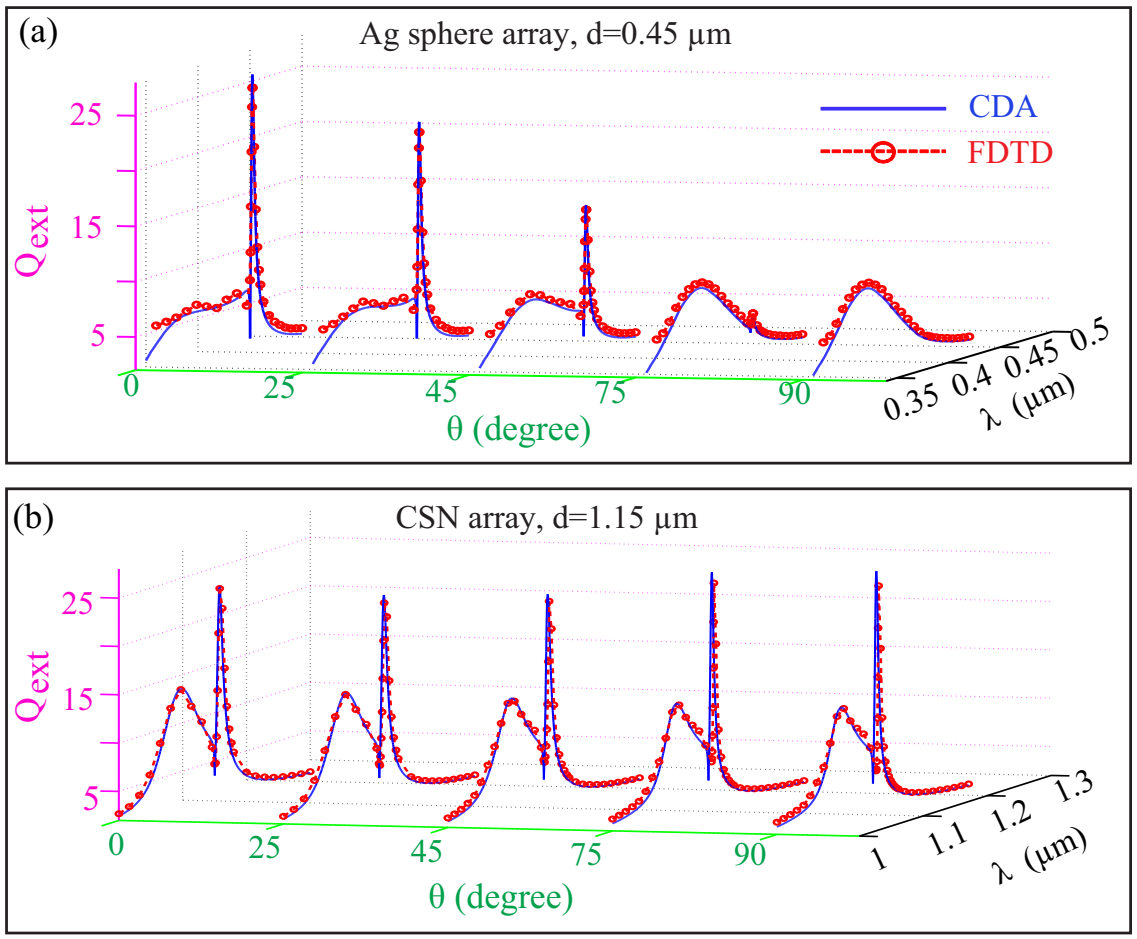

Figure 4.12: CDA (solid line) and FDTD (dashed line with circles) results of the extinction efficiency spectra for a 1D array of (a) silver spheres with $d = 0.5$ μm and (b) core-shell nanosphere with $d = 1.15$ μm for five polarization angles of $\theta = 0, 25°, 45°, 75°$, and $90°$. For both cases the Fano dips are located at $\lambda = d$. Parameters for single particles are the same as those in Fig. 4.11.

identical polarization dependent response with x and y projections:

$$P_x = \frac{\alpha_1^e E_0 \cos\theta}{1 - 2\alpha_1^e (C_1 + C_2)}, P_y = \frac{\alpha_1^e E_0 \sin\theta}{1 + 4\alpha_1^e C_2}, \tag{4.13}$$

$$M_x = \frac{-\alpha_1^m H_0 \sin\theta}{1 - 2\alpha_1^m (C_1 + C_2)}, M_y = \frac{\alpha_1^m H_0 \cos\theta}{1 + 4\alpha_1^m C_2}, \tag{4.14}$$

where

$$C_1 = -k^2 \left[\ln\left(2 - 2\cos(kd)\right) + i(2m-1)\pi - kd\right]/2d, \tag{4.15}$$

$$C_2 = \sum\nolimits_{n=1}^{\infty} e^{iknd}(iknd - 1)/n^3 d^3. \tag{4.16}$$

Here d satisfies $(m-1)\lambda < d < m\lambda$ with $m = 1, 2, 3...$, E_0 and H_0 are the amplitude of the electric and magnetic fields of the incident wave respectively. According to Eq. (4.13) and Eq. (4.14), electric and magnetic moments are separable: electric

and magnetic moments are only dependent on the electric and magnetic fields of the incident wave, respectively. Based on Eq. (4.12)-Eq. (4.14) the extinction efficiency for the 1D array is:

$$Q_{ext} = Q_{ext}^{P_x} + Q_{ext}^{P_y} + Q_{ext}^{M_x} + Q_{ext}^{M_y}, \tag{4.17}$$

$$Q_{ext}^{P_x}(\theta) = \frac{4k}{R^2} Im\left(\frac{\alpha_1^e \cos^2\theta}{1 - 2\alpha_1^e(C_1 + C_2)}\right), \tag{4.18}$$

$$Q_{ext}^{P_y}(\theta) = \frac{4k}{R^2} Im\left(\frac{\alpha_1^e \sin^2\theta}{1 + 4\alpha_1^e C_2}\right), \tag{4.19}$$

$$Q_{ext}^{M_x}(\theta) = \frac{4k}{R^2} Im\left(\frac{\alpha_1^m \sin^2\theta}{1 - 2\alpha_1^m(C_1 + C_2)}\right), \tag{4.20}$$

$$Q_{ext}^{M_y}(\theta) = \frac{4k}{R^2} Im\left(\frac{\alpha_1^m \cos^2\theta}{1 + 4\alpha_1^m C_2}\right). \tag{4.21}$$

We note that the term C_2 is always convergent while the term C_1 could be divergent when $\cos(kd) = 1$. The divergence point of C_1 decides the position of the Fano dip, which is always located at $\lambda = d$ [248, 249, 254]. Such wavelength corresponds to the sharp Wood's anomaly and this wavelength is also termed as the Rayleigh wavelength [262–265]. The Fano peaks appears at $\mathrm{Re}[1 - 2\alpha_1^{e,m}(C_1 + C_2)] = 0$, when the projections P_x or M_x reach their maximum, respectively [254]. This means that there will be two independent Fano peaks when the ED and the MD are both supported but separated spectrally [225]. In the region close to the Fano peaks P_x and M_x (moments along x direction) are the dominant contributing terms as $Q_{ext}^{P_x},\ Q_{ext}^{M_x} \gg Q_{ext}^{P_y},\ Q_{ext}^{M_y}$.

When the unit cell of the array contains only single silver nanoparticle [see Fig. 4.11(a)], the magnetic response is negligible $b_1, M_x, M_y, Q_{ext}^{M_x}, Q_{ext}^{M_y} \approx 0$. Thus, the main contribution to the Fano peak comes from the electric dipole moment along x direction only $Q_{ext}^{P_x}(\theta)$. This means that the Fano resonance originates from the interference of two modes (ED and the geometric resonance of the array), and thus, it is highly polarization dependent [see $\cos^2\theta$ dependence in Eq. (4.18)- Eq. (4.21)]. This is understandable as for different polarizations, the ED moments have different orientations, leading to different field overlap between adjacent coupled EDs. The theoretical results based on Eq. (4.13)-Eq. (4.21) for the extinction efficiency of infinite 1D array of silver spheres are shown in Fig. 4.12(a) for five polarization angles of $\theta = 0,\ 25°,\ 45°,\ 75°$, and $90°$ (solid line). As discussed above, the Fano dips are located at $\lambda = d$ and clear polarization dependence features are shown. To confirm the theoretical results, we also do 3D finite-difference time-domain (FDTD, Lumerical) simulations with the results shown in Fig. 4.12(a) (dashed line with circles). Both the CDA analysis and the simulation results agree very well, confirming the validity of the coupled dipole approximations. We note here that such polarization dependence has the origin in the original Wood's observations, where there were both p-anomalies and s-anomalies [262–265]. Also the Fano line shapes shown here is reminiscent of the Wood's anomaly line shapes [264, 265], both of which indicate the existence of Fano resonances.

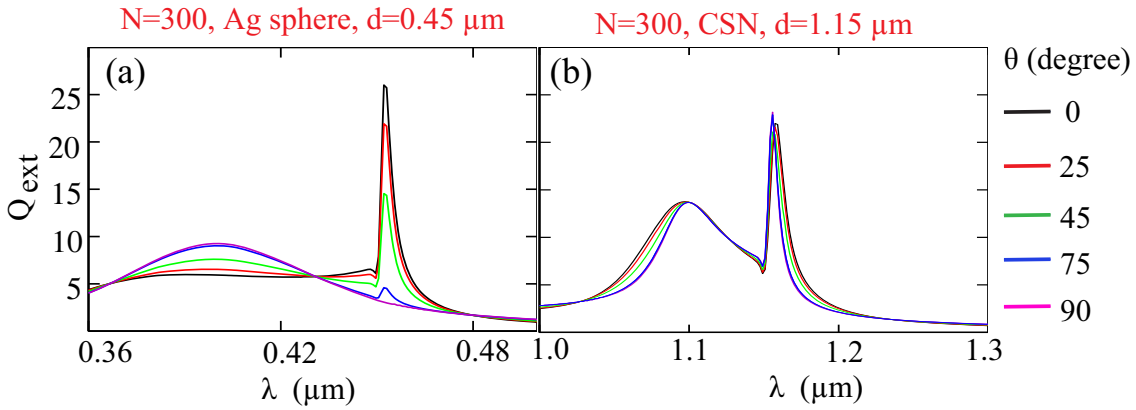

Figure 4.13: Extinction efficiency spectra of five polarization angles of $\theta = 0,\ 25°,\ 45°,\ 75°$, and $90°$ for finite 1D array of (a) 300 silver spheres and (b) 300 core-shell nanospheres. Other parameters are the same as in Fig. 4.11.

When the unit cell contains a core-shell nanosphere [see Fig. 4.11(b)], both modes are excited with $a_1 \approx b_1$ and according to Eq. (4.1), $\alpha_1^e \approx \alpha_1^m \approx \alpha$. Therefore, two main contributions to the Fano peak come from $Q_{ext}^{P_x}(\theta)$ and $Q_{ext}^{M_x}(\theta)$. Although both terms show polarization dependence, the overall effect of them

$$Q_{ext} = Q_{ext}^{P_x}(\theta) + Q_{ext}^{M_x}(\theta) = \frac{4k}{r^2} Im\left[\frac{\alpha}{1 - 2\alpha(C_1 + C_2)}\right] \tag{4.22}$$

is polarization independent. In sharp contrast to the case of silver sphere array, in the array of core-shell nanospheres the Fano resonance comes from the interference of three resonances (the ED, the MD and geometric resonance of the array) rather than two. This means that the ED and the MD can interference simultaneously with the geometric resonance of the array, leading to polarization independent Fano resonances, irrespective of different orientations of the EDs and MDs. The CDA results for 1D array of core-shell nanospheres are shown in Fig. 4.12(b) (solid line), which show the Fano dip at the Rayleigh wavelength $\lambda = d$. It is clear that compared to the case of silver sphere array [Fig. 4.12(a)], the Fano resonances are practically polarization independent. The FDTD simulation results in Fig. 4.12(b) (dashed line with circles) agree well with the CDA results, verifying the theoretical analysis.

Then we study the realistic structure of finite 1D array with N nanoparticles. For a finite array, in contrast to the infinite array, the electric and magnetic moments are coupled to each other (all resonant moments are dependent on both electric and magnetic fields of the incident wave) and each particle has different responses. In Fig. 4.13(a) and (b) we show the extinction efficiency [Eq. (4.12)] of the finite arrays of 300 silver spheres and 300 core-shell nanospheres respectively. As is clear from Fig. 4.13, in finite arrays the polarization dependent or independent features are preserved.

Near-field enhancement in the 1D arrays of core-shell nanospheres

Up to now we have achieved polarization independent Fano resonances in the array of core-shell nanospheres in terms of extinction efficiency spectra, which is a far-field feature. As a next step, we investigate the near-field distributions for different polarizations of the incident waves. We would like to stress again that no real magnetic materials are involved in our study, and the MD supported by the core-shell nanosphere is *artificial*, which comes from the circulation of displacement currents in the high permittivity shell [206]. The dipole approximation comes from the far-field scattering similarity to Ref. [233], and the near-field distribution of this virtual MD would be significantly different from that of a real MD. To clarify this, in Fig. 4.14(a) we show a dielectric ($n = 3.5$) shell structure with hollow core that support dominantly a MD resonance [199, 229, 233] in the spectral range 1 μm-1.3 μm. The inner radius is 38 nm, outer radius is 150 nm and the central MD resonant wavelength is $\lambda = 1195$ nm. In Fig. 4.14(b) we show the corresponding near-field (electric and magnetic field amplitude) distributions. Although for a metal sphere at the ED resonant wavelength, the near-field shows typical dipole distribution [199], for the *artificial* MD shell [206] in Fig. 4.14(b), the near-field shows dominant magnetic field enhancement within the shell, without exhibiting obvious dipolar type distribution.

As a next step, we investigate the near-field distributions of the core-shell nanosphere array at the Fano peak for different polarizations. According to Eq. (4.13) and Eq. (4.14), at the Fano peak $\mathrm{Re}[1 - 2\alpha(C_1 + C_2)] = 0$ for the array of core-shell nanospheres (the corresponding wavelength is approximately 1159.5 nm), both electric moments P_x and magnetic moments M_x can be enhanced but individually they are highly polarization dependent ($\cos\theta$ and $\sin\theta$ dependence respectively). This means that at the Fano peak, for different polarization angles of the incident wave, the ED and the MD moments can be selectively enhanced. In Fig. 4.14(c)-(h) we show the normalized near-field distribution (electric field and magnetic field at the plane $z = 0$ for a unit cell particle in an infinite array) at the Fano peak ($\lambda = 1159.5$ nm) for three polarization angles $\theta = 0$, 45°, and 90°. For $\theta = 0$, the ED ($\cos\theta$ dependence) is dominant and the near-field shows the typical feature of an ED [199, 200] [Fig. 4.14(c) and Fig. 4.14(f)]. For $\theta = 90°$, the MD is dominant ($\sin\theta$ dependence) and the near-field shows the typical features of a pure MD [Fig. 4.14(e) and Fig. 4.14(h)] with dominant magnetic field enhancement, similar to what is shown in Fig. 4.14(b). For $\theta = 45°$, the MD and the ED are equally excited and the near-field shows hybrid features [Fig. 4.14(d)-(g)]. According to Fig. 4.14, in the array of core-shell nanospheres, the near-field distributions can be effectively manipulated by different polarizations of the incident wave. The electric fields can be selectively enhanced [Fig. 4.14(c)] or suppressed [Fig. 4.14(e)]. For the magnetic fields, though the maximum value is stable against θ (due to the *artificial* nature of the MD), the field distribution patterns can be significantly changed with different polarizations [Fig. 4.14(f)-(h)]. Those flexible near-field manipulations together with the far-field polarization independent Fano resonances make our structures superior to other similar ones that support either only the ED [253–256], or only the

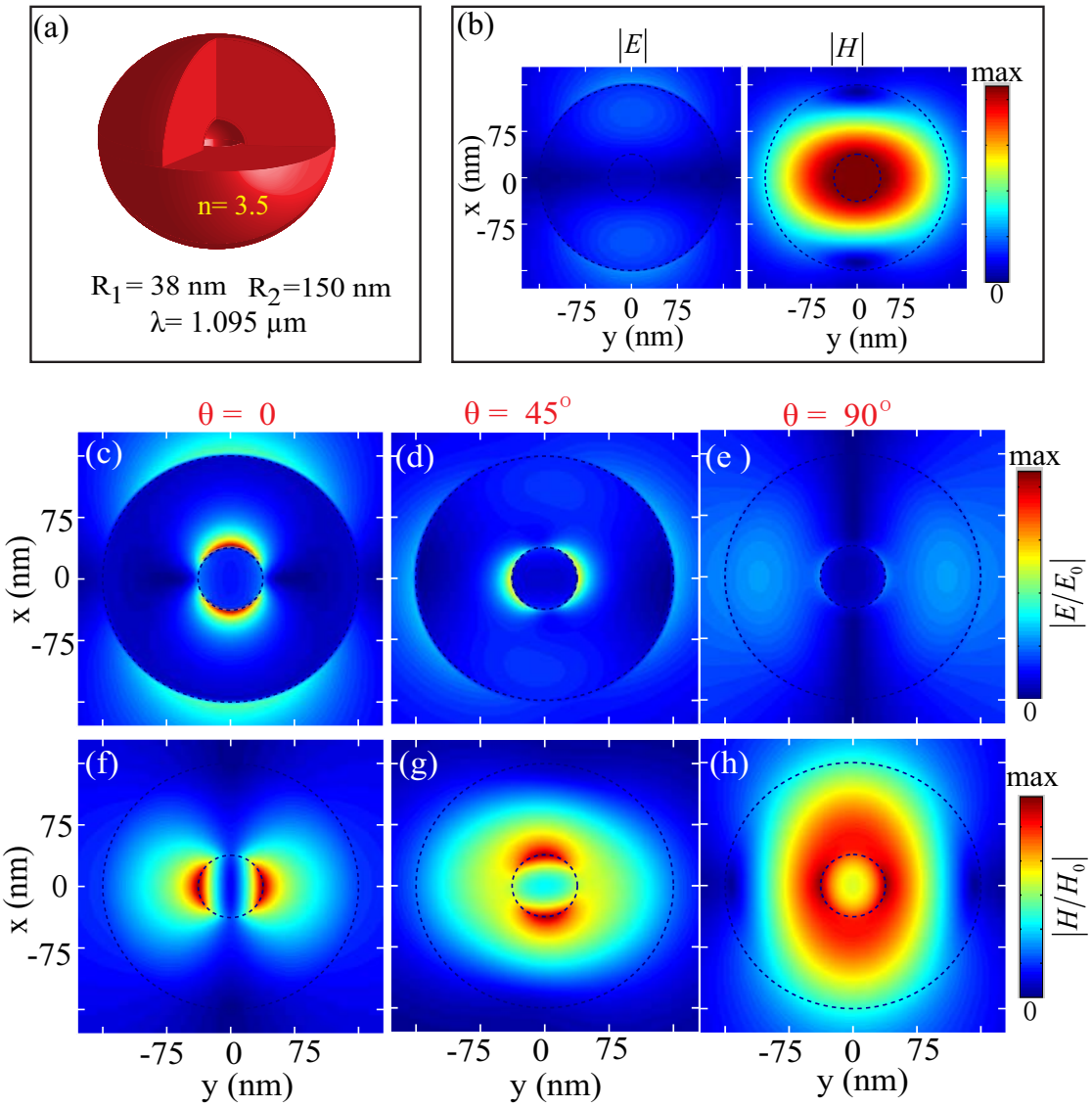

Figure 4.14: (a) A dielectric ($n = 3.5$) shell structure with hollow core that support a MD resonance. The inner radius 38 nm, outer radius 150 nm and the central MD resonant wavelength is $\lambda = 1095$ nm. (b) Corresponding near-field (normalized electric and magnetic field) distributions. (c)-(h) Normalized near-field distributions of a unit cell in a 1D infinite array of core-shell nanospheres for three polarization angles of $\theta = 0, 45°$, and $90°$ at the Fano peak position $\lambda = 1159.5$ nm. Other parameters are the same as in Fig. 4.12 and Fig. 4.11.

MD [266, 267], or both [225] but with the two resonances significantly separated spectrally. Also according to Fig. 4.12(b), the existence of polarization independent Fano resonances indicates that all the near-field manipulations can be carried out without being detected in the far-field.

Polarization independent Fano resonance in 2D arrays of core-shell nanospheres

It is worth mentioning that the polarization independent features of the core-shell nanospheres originate from the simultaneously equal electric and magnetic responses of each particle itself, rather than the overall symmetry of the whole structure [236, 268]. This is shown in Fig. 4.12 with 1D structures. To further confirm this, we investigate a 2D rectangular lattice shown in Fig. 4.15(a), with lattice constants d_x and d_y along vertical and horizontal directions, respectively. Figures 4.15(b)-(d) shows the extinction efficiency spectra of the Ag sphere lattice for different polarizations with $d_x = 0.45$ μm and $d_y = 0.43$ μm, where the Fano maxima are marked as F_x and F_y for the Fano resonances arising from coupling between particles along x and y directions, respectively. The two Fano resonances can be selectively excited with different polarization angles, showing clearly the polarization dependent features of the Ag sphere lattice. In contrast, in Fig. 4.15(e)-(g) we show the extinction efficiency spectra for a lattice of core-shell nanospheres with $d_x = 1.17$ μm and $d_y = 1.11$ μm. As each core-shell nanosphere has equal electric and magnetic responses, for different polarizations both Fano resonances related to the two lattice constants can be excited simultaneously and the polarization independent features are shown. We emphasize that for both lattices there is a third lattice constant along the diagonal direction. However, along this direction, the geometric resonance is spectrally far from the individual resonance supported by each particle, thus there is no coupling between them and no Fano resonances will arise along this third direction.

Conclusion

In conclusion, we demonstrate the polarization independent Fano resonances in arrays of core-shell nanospheres, with each nanosphere supporting a pair of orthogonal ED and MD, which coincide spectrally with the same amplitude. For different polarizations, the ED and the MD can interfere simultaneously with the geometric resonance (sharp Wood's anomaly) of the array through diffractive coupling, producing polarization independent Fano resonances. We further demonstrate that at the Fano peak, the ED and the MD can be selectively controlled through the change of polarizations, leading to flexible near-field manipulation without being detected in the far-field. We expect that the proposed structure can work as an effective platform with much more flexibilities to study nonlinear and lasing effects when nonlinear and/or gain materials are incorporated. The principle of overlapping the ED and the MD with the same strength to produce a hybrid background state for the realization of polarization independent Fano resonances can be extended to higher order modes or to other structures (not necessarily spherical particles) which support orthogonal electric and magnetic resonances. Such mechanism of superimposing orthogonal electric and magnetic modes to achieve polarization independent Fano resonances is not confined to optics, and it can be applied to other fields including atomic and nuclear physics.

4.4 Summary

The central goal of this chapter is to overlap the artificial MD with the ED, and employ their inference to shape the scattering patterns of plasmonic structures. We shown that for the core-shell nanosphere, the ED and the MD can be overlapped with the same strength, thus leading to unidirectional scattering. We also show that the directionality of the scattering can be further enhanced in a 1D array of such nanospheres and the unidirectional scattering response is practically broadband. For the core-shell nanowire of p-polarized incident waves, when the ED and MD are tuned to overlap spectrally, as the ED corresponds to two angular momentum channels while the MD corresponds to only one channel, its magnitude is twice the magnitude of the MD. Consequently, in sharp contrast to the spherical structure investigated before where the scattering is suppressed at only the backward direction, here we demonstrate a pair of angles along which the scattering is vanishing. It is also demonstrated that the scattering features are highly polarization dependent, and the vanishing scattering angles can also be obtained through employing the Fano resonance, which is induced by the interference of the broad MD and the narrow higher order electric modes. At the end of this chapter, in the arrays of core-shell nanospheres, with each nanosphere supporting a pair of orthogonal ED and MD, which can interfere simultaneously with the geometric resonance (sharp Wood's anomaly) of the array through diffractive coupling, we produce polarization independent Fano resonances.

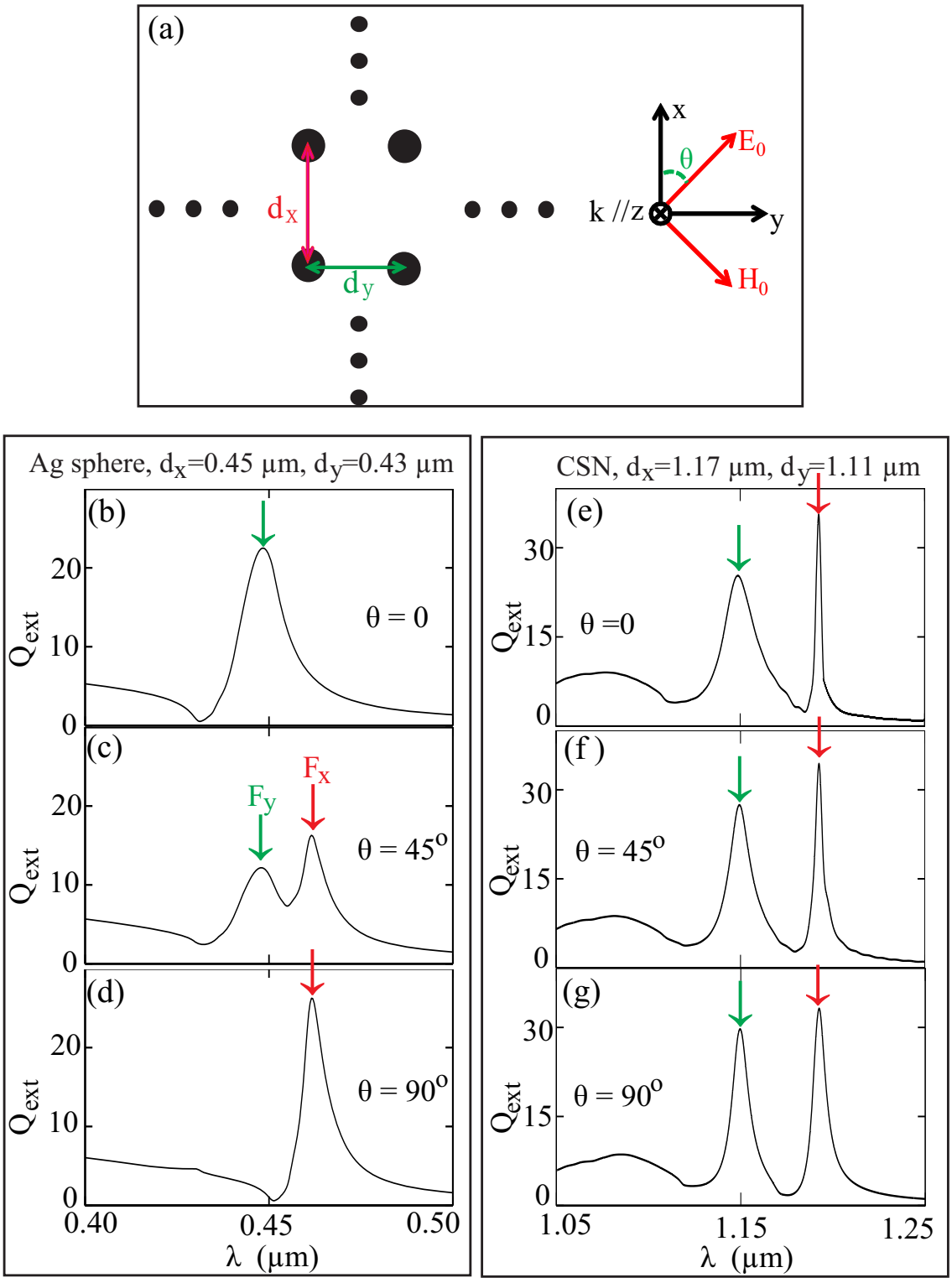

Figure 4.15: (a) Schematic geometry of the 2D rectangular lattice with lattice constants d_x and d_y along vertical and horizontal directions, respectively. Extinction efficiency spectra of: (b-d) the Ag sphere lattice with $d_x = 0.45$ μm and $d_y = 0.43$ μm and (e-g) the core-shell nanosphere lattice with $d_x = 1.17$ μm and $d_y = 1.11$ μm. For both lattices the results of three polarization angles of $\theta = 0, 45°$, and $90°$ are shown. The parameters of single particles are the same as in Fig. 4.11. F_x and F_y mark the peaks of the Fano resonances arising from coupling between particles along x and y direction, respectively.

CHAPTER 5

Conclusions and outlook

Fostered by the observation of extraordinary optical transmission and the rise of the new field of metamaterials, recently the field of plasmonics is attracting more interest than ever before. Named by the group of Harry Atwater in 2000, the term of plasmonics is a very broad concept and any science and technology that is related to the coherent coupling of photons to collective oscillations of electrons at the conductor-dielectric interface can be categorized into this field. According to the type of the energy confinement, the field of plasmonics can be roughly divided into two branches: propagating surface plasmon polaritons and localized surface plasmons. The former branch deals mainly with topics related to the subwavelength energy transportation and the latter one deals mainly with topics related to the scattering of light by plasmonic particles. Furthermore, the LSPs can be geometrized through Bohr condition and thus are highly related to SPPs. Here in this thesis, we discuss light manipulation by plasmonic nanostructures and address several challenging problems in the field of plasmonics, including contents about both propagating surface plasmon polaritons and localized surface plasmons.

We demonstrate a simple mechanism to achieve plasmonic spectral gaps based on the coupling of forward and backward modes. We study a plasmonic coupler involving backward and forward modes of coupled plasmonic nanocavities. The simultaneously achievable contra-directional energy flows and co-directional phase velocities in different channels lead to a spectral gap, despite the absence of periodic structures along the waveguide. We also demonstrate that a complete spectral gap can be achieved in a symmetric structure composed of four coupled waveguides.

We realize efficient and flexible plasmonic beam manipulations in various plasmonic potentials: (1) we introduce the concept of polychromatic plasmonics and suggest a broadband plasmonic lens for nanofocusing of surface plasmon polaritons based on full parabolic potentials; (2) we demonstrate a plasmonic analogue of a quantum paddle ball that describes the dynamics of a quantum particle in a half-parabolic potential (under a linear restoring force bouncing off an impenetrable barrier); (3) we propose and investigate the adiabatic nanofocusing of the fundamental modes in tapered plasmonic parabolic potentials where light is compressed in both transverse directions due to increasingly stronger parabolic potentials and decreasing dielectric layer width; (4) we demonstrate the efficient manipulations of plasmonic Airy beams in linear optical potentials, including acceleration, com-

pensation and reversing the self-deflection of the plasmonic Airy beams without compromising the self-healing properties.

We introduce artificial magnetic MDs into plasmonic nanostructures and manage to effectively shape the scattering patterns, through the interferences of EDs and MDs: (1) we have studied the scattering properties of core-shell nanospheres and show that they exhibit azimuthally symmetric unidirectional scattering, which originates from the interference of the ED and the MD that coexist with the same strength at the same frequency. The directionality of a single particle can be enhanced when they are arranged in a chain and the operating wavelength range for unidirectional scattering of the chain is practically broadband; (2) we extend the approach of scattering shaping through overlapping of EDs and MDs from 3D nanospheres to 2D core-shell nanowires. Within such nanowires, for p polarization incident waves, each electric resonance corresponds to two angular momentum channels while the magnetic resonance corresponds to only one channel. Consequently when the electric dipole and magnetic dipole are tuned to overlap spectrally, the magnitude of the electric dipole is twice that of the magnetic one, leading to a pair of vanishing scattering angles. We further demonstrate that the scattering features of nanowires are polarization dependent, and vanishing scattering angles can also be induced by Fano resonances due to the interference of high order electric modes with the broad magnetic dipole background; (3) we study the scattering properties of arrays of core-shell nanospheres and reveal the existence of polarization independent Fano resonances due to the interaction of a pair of degenerate orthogonal ED and MD of the same strength with the spectrally-narrow geometric resonance of the array. Furthermore, we show that for different polarizations of the incident plane waves, the electric and magnetic modes supported by each nanoparticle can be selectively controlled, providing extra freedom for near-field manipulation, with applications to nonlinear and lasing devices.

Although there have been steady and rapid progress in the field of plasmonics especially after 1998 when the phenomenon of extraordinary transmission was observed, still many challenges are laying ahead. The most urgent and challenging one is probably how to alleviate or even eliminate the effect of intrinsic loss of metal. It is shown that incorporating gain media can compensate the loss, while the side effects of gain media on the signal carried by plasmonic pulse is not clear. At the same time, the narrow operating spectral regime of the gain media and the requirement of an external pump will probably further restrict the applications of gain-assisted plasmonic devices. Other challenges include the clear and accurate characterization of the nonlocal and nonlinear responses of metal, the interplay of nonlocality and quantum tunneling for plasmonic nanoparticle interaction, quantum effects like single plasmon and their entanglement, singular plasmons and so on. The existence of the challenges mentioned above should be the reason of optimism rather than pessimism. Actually those challenges indicate the future development direction of the whole field.

Another rather exciting trend of the field of plasmonics is that it merges rapidly with several promising emerging fields, including spinoptics [269–283], graphene [284–288], and topological insulators [289–294]:

Photons that carry angular momentum (spin and/or orbital angular momentum) have nontrivial Berry curvature in momentum space, which plays a vitally important role in the field of spinoptics [269–271, 282]. Due to the duality of real space and momentum space, an extra term in the dynamical equation of motion, termed as the anomalous velocity or Lorentz force in momentum space, will naturally arise duo to this Berry curvature [282]. This term can provide extra freedom for beam manipulation for photons carrying angular momentum, including unidirectional SPPs excitation [278–280], the spin Hall effect of light [270, 272, 275], the plasmonic Aharonov-Bohm effect [274] and so on.

The current vibrant field of graphene also gives the plasmonic community a strong stimulus. As a 2D system within which the carbon atoms are arranged in a honeycomb lattice, graphene has intrinsic plasmonic effects [284, 285], and the combination of graphene with nanoplasmonic structures may lead to totally new optical devices. Such devices can operate with high speed, low driving force and energy consumption, and can work at wide rage of spectral regimes [285]. Promising output that might come out from the marriage of graphene and plasmonic structures include efficient photocells, ultrafast optical modulators, graphene-based 2D plasmonic lasers, ultrasensitive chemical sensors and biosensors, and so on. At the same time, the hybrid plasmonic-graphene structures might provide an efficient platform for research in fundamental physics, including quantum spin Hall effect for plasmons, ultra-strong light matter interactions and nonlinearity, pseudospin for SPPs and so on [282, 284, 290, 295, 296].

A third impetus that might push the field of plasmonics into unprecedented depth and breadth comes from the new topic of topological insulators [289–291]. An immediate motivation from this impetus is the search for topological states of surface plasmons, similar to what have already been demonstrated for photons [292, 293, 297–299]. At the same time, it is shown that the complete characterization of topological insulators requires an extra topological magnetoelectric term, which indicates the efficient coupling between electric and magnetic fields. Such term might bring out totally novel effects for SPPs excited on the surface of topological insulators [294], which do not exist for SPPs excited at the interface of conventional metal-dielectric structures.

To conclude, we anticipate that there is plenty of room of the development of plasmonics and this field will keep on its expansion and spread widely more into not only other branches of optics and physics, but also into biological and medical researches, finding deeper space and extra dimensions to establish new physical principles, and numerous practical applications in our daily life.

Bibliography

[1] J. Needham, "Science and civilization in china - state of the project," Interdiscipl. Sci. Rev. **5**, 263 (1980).

[2] M. Born and E. Wolf, *Principles of optics : electromagnetic theory of propagation, interference and diffraction of light* (Cambridge University Press, Cambridge; New York, 1999), 7th ed.

[3] L. Novotny and B. Hecht, *Principles of nano-optics* (Cambridge University Press, Cambridge, 2012), 2nd ed.

[4] J. W. Goodman, *Introduction to Fourier optics* (Roberts & Co., Englewood, Colo., 2005), 3rd ed.

[5] P. W. Carlin, "The minimum spot size for a focused layer and the uncertainty relation," Proc. IEEE **52**, 1371 (1964).

[6] E. H. K. Stelzer and S. Grill, "The uncertainty principle applied to estimate focal spot dimensions," Opt. Commun. **173**, 51 (2000).

[7] E. H. K. Stelzer, "Light microscopy - beyond the diffraction limit?" Nature **417**, 806 (2002).

[8] L. M. Tong, J. Y. Lou, and E. Mazur, "Single-mode guiding properties of subwavelength-diameter silica and silicon wire waveguides," Opt. Express **12**, 1025 (2004).

[9] W. L. Barnes, A. Dereux, and T. W. Ebbesen, "Surface plasmon subwavelength optics," Nature **424**, 824 (2003).

[10] S. A. Maier, *Plasmonics : fundamentals and applications* (Springer, New York, 2007).

[11] J. A. Schuller, E. S. Barnard, W. S. Cai, Y. C. Jun, J. S. White, and M. L. Brongersma, "Plasmonics for extreme light concentration and manipulation," Nat. Mater. **9**, 193 (2010).

[12] S. I. Bozhevolnyi, *Plasmonic nanoguides and circuits* (World Scientific Pub., Singapore., 2009).

[13] A. V. Zayats, I. I. Smolyaninov, and A. A. Maradudin, "Nano-optics of surface plasmon polaritons," Phys. Rep. **408**, 131 (2005).

[14] J. M. Pitarke, V. M. Silkin, E. V. Chulkov, and P. M. Echenique, "Theory of surface plasmons and surface-plasmon polaritons," Rep. Prog. Phys. **70**, 1 (2007).

[15] H. A. Atwater, "The promise of plasmonics," Sci. Am. **296**, 56 (2007).

[16] K. A. Willets and R. P. Van Duyne, "Localized surface plasmon resonance spectroscopy and sensing," Annu. Rev. Phys. Chem. **58**, 267 (2007).

[17] T. W. Ebbesen, H. J. Lezec, H. F. Ghaemi, T. Thio, and P. A. Wolff, "Extraordinary optical transmission through sub-wavelength hole arrays," Nature **391**, 667 (1998).

[18] J. B. Pendry, "Negative refraction makes a perfect lens," Phys. Rev. Lett. **85**, 3966 (2000).

[19] R. A. Shelby, D. R. Smith, and S. Schultz, "Experimental verification of a negative index of refraction," Science **292**, 77 (2001).

[20] W. Cai and V. M. Shalaev, *Optical metamaterials : fundamentals and applications* (Springer, New York, 2010).

[21] R. C. McPhedran, I. V. Shadrivov, B. T. Kuhlmey, and Y. S. Kivshar, "Metamaterials and metaoptics," NPG. Asia. Mater. **3**, 100 (2011).

[22] N. I. Zheludev and Y. S. Kivshar, "From metamaterials to metadevices," Nat. Mater. **11**, 917 (2012).

[23] C. N. Yang, "Quantum numbers, chern classes, and a bodhisattva," Phys. Today **65**, 33 (2012).

[24] L. D. Landau and E. M. Lifshits, *Quantum mechanics : non-relativistic theory* (Pergamon Press, Oxford; New York, 1977), 3rd ed.

[25] Z. C. Ruan and S. H. Fan, "Superscattering of light from subwavelength nanostructures," Phys. Rev. Lett. **105**, 013901 (2010).

[26] K. Huang, *Fundamental forces of nature: the story of gauge fields* (World Scientific, Singapore; Hackensack, NJ, 2007).

[27] A. D. Boardman, *Electromagnetic surface modes* (Wiley, Chichester; New York, 1982).

[28] D. K. Gramotnev and S. I. Bozhevolnyi, "Plasmonics beyond the diffraction limit," Nat. Photon. **4**, 83 (2010).

[29] K. J. Vahala, "Optical microcavities," Nature **424**, 839 (2003).

[30] B. K. Min, E. Ostby, V. Sorger, E. Ulin-Avila, L. Yang, X. Zhang, and K. Vahala, "High-q surface-plasmon-polariton whispering-gallery microcavity," Nature **457**, 455 (2009).

[31] K. R. Li, M. I. Stockman, and D. J. Bergman, "Self-similar chain of metal nanospheres as an efficient nanolens," Phys. Rev. Lett. **91**, 227402 (2003).

[32] C. Ropers, C. C. Neacsu, T. Elsaesser, M. Albrecht, M. B. Raschke, and C. Lienau, "Grating-coupling of surface plasmons onto metallic tips: A nanoconfined light source," Nano Lett. **7**, 2784 (2007).

[33] M. Quinten, A. Leitner, J. R. Krenn, and F. R. Aussenegg, "Electromagnetic energy transport via linear chains of silver nanoparticles," Opt. Lett. **23**, 1331 (1998).

[34] M. L. Brongersma, J. W. Hartman, and H. A. Atwater, "Electromagnetic energy transfer and switching in nanoparticle chain arrays below the diffraction limit," Phys. Rev. B **62**, 16356 (2000).

[35] S. A. Maier, P. G. Kik, H. A. Atwater, S. Meltzer, E. Harel, B. E. Koel, and A. A. G. Requicha, "Local detection of electromagnetic energy transport below the diffraction limit in metal nanoparticle plasmon waveguides," Nat. Mater. **2**, 229 (2003).

[36] M. L. Brongersma and V. M. Shalaev, "The case for plasmonics," Science **328**, 440 (2010).

[37] S. I. Bozhevolnyi, V. S. Volkov, E. Devaux, J. Y. Laluet, and T. W. Ebbesen, "Channel plasmon subwavelength waveguide components including interferometers and ring resonators," Nature **440**, 508 (2006).

[38] W. S. Cai, W. Shin, S. H. Fan, and M. L. Brongersma, "Elements for plasmonic nanocircuits with three-dimensional slot waveguides," Adv. Mater. **22**, 5120 (2010).

[39] S. Kim, J. H. Jin, Y. J. Kim, I. Y. Park, Y. Kim, and S. W. Kim, "High-harmonic generation by resonant plasmon field enhancement," Nature **453**, 757 (2008).

[40] I. Y. Park, S. Kim, J. Choi, D. H. Lee, Y. J. Kim, M. F. Kling, M. I. Stockman, and S. W. Kim, "Plasmonic generation of ultrashort extreme-ultraviolet light pulses," Nat. Photon. **5**, 678 (2011).

[41] D. Y. Fedyanin, A. V. Krasavin, A. V. Arsenin, and A. V. Zayats, "Surface plasmon polariton amplification upon electrical injection in highly integrated plasmonic circuits," Nano Lett. **12**, 2459 (2012).

[42] G. A. Wurtz and A. V. Zayats, "Nonlinear surface plasmon polaritonic crystals," Laser Photonics Rev. **2**, 125 (2008).

[43] A. V. Krasavin, T. P. Vo, W. Dickson, P. M. Bolger, and A. V. Zayats, "All-plasmonic modulation via stimulated emission of copropagating surface plasmon polaritons on a substrate with gain," Nano Lett. **11**, 2231 (2011).

[44] O. Hess, J. B. Pendry, S. A. Maier, R. F. Oulton, J. M. Hamm, and K. L. Tsakmakidis, "Active nanoplasmonic metamaterials," Nat. Mater. **11**, 573 (2012).

[45] M. Kauranen and A. V. Zayats, "Nonlinear plasmonics," Nat. Photon. **6**, 737 (2012).

[46] G. A. Wurtz, R. Pollard, W. Hendren, G. P. Wiederrecht, D. J. Gosztola, V. A. Podolskiy, and A. V. Zayats, "Designed ultrafast optical nonlinearity in a plasmonic nanorod metamaterial enhanced by nonlocality," Nat. Nanotech. **6**, 106 (2011).

[47] K. F. MacDonald, Z. L. Samson, M. I. Stockman, and N. I. Zheludev, "Ultrafast active plasmonics," Nat. Photon. **3**, 55 (2009).

[48] Y. Zhang, N. K. Grady, C. Ayala-Orozco, and N. J. Halas, "Three-dimensional nanostructures as highly efficient generators of second harmonic light," Nano Lett. **11**, 5519 (2011).

[49] M. A. Noginov, G. Zhu, A. M. Belgrave, R. Bakker, V. M. Shalaev, E. E. Narimanov, S. Stout, E. Herz, T. Suteewong, and U. Wiesner, "Demonstration of a spaser-based nanolaser," Nature **460**, 1110 (2009).

[50] R. F. Oulton, V. J. Sorger, T. Zentgraf, R. M. Ma, C. Gladden, L. Dai, G. Bartal, and X. Zhang, "Plasmon lasers at deep subwavelength scale," Nature **461**, 629 (2009).

[51] G. A. Wurtz, R. Pollard, and A. V. Zayats, "Optical bistability in nonlinear surface-plasmon polaritonic crystals," Phys. Rev. Lett. **97**, 057402 (2006).

[52] A. V. Kabashin, P. Evans, S. Pastkovsky, W. Hendren, G. A. Wurtz, R. Atkinson, R. Pollard, V. A. Podolskiy, and A. V. Zayats, "Plasmonic nanorod metamaterials for biosensing," Nat. Mater. **8**, 867 (2009).

[53] A. N. Grigorenko, V. G. Kravets, F. Schedin, and A. V. Kabashin, "Sensitivity of collective plasmon modes of gold nanoresonators to local environment," Opt. Lett. **35**, 956 (2010).

[54] A. I. Kuznetsov, A. B. Evlyukhin, M. R. Goncalves, C. Reinhardt, A. Koroleva, M. L. Arnedillo, R. Kiyan, O. Marti, and B. N. Chichkov, "Laser fabrication of large-scale nanoparticle arrays for sensing applications," ACS Nano **5**, 4843 (2011).

[55] J. N. Anker, W. P. Hall, O. Lyandres, N. C. Shah, J. Zhao, and R. P. Van Duyne, "Biosensing with plasmonic nanosensors," Nat. Mater. **7**, 442 (2008).

[56] S. Kawata, Y. Inouye, and P. Verma, "Plasmonics for near-field nano-imaging and superlensing," Nat. Photon. **3**, 388 (2009).

[57] N. Fang, H. Lee, C. Sun, and X. Zhang, "Sub-diffraction-limited optical imaging with a silver superlens," Science **308**, 534 (2005).

[58] L. Novotny and N. van Hulst, "Antennas for light," Nat. Photon. **5**, 83 (2011).

[59] A. G. Curto, G. Volpe, T. H. Taminiau, M. P. Kreuzer, R. Quidant, and N. F. van Hulst, "Unidirectional emission of a quantum dot coupled to a nanoantenna," Science **329**, 930 (2010).

[60] H. A. Atwater and A. Polman, "Plasmonics for improved photovoltaic devices," Nat. Mater. **9**, 865 (2010).

[61] X. J. Ni, N. K. Emani, A. V. Kildishev, A. Boltasseva, and V. M. Shalaev, "Broadband light bending with plasmonic nanoantennas," Science **335**, 427 (2012).

[62] N. F. Yu, P. Genevet, M. A. Kats, F. Aieta, J. P. Tetienne, F. Capasso, and Z. Gaburro, "Light propagation with phase discontinuities: Generalized laws of reflection and refraction," Science **334**, 333 (2011).

[63] L. R. Hirsch, R. J. Stafford, J. A. Bankson, S. R. Sershen, B. Rivera, R. E. Price, J. D. Hazle, N. J. Halas, and J. L. West, "Nanoshell-mediated near-infrared thermal therapy of tumors under magnetic resonance guidance," P. Natl. Acad. Sci. USA. **100**, 13549 (2003).

[64] R. Huschka, J. Zuloaga, M. W. Knight, L. V. Brown, P. Nordlander, and N. J. Halas, "Light-induced release of dna from gold nanoparticles: Nanoshells and nanorods," J. Am. Chem. Soc. **133**, 12247 (2011).

[65] D. E. Chang, A. S. Sorensen, P. R. Hemmer, and M. D. Lukin, "Quantum optics with surface plasmons," Phys. Rev. Lett. **97**, 053002 (2006).

[66] A. V. Akimov, A. Mukherjee, C. L. Yu, D. E. Chang, A. S. Zibrov, P. R. Hemmer, H. Park, and M. D. Lukin, "Generation of single optical plasmons in metallic nanowires coupled to quantum dots," Nature **450**, 402 (2007).

[67] A. Ridolfo, O. Di Stefano, N. Fina, R. Saija, and S. Savasta, "Quantum plasmonics with quantum dot-metal nanoparticle molecules: influence of the fano effect on photon statistics," Phys. Rev. Lett. **105**, 263601 (2010).

[68] J. Zuloaga, E. Prodan, and P. Nordlander, "Quantum plasmonics: optical properties and tunability of metallic nanorods," ACS Nano **4**, 5269 (2010).

[69] Z. Jacob and V. M. Shalaev, "Plasmonics goes quantum," Science **334**, 463 (2011).

[70] J. A. Scholl, A. L. Koh, and J. A. Dionne, "Quantum plasmon resonances of individual metallic nanoparticles," Nature **483**, 421 (2012).

[71] G. Di Martino, Y. Sonnefraud, S. Kena-Cohen, M. Tame, S. K. Ozdemir, M. S. Kim, and S. A. Maier, "Quantum statistics of surface plasmon polaritons in metallic stripe waveguides," Nano Lett. **12**, 2504 (2012).

[72] R. Esteban, A. G. Borisov, P. Nordlander, and J. Aizpurua, "Bridging quantum and classical plasmonics with a quantum-corrected model," Nat. Commun. **3**, 825 (2012).

[73] K. J. Savage, M. M. Hawkeye, R. Esteban, A. G. Borisov, J. Aizpurua, and J. J. Baumberg, "Revealing the quantum regime in tunnelling plasmonics," Nature **491**, 574 (2012).

[74] S. M. Xiao, V. P. Drachev, A. V. Kildishev, X. J. Ni, U. K. Chettiar, H. K. Yuan, and V. M. Shalaev, "Loss-free and active optical negative-index metamaterials," Nature **466**, 735 (2010).

[75] S. Roh, T. Chung, and B. Lee, "Overview of the characteristics of micro- and nano-structured surface plasmon resonance sensors," Sensors **11**, 1565 (2011).

[76] N. Liu, M. L. Tang, M. Hentschel, H. Giessen, and A. P. Alivisatos, "Nanoantenna-enhanced gas sensing in a single tailored nanofocus," Nat. Mater. **10**, 631 (2011).

[77] D. J. Bergman and M. I. Stockman, "Surface plasmon amplification by stimulated emission of radiation: Quantum generation of coherent surface plasmons in nanosystems," Phys. Rev. Lett. **90**, 027402 (2003).

[78] N. I. Zheludev, S. L. Prosvirnin, N. Papasimakis, and V. A. Fedotov, "Lasing spaser," Nat. Photon. **2**, 351 (2008).

[79] M. I. Stockman, "Spaser action, loss compensation, and stability in plasmonic systems with gain," Phys. Rev. Lett. **106**, 156802 (2011).

[80] S. Wuestner, A. Pusch, K. L. Tsakmakidis, J. M. Hamm, and O. Hess, "Comment on *Spaser Action, Loss Compensation, and Stability in Plasmonic Systems with Gain*," Phys. Rev. Lett. **107**, 259701 (2011).

[81] M. I. Stockman, "Stockman replies," Phys. Rev. Lett. **107**, 259702 (2011).

[82] J. B. Pendry and S. A. Maier, "Comment on *Spaser Action, Loss Compensation, and Stability in Plasmonic Systems with Gain*," Phys. Rev. Lett. **107**, 259703 (2011).

[83] M. I. Stockman, "Stockman replies," Phys. Rev. Lett. **107**, 259704 (2011).

[84] G. C. Aers, A. D. Boardman, and B. V. Paranjape, "Non-radiative surface plasmon-polariton modes of inhomogeneous metal circular-cylinders," J. Phys. F. Met. Phys. **10**, 53 (1980).

[85] F. J. G. de Abajo, "Nonlocal effects in the plasmons of strongly interacting nanoparticles, dimers, and waveguides," J. Phys. Chem. C **112**, 17983 (2008).

[86] J. Aizpurua and A. Rivacoba, "Nonlocal effects in the plasmons of nanowires and nanocavities excited by fast electron beams," Phys. Rev. B **78**, 035404 (2008).

[87] A. I. Fernandez-Dominguez, A. Wiener, F. J. Garcia-Vidal, S. A. Maier, and J. B. Pendry, "Transformation-optics description of nonlocal effects in plasmonic nanostructures," Phys. Rev. Lett. **108**, 106802 (2012).

[88] Y. Gefen, W. H. Shih, R. B. Laibowitz, and J. M. Viggiano, "Nonlinear behavior near the percolation metal-insulator transition," Phys. Rev. Lett. **57**, 3097 (1986).

[89] M. Perner, P. Bost, U. Lemmer, G. vonPlessen, J. Feldmann, U. Becker, M. Mennig, M. Schmitt, and H. Schmidt, "Optically induced damping of the surface plasmon resonance in gold colloids," Phys. Rev. Lett. **78**, 2192 (1997).

[90] N. N. Lepeshkin, A. Schweinsberg, G. Piredda, R. S. Bennink, and R. W. Boyd, "Enhanced nonlinear optical response of one-dimensional metal-dielectric photonic crystals," Phys. Rev. Lett. **93**, 123902 (2004).

[91] G. Piredda, D. D. Smith, B. Wendling, and R. W. Boyd, "Nonlinear optical properties of a gold-silica composite with high gold fill fraction and the sign change of its nonlinear absorption coefficient," J. Opt. Soc. Am. B **25**, 945 (2008).

[92] P. Ginzburg, A. Hayat, N. Berkovitch, and M. Orenstein, "Nonlocal ponderomotive nonlinearity in plasmonics," Opt. Lett. **35**, 1551 (2010).

[93] J. D. Joannopoulos, *Photonic crystals : molding the flow of light* (Princeton University Press, Princeton, 2008), 2nd ed.

[94] Y. S. Kivshar and G. P. Agrawal, *Optical solitons : from fibers to photonic crystals* (Academic Press, Amsterdam; Boston, 2003).

[95] P. Russell, "Photonic crystal fibers," Science **299**, 358 (2003).

[96] A. Alu and N. Engheta, "Cloaking a sensor," Phys. Rev. Lett. **102**, 233901 (2009).

[97] M. Wegener, G. Dolling, and S. Linden, "Plasmonics - backward waves moving forward," Nat. Mater. **6**, 475 (2007).

[98] H. Shin and S. Fan, "All-angle negative refraction for surface plasmon waves using a metal-dielectric-metal structure," Phys. Rev. Lett. **96**, 073907 (2006).

[99] H. J. Lezec, J. A. Dionne, and H. A. Atwater, "Negative refraction at visible frequencies," Science **316**, 430 (2007).

[100] N. A. P. Nicorovici, R. C. McPhedran, S. Enoch, and G. Tayeb, "Finite wavelength cloaking by plasmonic resonance," New. J. Phys. **10**, 115020 (2008).

[101] G. W. Milton, N. A. P. Nicorovici, and R. C. McPhedran, "Opaque perfect lenses," Physica B **394**, 171 (2007).

[102] J. Helsing, R. C. McPhedran, and G. W. Milton, "Spectral super-resolution in metamaterial composites," New. J. Phys. **13**, 115005 (2011).

[103] P. Y. Chen, R. C. McPhedran, C. M. de Sterke, C. G. Poulton, A. A. Asatryan, L. C. Botten, and M. J. Steel, "Group velocity in lossy periodic structured media," Phys. Rev. A **82**, 053825 (2010).

[104] P. Y. Chen, C. G. Poulton, A. A. Asatryan, M. J. Steel, L. C. Botten, C. M. de Sterke, and R. C. McPhedran, "Folded bands in metamaterial photonic crystals," New. J. Phys. **13**, 053007 (2011).

[105] J. A. Dionne, E. Verhagen, A. Polman, and H. A. Atwater, "Are negative index materials achievable with surface plasmon waveguides? a case study of three plasmonic geometries," Opt. Express **16**, 19001 (2008).

[106] A. Karalis, J. D. Joannopoulos, and M. Soljacic, "Plasmonic-dielectric systems for high-order dispersionless slow or stopped subwavelength light," Phys. Rev. Lett. **103**, 043906 (2009).

[107] C. A. Pfeiffer, E. N. Economou, and K. L. Ngai, "Surface polaritons in a circularly cylindrical interface - surface plasmons," Phys. Rev. B **10**, 3038 (1974).

[108] J. J. Burke, G. I. Stegeman, and T. Tamir, "Surface-polariton-like waves guided by thin, lossy metal films," Phys. Rev. B **33**, 5186 (1986).

[109] B. Prade and J. Y. Vinet, "Guided optical waves in fibers with negative dielectric-constant," J. Lightwave. Technol. **12**, 6 (1994).

[110] D. E. Chang, A. S. Sorensen, P. R. Hemmer, and M. D. Lukin, "Strong coupling of single emitters to surface plasmons," Phys. Rev. B **76**, 035420 (2007).

[111] M. A. Schmidt and P. S. J. Russell, "Long-range spiralling surface plasmon modes on metallic nanowires," Opt. Express **16**, 13617 (2008).

[112] P. B. Catrysse and S. H. Fan, "Understanding the dispersion of coaxial plasmonic structures through a connection with the planar metal-insulator-metal geometry," Appl. Phys. Lett. **94**, 231111 (2009).

[113] B. Sturman, E. Podivilov, and M. Gorkunov, "Eigenmodes for metal-dielectric light-transmitting nanostructures," Phys. Rev. B **76**, 125104 (2007).

[114] T. Yang and K. B. Crozier, "Analysis of surface plasmon waves in metal-dielectric-metal structures and the criterion for negative refractive index," Opt. Express **17**, 1136 (2009).

[115] A. R. Davoyan, W. Liu, A. E. Miroshnichenko, I. V. Shadrivov, Y. S. Kivshar, and S. I. Bozhevolnyi, "Mode transformation in waveguiding plasmonic structures," Photonic Nanostruct. **9**, 207 (2011).

[116] T. P. White and A. A. Sukhorukov, "Transition from slow and frozen to superluminal and backward light through loss or gain in dispersion-engineered waveguides," Phys. Rev. A **85**, 043819 (2012).

[117] H. A. Haus and H. Kogelnik, "Electromagnetic momentum and momentum flow in dielectric waveguides," J. Opt. Soc. Am. **66**, 320 (1976).

[118] L. D. Landau, E. M. Lifshits, and L. P. Pitaevski, *Electrodynamics of continuous media* (Pergamon, Oxford Oxfordshire; New York, 1984), 2nd ed.

[119] R. W. Boyd and D. J. Gauthier, "Controlling the velocity of light pulses," Science **326**, 1074 (2009).

[120] E. Feigenbaum, N. Kaminski, and M. Orenstein, "Negative dispersion: a backward wave or fast light? nanoplasmonic examples," Opt. Express. **17**, 18934 (2009).

[121] A. W. Snyder and J. D. Love, *Optical waveguide theory* (Chapman and Hall, London; New York, 1983).

[122] H. Shin, P. B. Catrysse, and S. Fan, "Effect of the plasmonic dispersion relation on the transmission properties of subwavelength cylindrical holes," Phys. Rev. B **72**, 085436 (2005).

[123] G. P. Agrawal, *Nonlinear fiber optics*, Quantum electronics–principles and applications (Elsevier/Academic Press, Amsterdam; Boston, 2007), 4th ed.

[124] C. M. deSterke, D. G. Salinas, and J. E. Sipe, "Coupled-mode theory for light propagation through deep nonlinear gratings," Phys. Rev. E **54**, 1969 (1996).

[125] P. R. Mcisaac, "Symmetry-induced modal characteristics of uniform waveguides," IEEE. T. Microw. Theory **23**, 421 (1975).

[126] M. J. Steel, T. P. White, C. M. de Sterke, R. C. McPhedran, and L. C. Botten, "Symmetry and degeneracy in microstructured optical fibers," Opt. Lett. **26**, 488 (2001).

[127] I. Newton and A. E. Shapiro, *The optical papers of Isaac Newton* (Cambridge University Press, Cambridge Cambridgeshire; New York, 1984).

[128] E. Schrodinger, *Collected papers on wave mechanics* (Chelsea Pub. Co., New York, 1978).

[129] W. Heisenberg, C. Eckart, and F. C. Hoyt, *The physical principles of the quantum theory*, The University of Chicago science series (The University of Chicago Press, Chicago, Ill., 1930).

[130] S. Longhi, "Quantum-optical analogies using photonic structures," Laser Photonics Rev. **3**, 243–261 (2009).

[131] J. A. Arnaud, *Beam and fiber optics* (Academic Press, New York, 1976).

[132] D. Ambrosini, A. Ponticiello, G. S. Spagnolo, R. Borghi, and F. Gori, "Bouncing light beams and the hamiltonian analogy," Eur. J. Phys. **18**, 284 (1997).

[133] G. A. Siviloglou, J. Broky, A. Dogariu, and D. N. Christodoulides, "Observation of accelerating airy beams," Phys. Rev. Lett. **99**, 213901 (2007).

[134] A. Minovich, A. E. Klein, N. Janunts, T. Pertsch, D. N. Neshev, and Y. S. Kivshar, "Generation and near-field imaging of airy surface plasmons," Phys. Rev. Lett. **107**, 126802 (2011).

[135] L. Li, T. Li, S. M. Wang, C. Zhang, and S. N. Zhu, "Plasmonic airy beam generated by in-plane diffraction," Phys. Rev. Lett. **107**, 126804 (2011).

[136] P. Zhang, S. Wang, Y. M. Liu, X. B. Yin, C. G. Lu, Z. G. Chen, and X. Zhang, "Plasmonic airy beams with dynamically controlled trajectories," Opt. Lett. **36**, 3191 (2011).

[137] C. M. de Sterke, J. N. Bright, P. A. Krug, and T. E. Hammon, "Observation of an optical wannier-stark ladder," Phys. Rev. E **57**, 2365 (1998).

[138] R. Morandotti, U. Peschel, J. S. Aitchison, H. S. Eisenberg, and Y. Silberberg, "Experimental observation of linear and nonlinear optical bloch oscillations," Phys. Rev. Lett. **83**, 4756 (1999).

[139] H. S. Eisenberg, Y. Silberberg, R. Morandotti, and J. S. Aitchison, "Diffraction management," Phys. Rev. Lett. **85**, 1863 (2000).

[140] R. W. Robinett, *Quantum mechanics* (Oxford University Press, New York, 1997).

[141] R. W. Robinett, "Quantum wave packet revivals," Phys. Rep. **392**, 1 (2004).

[142] R. J. Glauber, "Quantum theory of optical coherence," Phys. Rev. **130**, 2529 (1963).

[143] L. Cao and M. L. Brongersma, "Ultrafast developments," Nat. Photon. **3**, 12 (2009).

[144] B. Lee, S. Kim, H. Kim, and Y. Lim, "The use of plasmonics in light beaming and focusing," Prog. Quantum Electron. **34**, 47 (2010).

[145] Y. M. Liu, T. Zentgraf, G. Bartal, and X. Zhang, "Transformational plasmon optics," Nano Lett. **10**, 1991 (2010).

[146] P. A. Huidobro, M. L. Nesterov, L. Martin-Moreno, and F. J. Garcia-Vidal, "Transformation optics for plasmonics," Nano Lett. **10**, 1985 (2010).

[147] L. Verslegers, P. B. Catrysse, Z. F. Yu, and S. H. Fan, "Deep-subwavelength focusing and steering of light in an aperiodic metallic waveguide array," Phys. Rev. Lett. **103**, 033902 (2009).

[148] M. A. Noginov, G. Zhu, M. Mayy, B. A. Ritzo, N. Noginova, and V. A. Podolskiy, "Stimulated emission of surface plasmon polaritons," Phys. Rev. Lett. **101**, 226806 (2008).

[149] M. I. Stockman, "Nanofocusing of optical energy in tapered plasmonic waveguides," Phys. Rev. Lett. **93**, 137404 (2004).

[150] A. R. Davoyan, I. V. Shadrivov, A. A. Zharov, D. K. Gramotnev, and Y. S. Kivshar, "Nonlinear nanofocusing in tapered plasmonic waveguides," Phys. Rev. Lett. **105**, 116804 (2010).

[151] A. Szameit, I. L. Garanovich, M. Heinrich, A. A. Sukhorukov, F. Dreisow, T. Pertsch, S. Nolte, A. Tuennermann, and Y. S. Kivshar, "Polychromatic dynamic localization in curved photonic lattices," Nat. Phys. **5**, 271 (2009).

[152] S. Vedantam, H. Lee, J. Tang, J. Conway, M. Staffaroni, and E. Yablonovitch, "A plasmonic dimple lens for nanoscale focusing of light," Nano Lett. **9**, 3447 (2009).

[153] M. Durach, A. Rusina, and M. I. Stockman, "Toward full spatiotemporal control on the nanoscale," Nano Lett. **7**, 3145 (2007).

[154] H. Gao, J. K. Hyun, M. H. Lee, J.-C. Yang, L. J. Lauhon, and T. W. Odom, "Broadband plasmonic microlenses based on patches of nanoholes," Nano Lett. **10**, 4111 (2010).

[155] S. I. Bozhevolnyi and J. Jung, "Scaling for gap plasmon based waveguides," Opt. Express **16**, 2676 (2008).

[156] S. I. Bozhevolnyi and K. V. Nerkararyan, "Channel plasmon polaritons guided by graded gaps: closed-form solutions," Opt. Express **17**, 10327 (2009).

[157] S. I. Bozhevolnyi, "Effective-index modeling of channel plasmon polaritons," Opt. Express **14**, 9467 (2006).

[158] D. Marcuse, *Light transmission optics* (Van Nostrand Reinhold, New York, 1972).

[159] S. I. Bozhevolnyi and K. V. Nerkararyan, "Adiabatic nanofocusing of channel plasmon polaritons," Opt. Lett. **35**, 541–543 (2010).

[160] S. Longhi, "Quantum-optical analogies using photonic structures," Laser Photonics Rev. **3**, 243 (2009).

[161] F. Dreisow, M. Heinrich, R. Keil, A. Tunnermann, S. Nolte, S. Longhi, and A. Szameit, "Classical simulation of relativistic zitterbewegung in photonic lattices," Phys. Rev. Lett. **105**, 143902 (2010).

[162] G. Della Valle, M. Savoini, M. Ornigotti, P. Laporta, V. Foglietti, M. Finazzi, L. Duo, and S. Longhi, "Experimental observation of a photon bouncing ball," Phys. Rev. Lett. **102**, 180402 (2009).

[163] C. G. Aminoff, A. M. Steane, P. Bouyer, P. Desbiolles, J. Dalibard, and C. Cohen-Tannoudji, "Cesium atoms bouncing in a stable gravitational cavity," Phys. Rev. Lett. **71**, 3083 (1993).

[164] V. V. Nesvizhevsky, H. G. Borner, A. K. Petukhov, H. Abele, S. Baeszler, F. J. Ruesz, T. Stoferle, A. Westphal, A. M. Gagarski, G. A. Petrov, and A. V. Strelkov, "Quantum states of neutrons in the earth's gravitational field," Nature **415**, 297 (2002).

[165] V. V. Nesvizhevsky, A. Y. Voronin, R. Cubitt, and K. V. Protasov, "Neutron whispering gallery," Nat. Phys. **6**, 114 (2010).

[166] J. P. Dowling and J. GeaBanacloche, "Evanescent light-wave atom mirrors, resonators waveguides, and traps," Adv. Atom. Mol. Opt. Phy. **37**, 1 (1996).

[167] P. Szriftgiser, D. GueryOdelin, M. Arndt, and J. Dalibard, "Atomic wave diffraction and interference using temporal slits," Phys. Rev. Lett. **77**, 4 (1996).

[168] A. Landragin, J. Y. Courtois, G. Labeyrie, N. Vansteenkiste, C. I. Westbrook, and A. Aspect, "Measurement of the van der waals force in an atomic mirror," Phys. Rev. Lett. **77**, 1464 (1996).

[169] S. T. Dembinski, A. J. Makowski, and P. Peplowski, "Quantum bouncer with chaos," Phys. Rev. Lett. **70**, 1093 (1993).

[170] T. Zentgraf, Y. Liu, M. H. Mikkelsen, J. Valentine, and X. Zhang, "Plasmonic luneburg and eaton lenses," Nat. Nanotech. **6**, 151 (2011).

[171] A. A. Maradudin, R. F. Wallis, and G. I. Stegeman, "The optics of surface and guided wave polaritons," Prog. Surf. Sci. **33**, 171 (1990).

[172] M. Andrews, "Wave packets bouncing off walls," Am. J. Phys. **66**, 252 (1998).

[173] J. A. Arnaud, *Beam and fiber optics* (Academic Press, New York, 1976).

[174] A. Royer, "Why are the energy levels of the quantum harmonic oscillator equally spaced?" Am. J. Phys. **64**, 1393 (1996).

[175] G. Della Valle and S. Longhi, "Graded index surface-plasmon-polariton devices for subwavelength light management," Phys. Rev. B **82**, 153411 (2010).

[176] H. Choo, M.-K. Kim, M. Staffaroni, T. J. Seok, J. Bokor, S. Cabrini, P. J. Schuck, M. C. Wu, and E. Yablonovitch, "Nanofocusing in a metal-insulator-metal gap plasmon waveguide with a three-dimensional linear taper," Nat. Photon. **6**, 838 (2012).

[177] E. Verhagen, M. Spasenović, A. Polman, and L. K. Kuipers, "Nanowire plasmon excitation by adiabatic mode transformation," Phys. Rev. Lett. **102**, 203904 (2009).

[178] V. S. Volkov, S. I. Bozhevolnyi, S. G. Rodrigo, L. Martin-Moreno, F. J. Garcia-Vidal, E. Devaux, and T. W. Ebbesen, "Nanofocusing with channel plasmon polaritons," Nano Lett. **9**, 1278 (2009).

[179] V. S. Volkov, J. Gosciniak, S. I. Bozhevolnyi, S. G. Rodrigo, L. Martin-Moreno, F. J. Garcia-Vidal, E. Devaux, and T. W. Ebbesen, "Plasmonic candle: towards efficient nanofocusing with channel plasmon polaritons," New. J. Phys. **11**, 113043 (2009).

[180] D. K. Gramotnev, "Adiabatic nanofocusing of plasmons by sharp metallic grooves: Geometrical optics approach," J. Appl. Phys. **98**, 104302 (2005).

[181] D. F. P. Pile and D. K. Gramotnev, "Adiabatic and nonadiabatic nanofocusing of plasmons by tapered gap plasmon waveguides," Appl. Phys. Lett. **89**, 041111 (2006).

[182] D. K. Gramotnev, D. F. P. Pile, M. W. Vogel, and X. Zhang, "Local electric field enhancement during nanofocusing of plasmons by a tapered gap," Phys. Rev. B **75**, 035431 (2007).

[183] R. X. Yang, M. A. G. Abushagur, and Z. L. Lu, "Efficiently squeezing near infrared light into a 21nm-by-24nm nanospot," Opt. Express **16**, 20142 (2008).

[184] M. V. Berry and N. L. Balazs, "Nonspreading wave packets." Am. J. Phys. **47**, 264 (1979).

[185] G. A. Siviloglou and D. N. Christodoulides, "Accelerating finite energy airy beams," Opt. Lett. **32**, 979 (2007).

[186] A. Salandrino and D. N. Christodoulides, "Airy plasmon: a nondiffracting surface wave," Opt. Lett. **35**, 2082 (2010).

[187] J. Baumgartl, M. Mazilu, and K. Dholakia, "Optically mediated particle clearing using airy wavepackets," Nat. Photon. **2**, 675 (2008).

[188] P. Polynkin, M. Kolesik, J. V. Moloney, G. A. Siviloglou, and D. N. Christodoulides, "Curved plasma channel generation using ultraintense airy beams," Science **324**, 229 (2009).

[189] A. Chong, W. H. Renninger, D. N. Christodoulides, and F. W. Wise, "Airy-bessel wave packets as versatile linear light bullets," Nat. Photon. **4**, 103 (2010).

[190] D. Abdollahpour, S. Suntsov, D. G. Papazoglou, and S. Tzortzakis, "Spatiotemporal airy light bullets in the linear and nonlinear regimes," Phys. Rev. Lett. **105**, 253901 (2010).

[191] T. Ellenbogen, N. Voloch-Bloch, A. Ganany-Padowicz, and A. Arie, "Nonlinear generation and manipulation of airy beams," Nat. Photon. **3**, 395 (2009).

[192] I. Dolev, T. Ellenbogen, and A. Arie, "Switching the acceleration direction of airy beams by a nonlinear optical process," Opt. Lett. **35**, 1581 (2010).

[193] S. Jia, J. Lee, J. W. Fleischer, G. A. Siviloglou, and D. N. Christodoulides, "Diffusion-trapped airy beams in photorefractive media," Phys. Rev. Lett. **104**, 253904 (2010).

[194] Y. Hu, P. Zhang, C. B. Lou, S. Huang, J. J. Xu, and Z. G. Chen, "Optimal control of the ballistic motion of airy beams," Opt. Lett. **35**, 2260 (2010).

[195] C. L. Lin, T. C. Hsiung, and M. J. Huang, "The general potential v(x, t) in which airy wave packets remain nonspreading," Eur. phys. Lett. **83**, 30002 (2008).

[196] F. Gori, M. Santarsiero, R. Borghi, and G. Guattari, "The general wavefunction for a particle under uniform force," Eur. J. Phys. **20**, 477 (1999).

[197] C. Bernardini, F. Gori, and M. Santarsiero, "Converting states of a particle under uniform or elastic forces into free particle states," Eur. phys. Lett. **16**, 58 (2008).

[198] J. Broky, G. A. Siviloglou, A. Dogariu, and D. N. Christodoulides, "Self-healing properties of optical airy beams," Opt. Express **16**, 12880 (2008).

[199] C. F. Bohren and D. R. Huffman, *Absorption and scattering of light by small particles* (Wiley, New York, 1983).

[200] G. Schmid, *Nanoparticles : from theory to application* (Wiley-VCH, Weinheim, 2010), 2nd ed.

[201] Z. C. Ruan and S. H. Fan, "Design of subwavelength superscattering nanospheres," Appl. Phys. Lett. **98**, 043101 (2011).

[202] L. Verslegers, Z. Yu, Z. Ruan, P. B. Catrysse, and S. Fan, "From electromagnetically induced transparency to superscattering with a single structure: A coupled-mode theory for doubly resonant structures," Phys. Rev. Lett. **108**, 083902 (2012).

[203] A. E. Miroshnichenko, B. Luk'yanchuk, S. A. Maier, and Y. S. Kivshar, "Optically induced interaction of magnetic moments in hybrid metamaterials," ACS Nano **6**, 837 (2012).

[204] N. M. Lawandy, "Localized surface plasmon singularities in amplifying media," Appl. Phys. Lett. **85**, 5040 (2004).

[205] S. Linden, C. Enkrich, M. Wegener, J. F. Zhou, T. Koschny, and C. M. Soukoulis, "Magnetic response of metamaterials at 100 terahertz," Science **306**, 1351 (2004).

[206] A. I. Kuznetsov, A. E. Miroshnichenko, Y. H. Fu, J. B. Zhang, and B. S. Lukyanchuk, "Magnetic light," Sci. Rep. **2**, 492 (2012).

[207] N. S. King, Y. Li, C. Ayala-Orozco, T. Brannan, P. Nordlander, and N. J. Halas, "Angle- and spectral-dependent light scattering from plasmonic nanocups," ACS Nano **5**, 7254 (2011).

[208] T. Kosako, Y. Kadoya, and H. F. Hofmann, "Directional control of light by a nano-optical yagi-uda antenna," Nat. Photon. **4**, 312 (2010).

[209] T. Pakizeh and M. Kall, "Unidirectional ultracompact optical nanoantennas," Nano Lett. **9**, 2343 (2009).

[210] T. H. Taminiau, F. D. Stefani, F. B. Segerink, and N. F. Van Hulst, "Optical antennas direct single-molecule emission," Nat. Photon. **2**, 234 (2008).

[211] A. B. Evlyukhin, S. I. Bozhevolnyi, A. Pors, M. G. Nielsen, I. P. Radko, M. Willatzen, and O. Albrektsen, "Detuned electrical dipoles for plasmonic sensing," Nano Lett. **10**, 481 (2010).

[212] T. Shegai, S. Chen, V. D. Miljkovic, G. Zengin, P. Johansson, and M. Kall, "A bimetallic nanoantenna for directional colour routing," Nat. Commun. **2**, 4571 (2011).

[213] P. Spinelli, M. A. Verschuuren, and A. Polman, "Broadband omnidirectional antireflection coating based on subwavelength surface mie resonators," Nat. Commun. **3**, 692 (2012).

[214] T. Shegai, V. D. Miljkovic, K. Bao, H. X. Xu, P. Nordlander, P. Johansson, and M. Kall, "Unidirectional broadband light emission from supported plasmonic nanowires," Nano Lett. **11**, 706 (2011).

[215] V. D. Miljkovic, T. Shegai, M. Kall, and P. Johansson, "Mode-specific directional emission from hybridized particle-on-a-film plasmons," Opt. Express **19**, 12856 (2011).

[216] Z. P. Li, F. Hao, Y. Z. Huang, Y. R. Fang, P. Nordlander, and H. X. Xu, "Directional light emission from propagating surface plasmons of silver nanowires," Nano Lett. **9**, 4383 (2009).

[217] H. Aouani, O. Mahboub, N. Bonod, E. Devaux, E. Popov, H. Rigneault, T. W. Ebbesen, and J. Wenger, "Bright unidirectional fluorescence emission of molecules in a nanoaperture with plasmonic corrugations," Nano Lett. **11**, 637 (2011).

[218] G. H. Rui, R. L. Nelson, and Q. W. Zhan, "Circularly polarized unidirectional emission via a coupled plasmonic spiral antenna," Opt. Lett. **36**, 4533 (2011).

[219] M. Kerker, D. S. Wang, and C. L. Giles, "Electromagnetic scattering by magnetic spheres," J. Opt. Soc. Am. **73**, 765 (1983).

[220] A. W. Love, "Some highlights in reflector antenna development," Radio. Sci. **11**, 671 (1976).

[221] A. E. Krasnok, A. E. Miroshnichenko, P. A. Belov, and Y. S. Kivshar, "Huygens optical elements and yagi-uda nanoantennas based on dielectric nanoparticles," JETP. Lett. **94**, 593 (2011).

[222] J. B. Pendry, A. J. Holden, D. J. Robbins, and W. J. Stewart, "Magnetism from conductors and enhanced nonlinear phenomena," IEEE. T. Microw. Theory **47**, 2075 (1999).

[223] L. Peng, L. Ran, H. Chen, H. Zhang, J. A. Kong, and T. M. Grzegorczyk, "Experimental observation of left-handed behavior in an array of standard dielectric resonators," Phys. Rev. Lett. **98**, 157403 (2007).

[224] K. Vynck, D. Felbacq, E. Centeno, A. I. Cabuz, D. Cassagne, and B. Guizal, "All-dielectric rod-type metamaterials at optical frequencies," Phys. Rev. Lett. **102**, 133901 (2009).

[225] A. B. Evlyukhin, C. Reinhardt, A. Seidel, B. S. Luk'yanchuk, and B. N. Chichkov, "Optical response features of si-nanoparticle arrays," Phys. Rev. B **82**, 045404 (2010).

[226] A. Garcia-Etxarri, R. Gomez-Medina, L. S. Froufe-Perez, C. Lopez, L. Chantada, F. Scheffold, J. Aizpurua, M. Nieto-Vesperinas, and J. J. Saenz, "Strong magnetic response of submicron silicon particles in the infrared," Opt. Express **19**, 4815 (2011).

[227] R. Gomez-Medina, B. Garcia-Camara, I. Suarez-Lacalle, F. Gonzalez, F. Moreno, M. Nieto-Vesperinas, and J. J. Saenz, "Electric and magnetic dipolar response of germanium nanospheres: interference effects, scattering anisotropy, and optical forces," J. Nanophotonics **5**, 053512 (2011).

[228] A. B. Evlyukhin, S. M. Novikov, U. Zywietz, R. L. Eriksen, C. Reinhardt, S. I. Bozhevolnyi, and B. N. Chichkov, "Demonstration of magnetic dipole resonances of dielectric nanospheres in the visible region," Nano Lett. **12**, 3749 (2012).

[229] R. Paniagua-Dominguez, F. Lopez-Tejeira, R. Marques, and J. A. Sanchez-Gil, "Metallo-dielectric core-shell nanospheres as building blocks for optical three-dimensional isotropic negative-index metamaterials," New. J. Phys. **13**, 123017 (2011).

[230] J. A. Schuller, R. Zia, T. Taubner, and M. L. Brongersma, "Dielectric metamaterials based on electric and magnetic resonances of silicon carbide particles," Phys. Rev. Lett. **99**, 107401 (2007).

[231] P. Y. Fan, U. K. Chettiar, L. Y. Cao, F. Afshinmanesh, N. Engheta, and M. L. Brongersma, "An invisible metal-semiconductor photodetector," Nat. Photon. **6**, 380 (2012).

[232] R. Paniagua-Dominguez, D. R. Abujetas, and J. A. Sanchez-Gil, "Ultra low-loss, isotropic optical negative-index metamaterial based on hybrid metal-semiconductor nanowires," Sci. Rep. **3**, 1057 (2013).

[233] M. S. Wheeler, J. S. Aitchison, and M. Mojahedi, "Coated nonmagnetic spheres with a negative index of refraction at infrared frequencies," Phys. Rev. B **73**, 045105 (2006).

[234] O. Pena and U. Pal, "Scattering of electromagnetic radiation by a multilayered sphere," Comput. Phys. Commun. **180**, 2348 (2009).

[235] P. B. Johnson and R. W. Christy, "Optical constants of the noble metals," Phys. Rev. B **6**, 4370 (1972).

[236] D. W. Brandl, N. A. Mirin, and P. Nordlander, "Plasmon modes of nanosphere trimers and quadrumers," J. Phys. Chem. B **110**, 12302 (2006).

[237] G. W. Mulholland, C. F. Bohren, and K. A. Fuller, "Light-scattering by agglomerates - coupled electric and magnetic dipole method," Langmuir **10**, 2533 (1994).

[238] O. Merchiers, F. Moreno, F. Gonzalez, and J. M. Saiz, "Light scattering by an ensemble of interacting dipolar particles with both electric and magnetic polarizabilities," Phys. Rev. A **76**, 043834 (2007).

[239] A. L. Burin, H. Cao, G. C. Schatz, and M. A. Ratner, "High-quality optical modes in low-dimensional arrays of nanoparticles: application to random lasers," J. Opt. Soc. Am. B **21**, 121 (2004).

[240] R. Ramaswami, "Optical fiber communication: from transmission to networking," IEEE. Commun. Mag. **40**, 138 (2002).

[241] X. G. Meng, K. Fujita, S. Murai, T. Matoba, and K. Tanaka, "Plasmonically controlled lasing resonance with metallic-dielectric core-shell nanoparticles," Nano Lett. **11**, 1374 (2011).

[242] R. T. Tom, A. S. Nair, N. Singh, M. Aslam, C. L. Nagendra, R. Philip, K. Vijayamohanan, and T. Pradeep, "Freely dispersible au@tio2, au@zro2, ag@tio2, and ag@zro2 core@shell nanoparticles: One-step synthesis, characterization, spectroscopy, and optical limiting properties," Langmuir **19**, 3439 (2003).

[243] Y. Yao, J. Yao, V. K. Narasimhan, Z. Ruan, C. Xie, S. Fan, and Y. Cui, "Broadband light management using low-q whispering gallery modes in spherical nanoshells," Nat. Commun. **3**, 664 (2012).

[244] B. S. Luk'yanchuk and C. W. Qiu, "Enhanced scattering efficiencies in spherical particles with weakly dissipating anisotropic materials," Appl. Phys. A **92**, 773 (2008).

[245] C. W. Qiu and B. Luk'yanchuk, "Peculiarities in light scattering by spherical particles with radial anisotropy," J. Opt. Soc. Am. A **25**, 1623 (2008).

[246] C. Qiu, L. Gao, J. D. Joannopoulos, and M. Soljacic, "Light scattering from anisotropic particles: propagation, localization, and nonlinearity," Laser Photonics Rev. **4**, 268 (2010).

[247] M. Kerker, *The scattering of light, and other electromagnetic radiation* (Academic Press, New York, 1969).

[248] A. E. Miroshnichenko, S. Flach, and Y. S. Kivshar, "Fano resonances in nanoscale structures," Rev. Mod. Phys. **82**, 2257 (2010).

[249] B. Luk'yanchuk, N. I. Zheludev, S. A. Maier, N. J. Halas, P. Nordlander, H. Giessen, and C. T. Chong, "The fano resonance in plasmonic nanostructures and metamaterials," Nat. Mater. **9**, 707 (2010).

[250] B. S. Luk'yanchuk, A. E. Miroshnichenko, and Y. S. Kivshar, "Fano resonances and topological optics: an interplay of far- and near-field interference phenomena," J. Opt. **15**, 073001 (2013).

[251] U. Fano, "Effects of configuration interaction on intensities and phase shifts," Phys. Rev. **124**, 1866 (1961).

[252] F. Hao, Y. Sonnefraud, P. V. Dorpe, S. A. Maier, N. J. Halas, and P. Nordlander, "Symmetry breaking in plasmonic nanocavities: Subradiant lspr sensing and a tunable fano resonance," Nano Lett. **8**, 3983 (2008).

[253] S. L. Zou, N. Janel, and G. C. Schatz, "Silver nanoparticle array structures that produce remarkably narrow plasmon lineshapes," J. Chem. Phys. **120**, 10871 (2004).

[254] V. A. Markel, "Divergence of dipole sums and the nature of non-lorentzian exponentially narrow resonances in one-dimensional periodic arrays of nanospheres," J. Phys. B. Mol. Opt. **38**, L115 (2005).

[255] B. Auguie and W. L. Barnes, "Collective resonances in gold nanoparticle arrays," Phys. Rev. Lett. **101**, 143902 (2008).

[256] V. G. Kravets, F. Schedin, and A. N. Grigorenko, "Extremely narrow plasmon resonances based on diffraction coupling of localized plasmons in arrays of metallic nanoparticles," Phys. Rev. Lett. **101**, 087403 (2008).

[257] M. Hentschel, M. Saliba, R. Vogelgesang, H. Giessen, A. P. Alivisatos, and N. Liu, "Transition from isolated to collective modes in plasmonic oligomers," Nano Lett. **10**, 2721 (2010).

[258] V. A. Fedotov, M. Rose, S. L. Prosvirnin, N. Papasimakis, and N. I. Zheludev, "Sharp trapped-mode resonances in planar metamaterials with a broken structural symmetry," Phys. Rev. Lett. **99**, 147401 (2007).

[259] W. Zhang, A. O. Govorov, and G. W. Bryant, "Semiconductor-metal nanoparticle molecules: Hybrid excitons and the nonlinear fano effect," Phys. Rev. Lett. **97**, 146804 (2006).

[260] S. Zhang, D. A. Genov, Y. Wang, M. Liu, and X. Zhang, "Plasmon-induced transparency in metamaterials," Phys. Rev. Lett. **101**, 047401 (2008).

[261] A. E. Miroshnichenko, S. F. Mingaleev, S. Flach, and Y. S. Kivshar, "Nonlinear fano resonance and bistable wave transmission," Phys. Rev. E **71**, 036626 (2005).

[262] R. W. Wood, "On a remarkable case of uneven distribution of light in a diffraction grating spectrum," Proc. Phys. Soc. Lond. **18**, 269 (1902).

[263] L. Rayleigh, "On the dynamical theory of gratings," Proc. R. Soc. Lond. **79**, 399 (1907).

[264] U. Fano, "The theory of anomalous diffraction gratings and of quasi-stationary waves on metallic surfaces (sommerfeld's waves)," J. Opt. Soc. Am. **31**, 213 (1941).

[265] A. Hessel and A. A. Oliner, "A new theory of wood's anomalies on optical gratings," Appl. Opt. **4**, 1275 (1965).

[266] H. Liu, D. A. Genov, D. M. Wu, Y. M. Liu, J. M. Steele, C. Sun, S. N. Zhu, and X. Zhang, "Magnetic plasmon propagation along a chain of connected subwavelength resonators at infrared frequencies," Phys. Rev. Lett. **97**, 243902 (2006).

[267] C. J. Tang, P. Zhan, Z. S. Cao, J. Pan, Z. Chen, and Z. L. Wang, "Magnetic field enhancement at optical frequencies through diffraction coupling of magnetic plasmon resonances in metamaterials," Phys. Rev. B **83**, 041402 (2011).

[268] K. Aydin, V. E. Ferry, R. M. Briggs, and H. A. Atwater, "Broadband polarization-independent resonant light absorption using ultrathin plasmonic super absorbers," Nat. Commun. **2**, 517 (2011).

[269] M. V. Berry, "The adiabatic phase and pancharatnam phase for polarized-light," J. Mod. Opt. **34**, 1401 (1987).

[270] M. Onoda, S. Murakami, and N. Nagaosa, "Hall effect of light," Phys. Rev. Lett. **93**, 083901 (2004).

[271] K. Y. Bliokh, A. Niv, V. Kleiner, and E. Hasman, "Geometrodynamics of spinning light," Nat. Photon. **2**, 748 (2008).

[272] X. B. Yin, Z. L. Ye, J. Rho, Y. Wang, and X. Zhang, "Photonic spin hall effect at metasurfaces," Science **339**, 1405 (2013).

[273] N. Shitrit, I. Bretner, Y. Gorodetski, V. Kleiner, and E. Hasman, "Optical spin hall effects in plasmonic chains," Nano Lett. **11**, 2038 (2011).

[274] Y. Gorodetski, S. Nechayev, V. Kleiner, and E. Hasman, "Plasmonic aharonov-bohm effect: Optical spin as the magnetic flux parameter," Phys. Rev. B **82**, 125433 (2010).

[275] K. Y. Bliokh, Y. Gorodetski, V. Kleiner, and E. Hasman, "Coriolis effect in optics: Unified geometric phase and spin-hall effect," Phys. Rev. Lett. **101**, 030404 (2008).

[276] C. Leyder, M. Romanelli, J. P. Karr, E. Giacobino, T. C. H. Liew, M. M. Glazov, A. V. Kavokin, G. Malpuech, and A. Bramati, "Observation of the optical spin hall effect," Nat. Phys. **3**, 628 (2007).

[277] O. Hosten and P. Kwiat, "Observation of the spin hall effect of light via weak measurements," Science **319**, 787 (2008).

[278] A. E. Miroshnichenko and Y. S. Kivshar, "Polarization traffic control for surface plasmons," Science **340**, 283 (2013).

[279] F. J. Rodriguez-Fortuno, G. Marino, P. Ginzburg, D. O'Connor, A. Martinez, G. A. Wurtz, and A. V. Zayats, "Near-field interference for the unidirectional excitation of electromagnetic guided modes," Science **340**, 328 (2013).

[280] J. Lin, J. P. B. Mueller, Q. Wang, G. H. Yuan, N. Antoniou, X. C. Yuan, and F. Capasso, "Polarization-controlled tunable directional coupling of surface plasmon polaritons," Science **340**, 331 (2013).

[281] N. Shitrit, I. Yulevich, E. Maguid, D. Ozeri, D. Veksler, V. Kleiner, and E. Hasman, "Spin-optical metamaterial route to spin-controlled photonics," Science **340**, 724 (2013).

[282] D. Xiao, M. C. Chang, and Q. Niu, "Berry phase effects on electronic properties," Rev. Mod. Phys. **82**, 1959 (2010).

[283] Y. Gorodetski, N. Shitrit, I. Bretner, V. Kleiner, and E. Hasman, "Observation of optical spin symmetry breaking in nanoapertures," Nano Lett. **9**, 3016 (2009).

[284] A. K. Geim and K. S. Novoselov, "The rise of graphene," Nat. Mater. **6**, 183 (2007).

[285] A. N. Grigorenko, M. Polini, and K. S. Novoselov, "Graphene plasmonics," Nat. Photon. **6**, 749 (2012).

[286] H. Buljan, M. Jablan, and M. Soljacic, "Graphene plasmonics damping of plasmons in graphene," Nat. Photon. **7**, 346 (2013).

[287] S. A. Maier, "Graphene plasmonics all eyes on flatland," Nat. Phys. **8**, 581 (2012).

[288] P. Tassin, T. Koschny, M. Kafesaki, and C. M. Soukoulis, "A comparison of graphene, superconductors and metals as conductors for metamaterials and plasmonics," Nat. Photon. **6**, 259 (2012).

[289] X. L. Qi and S. C. Zhang, "The quantum spin hall effect and topological insulators," Phys. Today **63**, 33 (2010).

[290] X.-L. Qi and S.-C. Zhang, "Topological insulators and superconductors," Rev. Mod. Phys. **83**, 1057 (2011).

[291] M. Z. Hasan and C. L. Kane, "Colloquium: Topological insulators," Rev. Mod. Phys. **82**, 3045 (2010).

[292] A. B. Khanikaev, S. H. Mousavi, W. K. Tse, M. Kargarian, A. H. MacDonald, and G. Shvets, "Photonic topological insulators," Nat. Mater. **12**, 233 (2013).

[293] M. C. Rechtsman, J. M. Zeuner, Y. Plotnik, Y. Lumer, D. Podolsky, F. Dreisow, S. Nolte, M. Segev, and A. Szameit, "Photonic floquet topological insulators," Nature **496**, 196 (2013).

[294] A. Karch, "Surface plasmons and topological insulators," Phys. Rev. B **83**, 245432 (2011).

[295] M. Mecklenburg and B. C. Regan, "Spin and the honeycomb lattice: Lessons from graphene," Phys. Rev. Lett. **106**, 116803 (2011).

[296] D. Leykam, O. Bahat-Treidel, and A. S. Desyatnikov, "Pseudospin and nonlinear conical diffraction in lieb lattices," Phys. Rev. A **86**, 031805 (2012).

[297] K. J. Fang, Z. F. Yu, and S. H. Fan, "Realizing effective magnetic field for photons by controlling the phase of dynamic modulation," Nat. Photon. **6**, 782 (2012).

[298] F. D. M. Haldane and S. Raghu, "Possible realization of directional optical waveguides in photonic crystals with broken time-reversal symmetry," Phys. Rev. Lett. **100**, 013904 (2008).

[299] Z. Wang, Y. D. Chong, J. D. Joannopoulos, and M. Soljacic, "Observation of unidirectional backscattering-immune topological electromagnetic states," Nature **461**, 772 (2009).